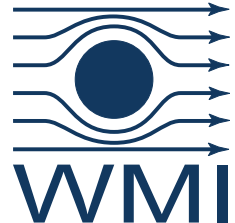


BAYERISCHE  
AKADEMIE  
DER  
WISSENSCHAFTEN



**Propagating quantum microwave  
photonics:  
Transmon qubit in a broadband on-chip  
environment**

Dissertation

Peter Eder

October 2021

Advisor: Prof. Dr. Rudolf Gross

Fakultät für Physik  
TECHNISCHE UNIVERSITÄT MÜNCHEN



TECHNISCHE UNIVERSITÄT MÜNCHEN

Fakultät für Physik

**Propagating quantum microwave  
photonics:  
Transmon qubit in a broadband on-chip  
environment**

Peter Eder

Vollständiger Abdruck der von der Fakultät für Physik der Technischen  
Universität München zur Erlangung des akademischen Grades eines

**Doktors der Naturwissenschaften**

genehmigten Dissertation.

Vorsitzender: Prof. Dr. Martin Zacharias

Prüfer der Dissertation: 1. Prof. Dr. Rudolf Gross  
2. Prof. Dr. Alexander Holleitner

Die Dissertation wurde am 13.10.2021 bei der  
Technischen Universität München eingereicht und durch  
die Fakultät für Physik am 29.11.2021 angenommen.



*To my family*



# Abstract

Superconducting circuits have become a key technology platform in the field of quantum science and technology, and the quantum properties of the microwave signals emitted from these circuits have become a popular object of study. The related experiments can be divided in experiments where the focus is put on the implementation of continuous-variable quantum protocols and the ones which aim at realizing scattering experiments of microwave photons. This latter set of experiments, to which also this work contributes, is closely related to the concepts of generation, routing, manipulation, and detection of propagating quantum states. These areas have been actively explored in photonics at optical frequencies and are - in analogy to optics - therefore often referred to as microwave quantum photonics. In this work, we study the scattering of an incident microwave field off an artificial atom placed in a broadband, but nevertheless carefully engineered, open environment provided by a superconducting quantum circuit. To this end, we design and fabricate the according microwave circuits, and optimize their design, packaging and shielding. We conduct spectral measurements for a broad range of frequencies. We use a transfer matrix model to fit the obtained spectral data, and extract the decoherence parameters of the physical system. Based on model assumptions, we extract the noise characteristics of our sample. Finally, we confirm that the high frequency noise in our system can be described by the spin boson model and the low frequency noise is well described in the  $1/f$ -noise limit of the Ornstein-Uhlenbeck approach.



# Kurzzusammenfassung

In den letzten Jahren haben sich supraleitende Schaltkreise zu einer Schlüsseltechnologie im Bereich der Quantentechnologien entwickelt, wobei die Eigenschaften von Mikrowellensignalen, die von solchen Schaltkreisen emittiert werden, ein beliebtes Studienobjekt darstellen. In Hinblick auf die dazu durchgeführten Experimente lassen sich zwei Klassen unterscheiden. Es gibt einerseits Experimente, die ihr Hauptaugenmerk auf Protokolle mit kontinuierlichen Variablen legen, und andererseits solche, die die Streuung von Mikrowellenphotonen untersuchen. Diese Arbeit fällt die zweite Kategorie von Experimenten und ist somit artverwandt zu Untersuchungen zur Generation, Manipulation und Detektion von Photonen, welche bei optischen Frequenzen bereits intensiv untersucht wurden und dem Gebiet der optischen Photonik zuzuordnen sind. In dieser Arbeit untersuchen wir die Streuung eines eingehenden Mikrowellenfeldes an einem in einer breitbandigen, ingenieurmäßig maßgeschneiderten, Umgebung platzierten, künstlichen Atom. Zu diesem Zweck entwerfen, fabrizieren und optimieren wir die Mikrowellenschaltkreise, welche Umgebung und künstliches Atom realisieren. Wir verbessern zusätzlich das Gehäuse und die Abschirmung, sowie die Verbindungstechnik der verwendeten Chips. Wir führen spektral aufgelöste Messungen über einen breiten Frequenzbereich durch und nutzen das Transfermatrizenmodell, um die erhaltenen Messdaten zu fitten. Basierend auf wenigen Annahmen schließen wir auf die Rauscheigenschaften unserer Probe. Wir bestätigen dadurch, dass sich das hochfrequente Rauschen in unserem System mit dem Spin-Boson Modell erklären lässt, während sich der niederfrequente Rauschanteil gut mit einem Ornstein-Uhlenbeck Ansatz im  $1/f$ -Limit darstellen lässt.



# Contents

<b>1</b>	<b>Introduction</b>	<b>1</b>
<b>2</b>	<b>Quantum microwave photonics</b>	<b>5</b>
2.1	Transfer matrix formalism . . . . .	5
2.2	Lumped element circuit theory . . . . .	14
2.3	Classical lossless circuits . . . . .	21
2.3.1	Coplanar waveguide transmission line . . . . .	21
2.3.2	Transmission line resonator . . . . .	24
2.3.3	Quadrature hybrid beam splitter . . . . .	26
2.3.4	Mach-Zehnder interferometer . . . . .	32
2.4	Superconducting quantum circuits . . . . .	35
2.4.1	LC-resonator . . . . .	35
2.4.2	Transmission line . . . . .	37
2.4.3	Qubit . . . . .	38
2.4.4	Qubit in a microwave interferometer . . . . .	55
2.5	Open quantum systems . . . . .	57
2.5.1	Spin-boson model . . . . .	58
2.5.2	Noise and decoherence . . . . .	59
2.5.3	Ornstein-Uhlenbeck model . . . . .	62
<b>3</b>	<b>Experimental techniques</b>	<b>65</b>
3.1	Cryogenics . . . . .	65
3.2	Fabrication . . . . .	66
3.2.1	Niobium structures . . . . .	67
3.2.2	Aluminum structures . . . . .	67
3.2.3	Designs . . . . .	68
3.3	Measurement setup . . . . .	74
3.3.1	Packaging . . . . .	76
3.3.2	Magnetic shielding . . . . .	77
3.4	Measurement techniques . . . . .	79
<b>4</b>	<b>Quantum probe of a broadband on-chip interferometer</b>	<b>83</b>
4.1	Fundamental building blocks . . . . .	83
4.2	Transmon qubit in interferometer . . . . .	93

---

<b>5 Summary and outlook</b>	<b>103</b>
<b>Bibliography</b>	<b>107</b>
<b>List of publications</b>	<b>115</b>
<b>A Details on cryogenic setups</b>	<b>121</b>
A.1 Helium bath cryostat . . . . .	121
A.2 Wet dilution refrigerator . . . . .	122
A.3 Dry dilution refrigerator . . . . .	124
<b>B Derivation of Hamiltonians</b>	<b>125</b>
B.1 LC resonator . . . . .	125
B.2 Cooper pair box . . . . .	131
<b>C Cooper pair box and transmon as qubit</b>	<b>137</b>
C.1 Harmonic oscillator . . . . .	137
C.2 Introduce nonlinear inductance . . . . .	137
C.3 Restriction to two energy levels . . . . .	139
<b>D Coplanar waveguide transmission line</b>	<b>141</b>

# List of Figures

2.1	Transmission and reflection $S$ -parameter for a device with $N$ ports. We are interested in the voltages $V_i$ and currents $I_i$ evaluated at reference planes $T_i$ . Figure with kind permission of Christian Schneider [25].	6
2.2	(a) The voltage phasor of the wave reflected at a terminated transmission line, which is a very simple one-port network, defines the reflection coefficient $\Gamma = V_1^-(z, t)/V_1^+(z, t)$ . (b) The four transmission and reflection coefficients at a two-port device define a $2 \times 2$ matrix.	7
2.3	(a) A transfer matrix relates the waves at the input port (red) of a device to waves at the output port(s) (blue). (b) In contrast, a scattering matrix connects all incident waves (red) to all rejected waves (blue), regardless of the port.	9
2.4	A sequence of transfer matrices can be used to model several scatterers in series. The modes at the output port (port 4) of a chain of two devices can be obtained by applying $\mathcal{T}_1$ on the modes at the input port of the first device (port 1), which gives the modes at the output of the first device (port 2), which are used as input for the second device (port 3). Finally $\mathcal{T}_2$ is applied to obtain modes at the output port (port 4).	11
2.5	Scattering matrices <b>cannot</b> be used sequentially to model the effect of several scatterers. The scattering matrix $\mathcal{S}_3$ connecting the incident and reflected modes of a chain of device A and B cannot be decomposed into a product of the individual $S$ -matrices $\mathcal{S}_1$ and $\mathcal{S}_2$ .	12
2.6	In a transmission measurement we apply a well defined signal $V_1^+(z, t)$ at one defined input port and no signal at the other. Reflection and transmission are measured.	13
2.7	(a) An electric circuit is represented by a network of elements. We restrict our considerations to elements with two terminals. The connection between the elements is drawn as line and constitutes a branch. Branches meet at nodes (red dots). Nodes that can be reached via different paths form loops. (b) Single circuit element, for which the voltage drop $V$ and the current intensity $I$ are investigated. The reference directions for current and voltage are reflected by the orientation of the associated arrows. Although both can be chosen at will, it is standard to have opposite reference orientation for voltage and current.	15

2.8	(a) A circuit diagram is used to do a nodal analysis, which is a systematic way to find a set of equations relating the descriptive variables of a circuit. (b) KCL is used to relate currents flowing in or out of nodes. Node a: $I_1 + I_2 + I_3 = 0$ . (c) KVL is used to relate the voltage drops across circuit elements within loops. Loop C: $V_1 - V_2 = 0$ . . . .	17
2.9	Circuit diagram symbol for a capacitor with $I$ and $V$ depicted. . . .	17
2.10	Circuit diagram symbol for an inductor with $I$ and $V$ depicted. . . .	18
2.11	(a) Equivalent circuit for a LC-resonator consisting of an inductance $L_r$ and a capacitance $C_r$ with a resonance frequency $\omega_0 = \frac{1}{\sqrt{L_r C_r}}$ . In shaded grey we see how this circuit can be integrated to another via coupling capacitors. Resistive elements, introducing damping to the system, are not modeled. (b) Typical Lorentzian shaped transmission magnitude spectrum for a damped resonator. . . . .	19
2.12	We model the effect of our circuit on a probe signal as a scattering potential acting on an incoming wave. Thus a parameterized transfer matrix $\mathcal{T}(\vec{p})$ gives the relation between the final waveform $V_f(z, t)$ and the initial waveform $V_i(z, t)$ . Thus $V_f(z, t) = \mathcal{T}(\vec{p}) \cdot V_i(z, t)$ . Here the internal structure of the potential is modeled in the parameter vector $\vec{p}$	21
2.13	Phase of an EM wave propagating down a transmission line: At Position $x_1$ we measure a phase-difference $\Delta\varphi_{01} = \varphi_1 - \varphi_0$ , compared to the phase $\varphi_0$ at position $x_0$ . Thus, $T_{11} = e^{-i\Delta\varphi_{01}}$ is the transfer matrix element for a TL of length $l_1$ . . . . .	22
2.14	(a) Design of a half-wavelength transmission line resonator. $g$ and $w$ define the characteristic impedance of the TL and together with $l$ the characteristic frequency of the resonator. $d_{1,2}$ then define the coupling capacitors $C_{k,1}$ and $C_{k,2}$ . (b) Equivalent circuit for the design shown in (a). . . . .	24
2.15	Circuit diagram of a quadrature hybrid beam splitter. . . . .	26
2.16	The H-section is the main building block for a microwave beam splitter. It consists of two T-junctions in nodes $a$ and $b$ . . . . .	27
2.17	Two H-sections (blue, red) connected by two transmission lines (dark green) form a beam splitter. A theoretical description is obtained by multiplication of the according transfer matrices $\mathcal{T}_{H,1}$ , $\mathcal{T}_{TL}$ , and $\mathcal{T}_{H,2}$ . . . . .	27
2.18	Calculated isolation, straight, and cross transmission / reflection spectrum of an ideal beam splitter (see inset) with $\omega_{BS}/(2\pi) = 5.75$ GHz [Method equivalent to Ref. [25], using Eq. (2.51)]. (a) Magnitude (b) Phase . . . . .	31
2.19	The structure presented in (a) is a microwave equivalent of a Mach-Zehnder interferometer in optics shown in (b). The scatterer (depicted as symbolic atom in a box), whose phase shift is measured, in our composite system will be replaced by a transmon qubit. . . . .	32
2.20	Circuit diagram of microwave interferometer (Mach-Zehnder type) with indication of transmission of an incident signal of frequency $\omega_{IF}$ at port 1. Blue shaded areas mark parts of the circuit modeled by according transfer matrices. . . . .	33

2.21	Calculated isolation, straight, and cross transmission / reflection spectrum of an ideal microwave interferometer with $\omega_{\text{IF}} = 5.75$ GHz [Method equivalent to Ref. [25], using Eq. (2.54)]. (a) Magnitude (b) Phase . . . . .	34
2.22	An LC resonator is analogous to a particle in a harmonic potential. Both are quantum harmonic oscillators with equidistant energy levels $\Delta E = \hbar\omega_0$ . . . . .	37
2.23	The Bloch sphere is a graphical representation of the quantum state of a qubit. The vector $\mathbf{r} = (r \sin \theta \cos \xi, r \sin \theta \sin \xi, r \cos \theta)$ represents the qubit state $ \psi\rangle = \cos \frac{\theta}{2} g\rangle + e^{i\xi} \sin \frac{\theta}{2} e\rangle$ . For free evolution in time, the state vector $r$ precesses around the z-axis. . . . .	38
2.24	The phase $\chi$ of the applied microwave pulse determines the axis of the rotation of the qubit state. . . . .	40
2.25	(a) A Josephson junction is a sandwich structure of two superconductors separated by a thin insulator-layer. Macroscopic wavefunctions model the superconducting areas of the junction. (b) Circuit diagram representation as inductor and capacitor (top) or as cross inside a square (bottom). . . . .	42
2.26	(a) An ideal dc SQUID consists of a superconducting ring interrupted by identical two JJs ( $E_{J,1} = E_{J,2}$ ). (b) The coupling energy of a dc SQUID is modulated by the external frustration $f_{\text{ext}} = \Phi_{\text{ext}}/\Phi_0$ with asymmetry parameters $d = 0$ and $d = 0.15$ . . . . .	44
2.27	(a) Equivalent circuit of a transmon qubit. The branches marked in red are additional in comparison to a dc SQUID. (b) Potential and energy levels of a transmon. The blue line shows the transmon potential, the dashed red line a harmonic potential. . . . .	46
2.28	Transmon qubit coupled to a single resonator. Both entities are modeled with their equivalent circuits. . . . .	47
2.29	The energy levels of the JC Hamiltonian. (a) In the resonant regime, energy levels of degenerate doublets split due to the coupling $g$ . (b) In the dispersive regime, where qubit and resonator are strongly detuned, the coupling gives rise to dressed states with ac-Stark- and Lamb-shifted energy levels. . . . .	48
2.30	The transmission spectrum of the qubit-resonator system. Coupled system (black), noninteracting resonator (red), noninteracting qubit (blue). . . . .	49
2.31	In the equivalent circuit of a transmission line, one of infinitely many LC-resonators is replaced by a transmon qubit. . . . .	50
2.32	A transmission line of characteristic impedance $Z_0$ (white), with a small piece having a different characteristic impedance $Z_{\text{eff}}$ (dark blue), caused by an LC resonator circuit and a coupling capacitor (light blue). . . . .	51
2.33	The transmission and reflection spectrum of an qubit in a transmission line in the low power limit. (a) Transmission magnitude (b) Phase. . . . .	54

2.34	(a) A transmon qubit placed in one arm of a microwave interferometer. (b) Transfer matrix to model circuit in (a). . . . .	55
2.35	Circuit diagram of a transmon qubit placed in one arm of a microwave interferometer. The transfer matrices of the individual components are marked in blue. . . . .	56
2.36	(a) Open quantum systems consider a small system $S$ coupled to a system $B$ with many degrees of freedom, called bath or environment. (b) The spin boson model (SBM) describes an open quantum system, where the system $S$ is a single spin and all modes of the bath $B$ are bosonic. . . . .	57
2.37	The bath drives two types of decoherence processes in the qubit. Relaxation is governed by interactions at the transition frequency of the qubit, thus $S(\omega = \omega_{qb})$ is of special interest in this case. Dephasing is mainly caused by interactions at low frequencies, $S(\omega \rightarrow 0)$ , which are not driving state transitions. . . . .	59
2.38	(a) Functional dependence of $\Gamma_{\varphi}(\omega_{qb})$ if caused by white-, compared to $1/f$ -noise. (b) The spectral distribution characterizes noise sources. The Ornstein-Uhlenbeck model smoothly interpolates between its limiting cases $1/f$ , and white noise by introducing a parameter $\kappa$ (see Sec. 2.5.3 for details). . . . .	63
3.1	Fabrication steps for Nb structures. . . . .	66
3.2	Double-angle shadow evaporation process to make nanoscale Josephson junctions. Process steps are shown from left to right. Top: Resist system, Bottom: Material layers on the substrate (Figure used with kind permission of Jan Goetz). . . . .	68
3.3	Quadrature hybrid design: (a) Design of whole chip, (blue...Nb structures, white...substrate), (b) Photograph of the sample chip, (c) Detail with T-junction and CPWs of $50\ \Omega$ and $35.4\ \Omega$ characteristic impedance, respectively. (d) Optical micrograph of same detail as in (c). . . . .	69
3.4	Interferometer: (a) In the design (blue...Nb structures, white...substrate) it is clearly recognizable that the interferometer is composed of two beam splitters (yellow rectangles), (b) On the sample picture we see that again on-chip wire bonds are used to ensure a good electrical connection between all parts of the ground plane. . . . .	70
3.5	Transmon qubit in $\lambda/4$ resonator: (a) Chip design (blue...Nb structures, green...Al structures, white...substrate). The yellow rectangle marks the position of the transmon qubit. (b) Zoom onto the transmon circuit (green...Al structures, white...substrate). Red rectangles mark the position of Josephson junctions (c) Micrograph of transmon qubit. Black: SQUID loop. Red: Finger capacitors of the transmon structure, (d) Mask layout of a Josephson junction. (e) SEM image of a Josephson junction. . . . .	71

3.6	Transmon qubit in interferometer. Left: (a/c/e) Design and details (designs: blue...Nb structures, green...Al structures, white...substrate), Right: (b/d/f) Photographs of sample chip, micrograph of transmon qubit and SEM image of a Josephson junction. Left and Right are to the same scale. . . . .	72
3.7	Setup of the experiment including cryogenics, cabling, etc. Left: Schematic, Right: Photograph. . . . .	75
3.8	(a) Sample box with details: (b) Mode confinement for CPW-lines on PCB. (c) Surface mount connectors. . . . .	76
3.9	(a) PCB with surface mount connectors and CPW-lines. (b) Box with connectors directly mounted on sample chip with silver glue. (c) Close-up on the transition from the PCB to the sample chip. Center conductors and ground planes are connected by wire bonds. . . . .	77
3.10	(a) The sample box is connected to the microwave lines via SMP connectors. (b) Cryoperm shield. Inner Al-shield and sample box are not visible in (b). . . . .	78
3.11	(a) Measurement paths for an interferometer (b) We scan a frequency window of $\omega_{\text{qb}}/(2\pi) \pm 100$ MHz at different qubit working frequencies $\omega_{\text{qb},i}$ . A calibration is conducted for each scan, with the qubit frequency set to $\omega_{\text{qb-cal},i}$ . . . . .	80
3.12	Measurement and fit of transmission magnitude and phase for S-parameter $S_{12}$ around a center frequency of $\omega_{\text{qb},0}/(2\pi) \approx 6.735$ GHz. . . . .	82
4.1	(a) Schematic for the beam splitter ports and measured scattering parameters. Red - cross transmission $S_{12}$ , blue - straight transmission $S_{32}$ , and green - isolation $S_{42}$ . (b) Cartoon of sample chip. The CPWs intersect the ground plane and create a floating island in the middle of the chip (red). . . . .	84
4.2	Effect of “floating island” in the middle of the beam splitter chip. Solid black lines represent the transmission magnitude (Tr. Mag.) of an ideal beam splitter spectrum, dashed colored lines simulated data with an island of undefined potential and solid colored lines simulation data for the island connected to the outer CPW ground planes (a) Red - Cross transmission $S_{12}$ , (b) Blue - Straight transmission $S_{32}$ , and (c) Green - Isolation transmission $S_{42}$ . The horizontal dashed line marks the 50 percent signal attenuation, the vertical dashed line the beam splitter design frequency $\omega_{\text{BS}}$ . . . . .	85
4.3	The measured spectrum of the beam splitter is close to theory in the frequency range marked green around the working frequency and qualitatively follows the expected behavior for other frequencies. . . . .	86
4.4	(a) Schematic of the interferometer with ports and S-parameters. Cross transmission ( $S_{12}$ and $S_{34}$ ) and straight transmission ( $S_{14}$ and $S_{32}$ ). (b) Cartoon of sample. We can identify three islands not connected to the other ground planes (red). . . . .	87

4.5	Comparison of interferometers with transmission lines of different length $l$ in between the two constituting beam splitters. Transmission magnitude is shown for $l = 4.0 \text{ mm} < \lambda/4$ (solid lines) and for a length $l = 6.0 \text{ mm} > \lambda/4$ (dashed lines), where $\lambda/4 = 5.2 \text{ mm}$ . . . . .	88
4.6	Transmission magnitude vs. frequency for the interferometer ( $l = 5.2 \text{ mm} = \lambda/4$ ) in the frequency range from 2.5 – 9 GHz, measured at liquid helium temperature. . . . .	89
4.7	(a) Schematic of the transmon qubit in a resonator. Transmission is measured via the $S_{21}$ -parameter. (b) Photograph of sample in a box with SMA-connectors. . . . .	90
4.8	Reevaluated from Ref. [49]: (a) Qubit anharmonicity (b) Josephson energy $E_J$ and asymmetry parameter $d$ (see Sec. 2.4.3). (c) Avoided crossing (d) Qubit-resonator coupling . . . . .	91
4.9	Flux dependence of the transmon qubit transition frequency measured by a resonator using two-tone spectroscopy [49]. Diamonds: data. Lines: fits (see Qubit-resonator coupling in Sec. 2.4.3). Inset: Region around the avoided crossing with more data points using single-tone spectroscopy. . . . .	91
4.10	(a) Schematic for the interferometer with a transmon qubit in one arm, ports and measured S-parameters. (b) Sample mask with zoom on transmon qubit circuit (blue...Nb structures, green...Al structures, white...substrate). Red rectangles show the positions of the JJs. . . . .	93
4.11	(a) Data and fit of magnitude (in linear units) and phase for a cross transmission measurement for $\omega_{\text{qb}}/(2\pi) \approx 6.735 \text{ GHz}$ . (b) The spectrum of the bare interferometer can be obtained by combining the information of all calibration measurements (not all data points are shown in this plot). . . . .	94
4.12	Autler townes splitting. (a) Bare states vs. dressed states resulting from strong driving of the first qubit transition. (b) The frequency of the second qubit transition $\omega_{\text{ef}}$ is obtained by measuring the Autler Townes splitting. . . . .	95
4.13	Resonance fluorescence spectroscopy: Cross transmission magnitude as a function of frequency and coil current. The black line is a fit to the deviations in the calibrated spectrum of the DUT caused by the transmon qubit using Eq. (2.86). . . . .	96

4.14	(a) Cross (red) and straight (light blue) transmission magnitude (Tr. mag.) in linear units as a function of the probe frequency for the bare interferometer in theory. (b) Measured cross transmission magnitude (Tr. mag.) in linear units and phase in rad as a function of the probe frequency at three different qubit transition frequencies $\omega_{\text{qb}}/(2\pi) = 4.556 \text{ GHz}$ , $5.826 \text{ GHz}$ , and $7.288 \text{ GHz}$ . The solid lines show the results of a fits of our transfer matrix model (see Eq. 2.107) to the data. The fits are in good agreement with the experiment. (c) Measured straight transmission magnitude and phase at the same qubit transition frequencies. Evidently the dip and peak structure near $\omega_{\text{IF}}/(2\pi) = 5.75 \text{ GHz}$ is inverted. . . . .	98
4.15	Fitted relaxation rate for different qubit working points. The red line shows a fit to an Ohmic line. A Lorentzian accounts for the observed rise in $\Gamma_1$ above 8 GHz. . . . .	100
4.16	Single tone measurements for transmon qubit in resonator. . . . .	101
5.1	Sketch of a possible C-phase gate implementation for quantum computing with propagating microwaves in the spirit of all-optical quantum computing. Black lines indicate waveguides, gray boxes beam splitters and black boxes with $\varphi(n)$ inside represent phase shifters. One dual-rail encoded (DRE) qubit and the gate are highlighted by yellow boxes. . . . .	105
A.1	(a) Setup for measurements in a Helium bath cryostat. (b) Photograph of sample stick with a sample box mounted at the bottom (Pictures with kind permission of Christian Schneider). . . . .	121
A.2	Schematic overview of a wet dilution refridgerator at WMI (Pictures with kind permission of Jan Goetz). . . . .	122
A.3	Photograph of a dry dilution refridgerator at WMI (Used with kind permission by Achim Marx). . . . .	124
B.1	Equivalent circuit for an LC-resonator. . . . .	125
B.2	All nodes in this equivalent circuit are marked in red. Ground is marked with $o$ , without loss of generality we set $\Phi_o = 0, Q_o = 0$ . . . .	126
B.3	KCL: The sum of the currents flowing out a node equals the sum of incoming currents ( $I_1 + I_2 + I_3=0$ ). . . . .	127
B.4	Equivalent circuit for a Cooper pair box (CPB). Compared to the lumped element resonator circuit, in the CPB circuit, we replace the linear inductance ( $L_r$ in Fig. B.1) by the nonlinear Josephson inductance $L_J$ . . . . .	131
B.5	KCL: The sum of the currents flowing out a node equals the sum of incoming currents ( $I_1 + I_2 + I_3=0$ ). . . . .	132
B.6	Equivalent circuit for a transmon qubit. Compared to the Cooper pair box, in this circuit, we add a shunt capacitor $C_{\text{sh}}$ . . . . .	133

- D.1 (a) 3D model of a piece of a coplanar waveguide (CPW), (b) front view of CPW, green: superconducting material, grey Si-substrate,  $t$ ...thickness of superconducting film,  $h$ ...height of substrate,  $g$ ...gap width,  $w$ ...width of center conductor, (c) Electrical field lines (blue) in a coplanar waveguide (green). . . . . 141
- D.2 To model a transmission line, it is cut into pieces and every piece is modeled as LC-resonator. Letting the length of the pieces go to zero  $\Delta x \rightarrow 0$  we end up with an infinite series of LC-resonators. . . . . 142

# List of Tables

2.1	Formal analogy between LC-resonator and particle in a harmonic potential. We can see that the structure of the terms is similar. . . .	36
3.1	CPW design parameters of beam splitter lines with an impedance of $50\ \Omega$ and $36.4\ \Omega$ . . . . .	69
4.1	Parameters of the transmon qubit, based on a reevaluation of the data obtained by Javier Puertas [49]. . . . .	92
B.1	Circuit nodes and branches of circuit shown in Fig. B.1. The symbol "#" stands for node label, which can be $o$ , $a$ or $b$ or branch number, which can be 1, 2, 3, or 4. . . . .	126
B.2	Relations between descriptive variables gained from circuit topology and branch BCEs. The symbol "#" stands for node label, which can be $a$ or $b$ or branch number, which can be 1, 2, 3, or 4. . . . .	128
B.3	Relations between descriptive variables gained from circuit topology and branch BCEs. The symbol "#" stands for node label, which can be $a$ or $b$ or branch number, which can be 1, 2, 3, or 4. . . . .	132
C.1	Energy of capacitor and inductor . . . . .	138



# Chapter 1

## Introduction

Since the first descriptions of physical effects in the framework of quantum mechanics, its specific predictions have been verified in many experiments in modern physics. These experiments have led to what is meanwhile called the first quantum revolution, coming together with huge technological progress. The resulting technologies heavily influence our daily life. Almost everybody uses a cell phone based on transistors or navigates based on global positioning systems. People rely on nuclear magnetic resonance for medical imaging. Coherent light sources (lasers) are used for broadband communication. The entertainment industry uses lasers for, e.g., projections, compact discs, digital versatile discs, and blu-ray discs. Even such simple things as a holding magnet cannot be understood without the concepts of quantum mechanics. All these technologies are based on a fundamental understanding of quantum mechanics, in most cases especially on the interaction between electromagnetic radiation and matter.

In these days, we are in the middle of a second quantum revolution[1], in which not solely understanding the effects of quantum mechanics, but the direct control of quantum mechanical processes is in the focus. This will allow for incredibly accurate devices in quantum sensing, new materials and drugs enabled by quantum simulations, unbreakable security in quantum communications, and exponentially growth in the complexity of problems solved in quantum computing. For all of these areas, superconducting quantum circuits provide a promising platform for important reasons. First, they show quantum mechanical effects on a mesoscopic level, their fabrication is based on scalable thin film technology and they are operated at frequencies of several gigahertz, used in mobile telecommunications (LTE, WiFi, ...). Second, although superconducting circuits have to be operated at temperatures

well below 100 mK, the required effort is still reasonable. In practice, one employs dilution refrigerators, which meanwhile are commercially available. Due to these two factors, superconducting circuits provide good experimental accessibility and have become a key player in the field of quantum science and technology. In the last decade, also the quantum properties of the microwave signals emitted from these circuits have become a popular object of study. The related experiments can be divided into two major groups. In one of them, the focus is put on the implementation of continuous-variable quantum protocols [2–7]. The other group aims at realizing scattering experiments with a quantum system using either microwave photons in a discrete-variable description or quasi-classical coherent states as probe signals [8–14]. The latter set of experiments, to which also this work contributes, is closely related to the concepts of generation, routing, manipulation, and detection. These areas have been actively explored in photonics at optical frequencies and are therefore often referred to as microwave quantum photonics [15].

In this work, we study the scattering of an incident microwave field off an artificial atom placed in a broadband, but nevertheless carefully engineered, open quantum circuit. In theory, such a system can be described in the framework of the spin-boson model [16, 17]. In this model description, the relaxation and dephasing rates of the qubit are determined by the spectral function of the electromagnetic environment. Therefore, measuring the qubit relaxation and dephasing rates over a wide range of the qubit transition frequencies allows one to obtain valuable information on the environment.

Especially in the areas of quantum sensing, quantum simulation, and quantum computing, the understanding of the interaction of quantum mechanical systems with their environment is of essential importance, even if it is a dissipation channel. Understanding dissipation is a key to quantum sensing applications. For quantum simulations, this loss of information may introduce dynamics that harms the model to be simulated. In quantum computing, such a dissipation channel is a significant source of decoherence. In both cases, a detailed understanding is the first step to mitigate the problem. This thesis will contribute to the field of quantum microwave photonics by investigating the interaction of a two-level system implemented in superconducting microwave circuits with a broadband environment modeled within the framework of the spin-boson model. Specifically, we couple a transmon qubit to an on-chip microwave interferometer. Using the qubit as a probe, we extract information on the structure of the environment from the relaxation and dephasing rates. As mentioned before, our results are of high interest in quantum microwave

sensing and quantum microwave communications, where interaction with broadband environments might obscure results, if not handled properly.

This work is structured as follows. Chapter 2 introduces quantum microwave photonics and the theoretical framework used to describe the measurements conducted. Chapter 3 describes the experimental techniques used to obtain the measurement data, including cryogenics and fabrication of sample chips. In Chapter 4, the measurements are presented, while in Chapter 5, a summary and an outlook are given.



# Chapter 2

## Quantum microwave photonics

The field of quantum microwave photonics aims at generating, routing, and manipulating propagating microwave fields in the spirit of optical photonics [15] at a quantum level. Whereas optical photonics uses mostly lasers and atomic systems, in microwave photonics, the radiation is controlled by electrical circuits and coaxial cables. Electrical circuits can be engineered to imitate the properties of atoms when interacting with the electromagnetic field of microwaves and thus are called *artificial atoms*. By this, in the recent years, it has become possible to investigate strong interaction [18] between electromagnetic radiation and matter at the single photon level and gain deep experimental insight into quantum electrodynamics (QED). This development has opened the door for new applications in quantum technologies such as quantum computers and quantum sensors [19–21].

In this chapter, we first introduce the transfer matrix formalism as a convenient method for modeling scattering experiments. We then describe the various microwave circuits used within this thesis at the level of a classical model. Afterwards, the quantization of these circuits is discussed along with the quantum mechanical model of a transmon qubit. Finally, we look into modeling open quantum systems, composed of the components described earlier, and their decoherence properties.

### 2.1 Transfer matrix formalism

In microwave as well as in optical photonics, we investigate interactions between electromagnetic radiation and matter which can be described as a wave signal being scattered by a potential. The transfer matrix formalism [22] is used to describe the relation between the incident and reflected propagating electromagnetic waves, resulting from the interaction with a scattering potential. This method can be

used to describe electric circuits based on the transfer matrices of their fundamental components. Proper parametrization allows for the description of both elastic (energy-conserving) and inelastic (dissipative) processes. Here, we first introduce the closely related scattering parameters ( $S$ -parameters) constituting the scattering matrix [23, 24], which is holding information equivalent to the one of the transfer matrix. We want to analyze a microwave network with  $N$  ports, where, at each port, we are interested in the voltage  $V_i$  and current  $I_i$  at a reference plane  $T_i$  (see Fig. 2.1). We assume that for each port, the microwave voltages  $V_i(z, t)$  and currents

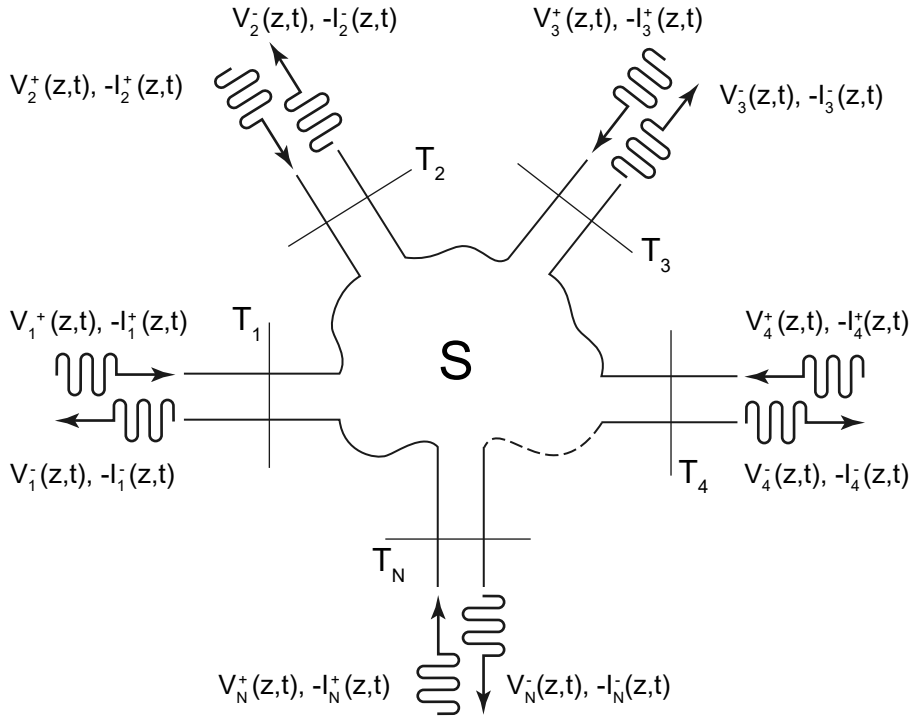


Figure 2.1: Transmission and reflection  $S$ -parameter for a device with  $N$  ports. We are interested in the voltages  $V_i$  and currents  $I_i$  evaluated at reference planes  $T_i$ . Figure with kind permission of Christian Schneider [25].

$I_i(z, t)$  at position  $z$  in the connected microwave line and time  $t$  are described by phasors, which are defined as linear combinations of incident and reflected waves:

$$V_i(z, t) = V_i^+(z, t) + V_i^-(z, t) = V_{i,0}^+ \cdot e^{-\gamma z - i\omega t} + V_{i,0}^- \cdot e^{\gamma z - i\omega t} \quad (2.1)$$

$$I_i(z, t) = \frac{1}{Z_0} (V_i^+(z, t) - V_i^-(z, t)) = I_{i,0}^+ \cdot e^{-\gamma z - i\omega t} - I_{i,0}^- \cdot e^{\gamma z - i\omega t}. \quad (2.2)$$

Here, superscript  $+$  denotes an incident wave, while superscript  $-$  denotes a reflected wave and by convention the reflected current is multiplied by  $(-1)$ . Further,  $\gamma = \alpha + i\beta$  is the complex propagation constant, consisting of the real attenuation

constant  $\alpha$  and the imaginary part  $\beta$ , called phase factor.  $Z_0$  is the characteristic impedance, with  $I = V/Z_0$  giving the relation between voltage and current. We need to distinguish between the complex wave quantity  $V_i^{+/-}(z, t)$  and its amplitude  $V_{i,0}^{+/-}$ . The notation can be simplified by skipping the second subscript for the amplitudes, thus  $V_{i,0}^{+/-}$  becomes  $V_i^{+/-}$  and is distinguished from the phasors by the lack of parameters  $V_i^{+/-} \neq V_i^{+/-}(z, t)$ ,

$$V_i(z, t) = V_i^+(z, t) + V_i^-(z, t) = V_i^+ \cdot e^{-\gamma z - i\omega t} + V_i^- \cdot e^{\gamma z - i\omega t}. \quad (2.3)$$

## S-parameters and S-matrix

In order to analyze a circuit, we need to know which output is generated by a certain input. For an N-port network, this is achieved via scattering parameters:

$$S_{ij} = \left. \frac{V_i^-(z, t)}{V_j^+(z, t)} \right|_{V_k^+(z, t)=0 \text{ for } k \neq j} \quad (2.4)$$

In the simple case of a terminated transmission line [a 1-port network, see Fig. 2.2(a)], the S-parameter  $S_{11}$  is equivalent to the reflection coefficient  $\Gamma$ <sup>1</sup>. It relates the incident part of the phasor  $V_1^+(z, t)$  of a wave traveling towards the device port, to the reflected part of the phasor  $V_1^-(z, t)$  of the wave reflected at the same port.

$$S_{11} = \Gamma = \frac{V_1^-(z, t)}{V_1^+(z, t)} \quad (2.5)$$

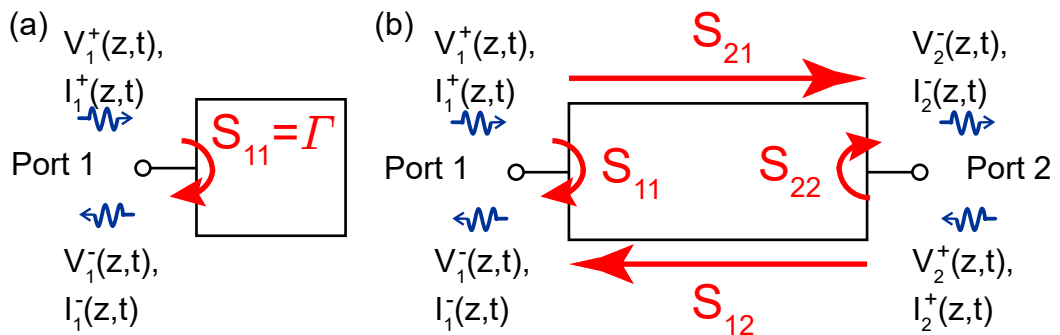


Figure 2.2: (a) The voltage phasor of the wave reflected at a terminated transmission line, which is a very simple one-port network, defines the reflection coefficient  $\Gamma = V_1^-(z, t)/V_1^+(z, t)$ . (b) The four transmission and reflection coefficients at a two-port device define a  $2 \times 2$  matrix.

<sup>1</sup>While the greek letter  $\Gamma$  is often used for rates, we follow the notation of Ref. [23] here.

For two-port networks, not only reflection, but also a transmission has to be taken into account. To do so, two reflection coefficients  $S_{11}$ , and  $S_{22}$ , one for each port and two transmission coefficients  $S_{12}$ , and  $S_{21}$ , one for each direction, are used [see Fig. 2.2(b)].

As they connect two phasors, S-parameters can take complex values. For example for a lossless two port device with a signal  $V_2^+(z, t) = V_2^+ e^{-i\beta z - i\omega t}$  entering at port 2 and exiting at port 1 as  $V_1^-(z, t) = V_1^- e^{-i\beta z - i\omega t - i\phi_{21}}$  one obtains

$$V_1^-(z, t) = S_{12} V_2^+(z, t) = \underbrace{e^{-i\phi_{21}} V_2^+}_{V_1^-} e^{-i\beta z - i\omega t}, \quad (2.6)$$

$$\text{where } S_{12} = \frac{V_1^-(z, t)}{V_2^+(z, t)} = \frac{e^{-i\phi_{21}} V_1^- e^{-i\beta z - i\omega t}}{V_2^+ e^{-i\beta z - i\omega t}} = e^{-i\phi_{21}}. \quad (2.7)$$

This simple equation tells us that the signal picks up an additional phase of  $\phi_{21}$ .

Experimentally, the S-parameter  $S_{ij}$  is determined by measuring the amplitude and phase of the wave coupled out of port  $i$ , for a known input at port  $j$ , while all other ports are terminated with matched loads (see chapter 3 for the actual setup used for experiments presented in this thesis). Exploiting the linearity of electrical circuits, we can construct a matrix relating arbitrary incident signals to the corresponding output. In this way, we know how a network will react to any input signal.

For an N-port network such as the one sketched in Fig. 2.1, evaluating the voltages at reference planes  $T_i$  yields:

$$\mathbf{V}^- = \begin{pmatrix} V_1^-(z, t) \\ V_2^-(z, t) \\ V_3^-(z, t) \\ \vdots \\ V_N^-(z, t) \end{pmatrix} = \begin{pmatrix} S_{11} & S_{12} & S_{13} & \cdots & S_{1N} \\ S_{21} & S_{22} & S_{23} & \cdots & S_{2N} \\ S_{31} & S_{32} & & & \vdots \\ \vdots & & & & \\ S_{N1} & S_{N2} & S_{N3} & \cdots & S_{NN} \end{pmatrix} \begin{pmatrix} V_1^+(z, t) \\ V_2^+(z, t) \\ V_3^+(z, t) \\ \vdots \\ V_N^+(z, t) \end{pmatrix} = \mathbf{S} \mathbf{V}^+ \quad (2.8)$$

$\mathbf{S}$  is called the scattering matrix.

## Definition of the T-Matrix

The transfer matrix  $\mathcal{T}$  allows to overcome an disadvantage of the scattering matrix  $\mathbf{S}$ , when it comes to find a scattering matrix describing a series of devices whose

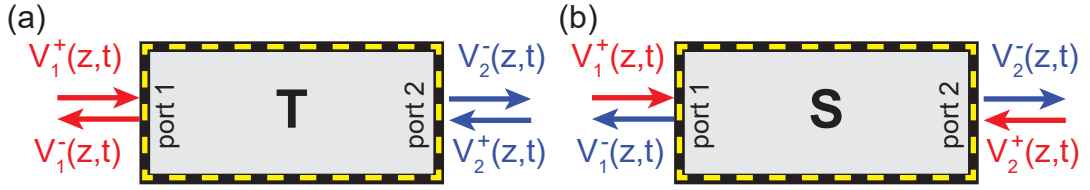


Figure 2.3: (a) A transfer matrix relates the waves at the input port (red) of a device to waves at the output port(s) (blue). (b) In contrast, a scattering matrix connects all incident waves (red) to all rejected waves (blue), regardless of the port.

individual matrices are known. As the scattering matrix  $\mathcal{S}$  connects all incident waves to all reflected waves [see Fig. 2.3(b)], it is not straightforward to matrix-multiply two or more S-matrices to obtain a matrix reflecting the relation between input ports and output ports of two devices put in series (see Fig. 2.4). The S-Matrix connects incident to reflected waves regardless of the port. Usually one or more ports of a device are defined as input, and one or more as output and this output is input for the next device in a series of connected devices. To overcome this, the transfer matrix  $\mathcal{T}$  connects all modes at the input ports, incident and reflected, of a device (or, in general, a scattering potential) to all modes at the output ports, again incident and reflected [see Fig. 2.3 (a)]. In this way, the relation between waves at the input port of the first and the waves at the output port of the last of two or more connected components can be described by the product of two or more T-matrices [Fig. 2.4 and Eq. (2.19)]. In this context, it is important to note that individual T-matrices represent point-like effective objects properly describing all reflection/transmission properties due to the internal structure. For a 2-port device, we define the transfer matrix  $\mathcal{T}$  and the scattering matrix  $\mathcal{S}$  via:

$$\begin{pmatrix} V_2^-(z,t) \\ V_2^+(z,t) \end{pmatrix} = \mathcal{T} \begin{pmatrix} V_1^+(z,t) \\ V_1^-(z,t) \end{pmatrix} = \begin{pmatrix} T_{11} & T_{12} \\ T_{21} & T_{22} \end{pmatrix} \begin{pmatrix} V_1^+(z,t) \\ V_1^-(z,t) \end{pmatrix} \quad (2.9)$$

$$\begin{pmatrix} V_1^-(z,t) \\ V_2^-(z,t) \end{pmatrix} = \mathcal{S} \begin{pmatrix} V_1^+(z,t) \\ V_2^+(z,t) \end{pmatrix} = \begin{pmatrix} S_{11} & S_{12} \\ S_{21} & S_{22} \end{pmatrix} \begin{pmatrix} V_1^+(z,t) \\ V_2^+(z,t) \end{pmatrix} \quad (2.10)$$

A relation between S- and T-parameters can be derived using the definition of the scattering matrix [Eq. (2.10)] and written as a system of equations :

$$V_1^-(z,t) = S_{11}V_1^+(z,t) + S_{12}V_2^+(z,t) \quad (2.11)$$

$$V_2^-(z, t) = S_{21}V_1^+(z, t) + S_{22}V_2^+(z, t). \quad (2.12)$$

From Eq. (2.11), we get an explicit term for  $V_2^+(z, t)$ :

$$V_2^+(z, t) = \underbrace{\left(-\frac{S_{11}}{S_{12}}\right)}_{T_{21}} V_1^+(z, t) + \underbrace{\frac{1}{S_{12}}}_{T_{22}} V_1^-(z, t). \quad (2.13)$$

Inserting  $V_2^+(z, t)$  into Eq. (2.12) to express  $V_2^-(z, t)$  gives:

$$V_2^-(z, t) = S_{21}V_1^+(z, t) + S_{22} \left( \frac{1}{S_{12}}V_1^-(z, t) - \frac{S_{11}}{S_{12}}V_1^+(z, t) \right) \quad (2.14)$$

$$= \underbrace{\left(S_{21} - \frac{S_{11}}{S_{12}}\right)}_{T_{11}} V_1^+(z, t) + \underbrace{\frac{S_{22}}{S_{12}}}_{T_{12}} V_1^-(z, t) \quad (2.15)$$

Thus, the entries  $T_{ij}$  of the transfer matrix  $\mathcal{T}$  can be expressed by means of the scattering parameters  $S_{ij}$ :

$$\mathcal{T} = \begin{pmatrix} T_{11} & T_{12} \\ T_{21} & T_{22} \end{pmatrix} = \begin{pmatrix} S_{21} - \frac{S_{11}S_{22}}{S_{12}} & \frac{S_{22}}{S_{12}} \\ -\frac{S_{11}}{S_{12}} & \frac{1}{S_{12}} \end{pmatrix}. \quad (2.16)$$

From Eq. (2.16), we see that for devices with no reflection the anti-diagonal entries  $T_{12}$  and  $T_{21}$  of the transfer matrix are zero. This will become obvious for the transfer matrix of a transmission line [see Eq. (2.35)]. From Eq. (2.15) and Eq. (2.13) it can also be understood that  $S_{21}$  appears in  $T_{11}$ , while the inverse of  $S_{12}$  appears in  $T_{22}$ .  $T_{11}$  reflects the contribution of the incident wave  $V_1^+(z, t)$  at port 1, to the reflected wave at port 2,  $V_2^-(z, t)$ . By definition, these are related by  $S_{21} = V_2^-(z, t)/V_1^+(z, t)$ .  $T_{22}$  gives the contribution of the reflected wave  $V_1^-(z, t)$  at port 1, to the incident wave  $V_2^+(z, t)$  at port 2. By definition  $S_{12} = V_1^-(z, t)/V_2^+(z, t)$ , thus  $V_2^+(z, t) = V_1^-(z, t)/S_{12}$ . A more physical interpretation of the inverse S-parameter is the reversal of the propagation direction.

From a practical point of view, the most useful property of the transfer matrix is that two or more matrices can be concatenated via matrix multiplication to model a sequence of devices whose output ports form the input for the next device in a series (see Fig. 2.4). Here, a direct connection of the devices is assumed, otherwise information on the phase is lost and the method cannot account for interference effects as observed in double tunnel junctions. Suppose  $\mathcal{T}_1$  connects incident and

reflected waves at the input port 1 to all incident and reflected waves at the output port 2 of device  $A$ , and  $\mathcal{T}_2$  connects incident and reflected waves at the input port 3 to all incident and reflected waves at the output port 4 of device  $B$ . By using the output of device  $A$  as input for device  $B$  we can derive a transfer matrix for the series of  $A$  and  $B$  by matrix multiplication of  $\mathcal{T}_1$  and  $\mathcal{T}_2$  to connect incident and reflected waves at port 1 to the waves at port 4 (see Fig. 2.4):

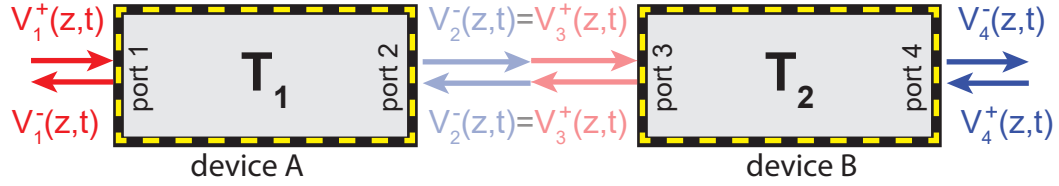


Figure 2.4: A sequence of transfer matrices can be used to model several scatterers in series. The modes at the output port (port 4) of a chain of two devices can be obtained by applying  $\mathcal{T}_1$  on the modes at the input port of the first device (port 1), which gives the modes at the output of the first device (port 2), which are use as input for the second device (port 3). Finally  $\mathcal{T}_2$  is applied to obtain modes at the output port (port 4).

$$\begin{pmatrix} V_4^-(z, t) \\ V_4^+(z, t) \end{pmatrix} = \mathcal{T}_2 \begin{pmatrix} V_3^+(z, t) \\ V_3^-(z, t) \end{pmatrix}, \quad (2.17)$$

$$\begin{pmatrix} V_3^+(z, t) \\ V_3^-(z, t) \end{pmatrix} = \begin{pmatrix} V_2^-(z, t) \\ V_2^+(z, t) \end{pmatrix}, \quad (2.18)$$

$$\begin{pmatrix} V_2^-(z, t) \\ V_2^+(z, t) \end{pmatrix} = \mathcal{T}_1 \begin{pmatrix} V_1^+(z, t) \\ V_1^-(z, t) \end{pmatrix} \quad (2.19)$$

$$\Rightarrow \begin{pmatrix} V_4^-(z, t) \\ V_4^+(z, t) \end{pmatrix} = \underbrace{\mathcal{T}_2 \mathcal{T}_1}_{\mathcal{T}} \begin{pmatrix} V_1^+(z, t) \\ V_1^-(z, t) \end{pmatrix} \quad (2.20)$$

Using the  $S$ -matrix formalism, it is not possible to decompose an  $S$ -matrix into the product of two or more  $S$ -matrices modeling several connected physical devices. Suppose  $S_1$  connects all incidents waves of device  $A$  at its ports 1 and 2 and  $S_2$  connects all incidents waves of device  $B$  at its ports 3 and 4. Furthermore suppose device  $A$  and  $B$  are connected via ports 2 and 3 (see Fig. 2.4 for transfer matrices and Fig. 2.5 for  $S$ -matrices). By defining an  $S$ -matrix of the composite device, constituted by the two individual devices put in series, we connect the incident waves

$[V_1^+(z, t), V_4^+(z, t)]$  to the reflected waves  $[V_1^-(z, t), V_4^-(z, t)]$ . An  $S$ -matrix for device  $B$  connects  $[V_3^+(z, t), V_4^+(z, t)]$  to  $[V_3^-(z, t), V_4^-(z, t)]$  and an  $S$ -matrix for device  $A$  connects  $[V_1^+(z, t), V_2^+(z, t)]$  to  $[V_1^-(z, t), V_2^-(z, t)]$ . Thus, the  $S$ -matrix for the composite device cannot be obtained by multiplication of the individual  $S$ -matrices of the device  $A$  and device  $B$ , as  $S_2$  cannot be applied to  $[V_1^+(z, t), V_4^+(z, t)]$ , which would be needed for an  $S$ -parameter model of the composite device.

$$\begin{pmatrix} V_1^-(z, t) \\ V_2^-(z, t) \end{pmatrix} = \mathcal{S}_1 \begin{pmatrix} V_1^+(z, t) \\ V_2^+(z, t) \end{pmatrix}, \quad \begin{pmatrix} V_3^-(z, t) \\ V_4^-(z, t) \end{pmatrix} = \mathcal{S}_2 \begin{pmatrix} V_3^+(z, t) \\ V_4^+(z, t) \end{pmatrix} \quad (2.21)$$

$$\Rightarrow \begin{pmatrix} V_1^-(z, t) \\ V_4^-(z, t) \end{pmatrix} \neq \underbrace{\mathcal{S}_1 \mathcal{S}_2}_S \begin{pmatrix} V_1^+(z, t) \\ V_4^+(z, t) \end{pmatrix} \quad (2.22)$$

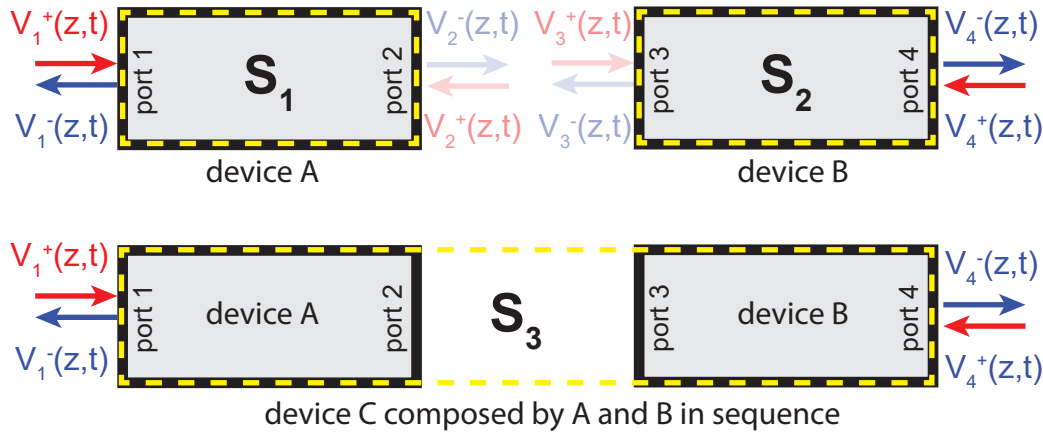


Figure 2.5: Scattering matrices **cannot** be used sequentially to model the effect of several scatterers. The scattering matrix  $\mathcal{S}_3$  connecting the incident and reflected modes of a chain of device A and B cannot be decomposed into a product of the individual  $S$ -matrices  $\mathcal{S}_1$  and  $\mathcal{S}_2$ .

## Transmission spectrum

In a typical transmission spectrum experiment, as it is often used within this thesis, we compare an incident wave at an input port, to the amplitude and phase of the same wave leaving a device under test (DUT) at the output port (see Fig. 2.6) for a range of probe frequencies. In other words, we conduct frequency-dependent  $S$ -parameter measurements. To model this situation using the transfer matrix for-



Figure 2.6: In a transmission measurement we apply a well defined signal  $V_1^+(z, t)$  at one defined input port and no signal at the other. Reflection and transmission are measured.

malism, the single incident wave is well defined by  $V_1^+(z, t)$ , while all other incident wave amplitudes are set to zero, and the system

$$\begin{pmatrix} V_2^-(z, t) \\ \mathbf{V}_2^+(z, t) = \mathbf{0} \end{pmatrix} = \begin{pmatrix} T_{11} & T_{12} \\ T_{21} & T_{22} \end{pmatrix} \begin{pmatrix} \mathbf{V}_1^+(z, t) \\ V_1^-(z, t) \end{pmatrix} \quad (2.23)$$

is solved for the transmitted and reflected phasors  $V_2^-(z, t), V_1^-(z, t)$ . For more complex systems, such as beam splitters or interferometers treated in the thesis, the matrix will be of higher dimension, but still exactly one incident signal is well defined and the system is solved for the reflected signals at all other ports. It also needs to be remarked, that in most cases only the amplitude and phase of transmitted waves are experimentally accessible due to the technical effort of implementing reflection measurements.

Together with Eq. (2.16), the measured S-parameters allow us to evaluate the frequency-dependent transfer matrix  $\mathcal{T}$  of the DUT.

## 2.2 Lumped element circuit theory

In this section, we look at the classical lumped element circuit theory for lossless circuits used throughout this thesis. We derive the Hamiltonian description of the classical dynamics of non-dissipative circuits (see Ref. [26]) in order to obtain the equations of motion for circuit elements. Although textbook knowledge it is useful to revisit this in preparation of Sec. 2.4, where the quantum mechanical description of circuits is obtained by a promotion of the classical conjugate variables to operators. Finally, comparing the mathematical structure of the circuit to the one of an atom motivates using these circuits as artificial atoms (see App. C).

The lumped element circuit model describes the dynamics of voltage and current in electronic circuits based on the assumption that the internal structure of circuit elements can be neglected. For basic elements such as capacitors, Josephson junctions, and inductors, used in the experiments performed in this thesis, this assumption is legitimate, as their electric circuit structure size is on the order of micrometers and below, which is small compared to the wavelengths of the microwaves propagating in the circuits, which is on the order of centimeters.

An electrical circuit is represented by a network of elements connected via nodes [see Fig. 2.7(a)]. We restrict our consideration to circuit elements with two terminals only, such as capacitors and inductors.

We will use the nodal analysis method [27] and the Lagrange formalism to solve the circuit. Here, solving means to obtain the equations of motion for each circuit element. To do so, we have to:

1. Create a **circuit diagram** of elements with two terminals and identify nodes and branches.
2. Introduce the **descriptive variables** of the system and assign a set of descriptive variables for each node and circuit element.
3. Use Kirchhoff's current law (KCL) and branch constitutive equations (BCE) to obtain a **system of equations** describing the circuit (Nodal analysis [27]).
4. Derive a classical **Hamiltonian** by finding the system Lagrangian and applying Legendre transformations.

This procedure is reviewed in detail for a capacitively coupled LC-resonator and the Cooper pair box in App. B.

## Circuit diagram

A circuit diagram or equivalent circuit is a graphical representation of the physical circuit made of three constituents: Circuit elements, nodes and branches [Fig. 2.7(a)]. A *circuit element* is represented in the diagram by a specific circuit symbol [see

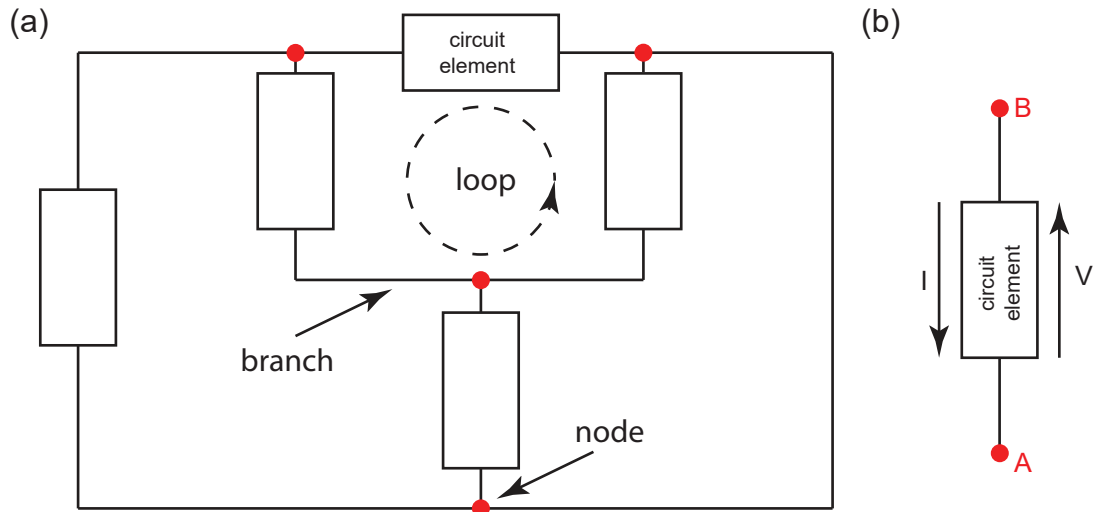


Figure 2.7: (a) An electric circuit is represented by a network of elements. We restrict our considerations to elements with two terminals. The connection between the elements is drawn as line and constitutes a branch. Branches meet at nodes (red dots). Nodes that can be reached via different paths form loops. (b) Single circuit element, for which the voltage drop  $V$  and the current intensity  $I$  are investigated. The reference directions for current and voltage are reflected by the orientation of the associated arrows. Although both can be chosen at will, it is standard to have opposite reference orientation for voltage and current.

[Figs. 2.7(b), 2.9, and 2.10 for examples]. The connection between two circuit elements is drawn as a line.

A *node* is the intersection of the lines connecting different circuit elements.

A *branch* is defined as the connection and the element between two nodes.

As we are using a lumped element model, the lines (wires) between circuit elements are not taken into account, despite the fact they define the interconnection between the different elements and thus the topology of the circuit.

## Descriptive variables

For each element of a circuit, the time evolution of the voltage-drop  $V(t)$  at the element and the electric current  $I(t)$  flowing through it are of interest. Thus,  $I$  and  $V$  are called the dynamic or descriptive variables. Figure 2.7(b) shows a generic

circuit element connected to nodes A and B. Here, alternatively to voltage  $V$  and current  $I$ , the magnetic flux induced in the branch  $\Phi$  and the charge  $Q_i$  as defined in Ref. [28] will be used:

$$\Phi(t) = \int_{-\infty}^t V(t') dt' \quad (2.24)$$

$$Q(t) = \int_{-\infty}^t I(t') dt', \quad (2.25)$$

Using these variables is advantageous when building a Lagrangian function.

## Nodal analysis

The nodal analysis provides a systematic way to obtain the dynamics of the descriptive variables for each element contained in the circuit. It utilizes Kirchhoff's Voltage Law [KVL, see Fig. 2.8(b)] and Kirchhoff's Current Law [see Fig. 2.8(c)] to obtain a set of equations relating the descriptive variables based on the topology of a circuit.

## Branch constitutive equations

The equations obtained from the nodal analysis alone do not provide sufficient information to extract all descriptive variables. Thus, also branch constitutive equations (BCE), reflecting the actual physics of a circuit element, are taken into account. The BCE can also be a differential equation. To find the respective differential equations, we are able to build a set of  $N$  equations in  $N$  variables and obtain a solution for the circuit. In the following, we give the descriptive equations (aka BCE) for capacitors and inductors.

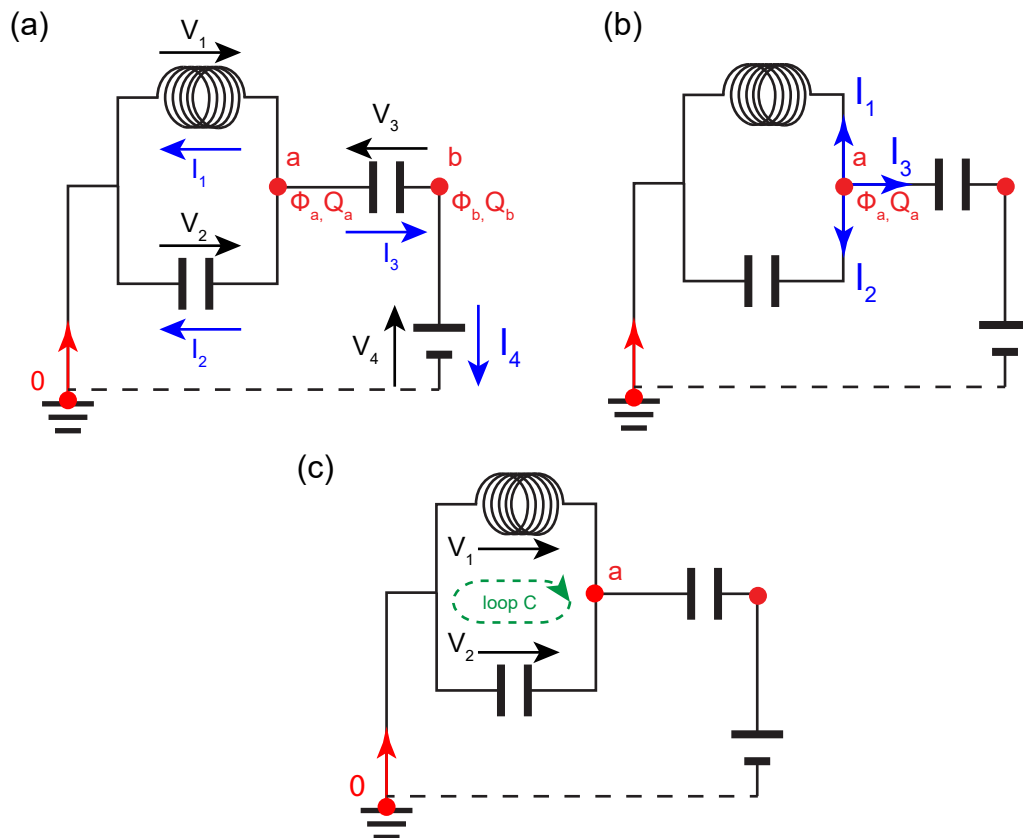


Figure 2.8: (a) A circuit diagram is used to do a nodal analysis, which is a systematic way to find a set of equations relating the descriptive variables of a circuit. (b) KCL is used to relate currents flowing in or out of nodes. Node a:  $I_1 + I_2 + I_3 = 0$ . (c) KVL is used to relate the voltages drops across circuit elements within loops. Loop C:  $V_1 - V_2 = 0$ .

## Capacitor

A generic capacitor is modeled as a plate capacitor. Voltage  $V$  and current  $I$ , respectively flux  $\Phi$  and charge  $Q$ , are related via the capacitance  $C$ :

$$I = C \frac{d}{dt} V \iff \dot{Q} = C \ddot{\Phi} \quad (2.26)$$

The energy  $E_{\text{Cap}}$  stored in this element is stored in the electric field and given as

$$E_{\text{Cap}}(\Phi) = \frac{1}{2} C V^2 = \frac{C}{2} \dot{\Phi}^2 \quad (2.27)$$

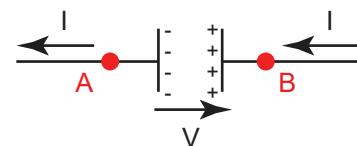


Figure 2.9: Circuit diagram symbol for a capacitor with  $I$  and  $V$  depicted.

## Inductor

For a general inductor, voltage and current, respectively flux and charge, are related via the inductance  $L$ :

$$V = L \frac{dI}{dt} \iff \dot{\Phi} = L\dot{Q} \quad (2.28)$$

Here, the energy  $E_{\text{Ind}}$  is stored in the magnetic field caused by the current flowing through the inductor:

$$E_{\text{Ind}} = \frac{1}{2}LI^2 = \frac{\Phi^2}{2L}. \quad (2.29)$$

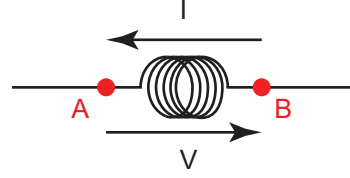


Figure 2.10: Circuit diagram symbol for an inductor with  $I$  and  $V$  depicted.

Equation (2.28) and Eq. (2.26) are the BCE reflecting the actual physics of the corresponding circuit elements. Together with the equations derived from the topology of the circuit by KVL and KCL, a system of equations of sufficient order to solve for all descriptive variables of the circuit can be stated [27].

## System Hamiltonian

The above procedure leads to a system of  $N$  equations with  $N$  unknowns, thus can be solved with linear algebra. From the electrical engineering point of view, we have all the required input to fully describe the system under test. As we are interested in the physics of the system, we will use the result to obtain a description of the system in terms of a Hamiltonian by defining a Lagrangian function and deriving the Hamiltonian from it. The Lagrangian function is defined as:

$$\mathcal{L} = T - U, \quad (2.30)$$

where  $T$  is the kinetic energy and  $U$  is the potential energy in the system. Now, the dynamics of the system then is obtained by the Euler-Lagrange equation:

$$\frac{d}{dt} \frac{\partial \mathcal{L}}{\partial \dot{Q}} = \frac{\partial \mathcal{L}}{\partial Q}. \quad (2.31)$$

Finally, the classical system Hamiltonian can be derived by use of the conjugate momenta and the Lagrangian

$$H = Q\dot{\Phi} - \mathcal{L}. \quad (2.32)$$

## Lumped element LC resonator

Investigating a first more complex circuit, we look at a lumped element parallel LC resonator, constituted of an inductance  $L_r$  and a capacitance  $C_r$  in parallel. This circuit is shown in Fig. 2.11(a) and has a resonance frequency  $\omega_0 = \frac{1}{\sqrt{L_r C_r}}$ . Its dynamics is obtained by the method explained earlier, a detailed discussion is given in appendix B.1. By adding a drive to the circuit, such as a microwave source, its physics is in full analogy to the driven, damped harmonic oscillator[29]. The LC resonator has maximum transmission at  $\omega_0$ , while for other frequencies it suppresses the transmission of signals. The full width at half maximum is denoted  $\Delta\omega$  and gives the bandwidth of the resonator, if coupled to a transmission line. Near resonance, the transmission spectrum can be approximated by a Lorentzian [see Fig. 2.11(b)]. In the absence of damping ( $\Delta\omega \rightarrow 0$ ), the resonator supports only a single microwave mode.

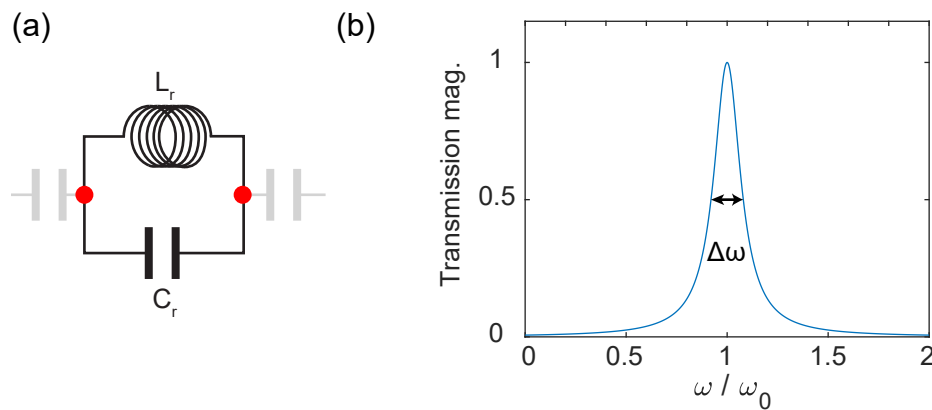


Figure 2.11: (a) Equivalent circuit for a LC-resonator consisting of an inductance  $L_r$  and a capacitance  $C_r$  with a resonance frequency  $\omega_0 = \frac{1}{\sqrt{L_r C_r}}$ . In shaded grey we see how this circuit can be integrated to another via coupling capacitors. Resistive elements, introducing damping to the system, are not modeled. (b) Typical Lorentzian shaped transmission magnitude spectrum for a damped resonator.

Next, we want to find the system Lagrangian  $\mathcal{L}_{LC}$ . We chose to attribute kinetic energy to capacitors,  $T = (C/2)\dot{\Phi}^2$  [see Eq. (2.27)], and potential energy to inductors,

$U = \Phi^2/(2L_r)$  [see Eq. (2.29)]. We get

$$\mathcal{L}_{\text{LC}} = T - U = \left( \frac{C_r}{2} \dot{\Phi}^2 - \frac{1}{2L_r} \Phi^2 \right). \quad (2.33)$$

Using charge  $Q = \partial\mathcal{L}/\partial\dot{\Phi} = C_r\dot{\Phi}$  and flux  $\Phi$  as descriptive variables and applying the Legendre transformation  $H = Q\dot{\Phi} - \mathcal{L}$ , the classical Hamiltonian is found to be

$$H_{\text{LC}} = \frac{Q^2}{2C_r} + \frac{\Phi^2}{2L_r}. \quad (2.34)$$

## 2.3 Classical lossless circuits

In this section, we describe basic microwave circuits used throughout this thesis, which can be modeled without using quantum mechanics. This again can be considered textbook knowledge, but provides the model for basic building blocks used in our experiments, thus is reviewed here. In the previous section, we have made the assumption, that basic circuit elements in question are small compared to the wavelength of the microwave signals used to probe them. The structures investigated in this section are on the order of the probe signal wavelength. Basic circuit elements, such as capacitors and inductors, are still modeled as point-like scatterers. Nevertheless, the finite geometric dimensions of connecting lines do not only define the topology, but introduce parameters into the transfer matrix. This is possible, as we are not interested in wave properties inside the structures, but only in the properties of the probe signal after passing the circuit. This can be compared with detecting the resulting wave after being scattered at a potential with some internal structure (see Fig. 2.12). First, we introduce the transmission line and the transmission line

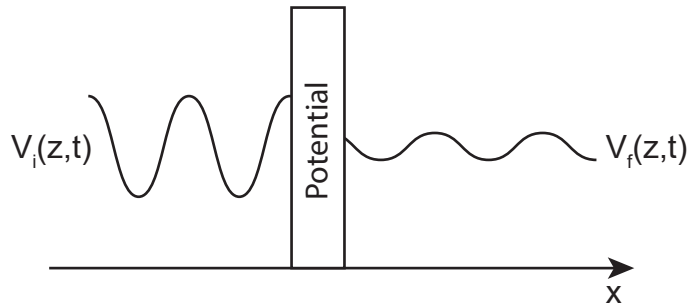


Figure 2.12: We model the effect of our circuit on a probe signal as a scattering potential acting on an incoming wave. Thus a parameterized transfer matrix  $\mathcal{T}(\vec{p})$  gives the relation between the final waveform  $V_f(z, t)$  and the initial waveform  $V_i(z, t)$ . Thus  $V_f(z, t) = \mathcal{T}(\vec{p}) \cdot V_i(z, t)$ . Here the internal structure of the potential is modeled in the parameter vector  $\vec{p}$

resonator. Then, we describe microwave circuits implementing a beam splitter and an interferometer and show their transfer matrices.

### 2.3.1 Coplanar waveguide transmission line

A transmission line (TL) is a structure designed to convey microwave frequency signals. There are several possible designs ranging from simple cables to complex 3D-structures. We focus on co-planar waveguides (CPWs) which are used in our

experiments. They provide quasi one-dimensional wave-propagation in the sense that the electrical field is confined to an area much smaller than the wavelength in two of three dimensions [23]. In CPWs, we find transverse electromagnetic (TEM) modes, where the electric field in TEM modes is oriented perpendicular to the direction of propagation. Modeling a transmission line, we have to account for its non-negligible size along the propagation direction, compared to the microwave wavelength (see App. D for further details).

### Transfer matrix

We define the transmission coefficient for a transmission line,  $t(k) = e^{-ikl}$ , with real<sup>2</sup> wave number  $k$  and length  $l$ . Here,  $k = (\omega\sqrt{\epsilon_r})/c$  with angular frequency  $\omega$  and dielectric constant  $\epsilon_r$ . This results in a phase difference for the microwave between entry point and exit point in and out of the transmission line (see Fig. 2.13). Thus, propagation of a wave in a transmission line adds a phase depending on the length of the line and results in voltage (anti-)nodes at defined positions on the line.

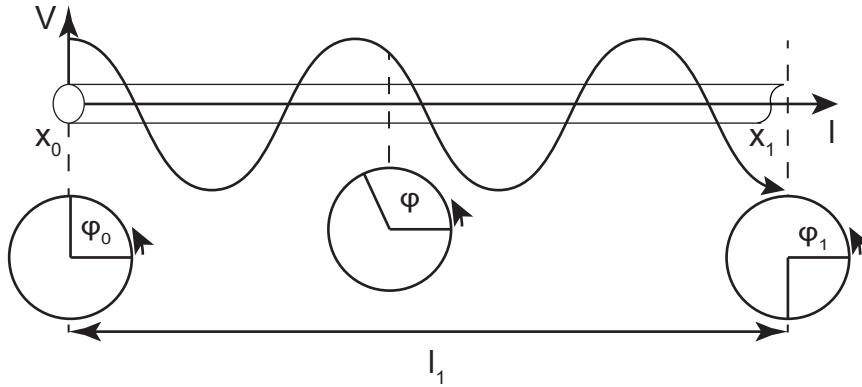


Figure 2.13: Phase of an EM wave propagating down a transmission line: At Position  $x_1$  we measure a phase-difference  $\Delta\varphi_{01} = \varphi_1 - \varphi_0$ , compared to the phase  $\varphi_0$  at position  $x_0$ . Thus,  $T_{11} = e^{-i\Delta\varphi_{01}}$  is the transfer matrix element for a TL of length  $l_1$ .

We assume a constant characteristic impedance over the transmission line, thus there is no reflection and the reflection coefficient  $r = 0$ . In this way, for the transfer matrix  $\mathcal{T}_{\text{TL},1}$ , we obtain:

$$\mathcal{T}_{\text{TL},1}(\omega, l) = \begin{pmatrix} t & 0 \\ 0 & \frac{1}{t} \end{pmatrix} = \begin{pmatrix} e^{-ikl} & 0 \\ 0 & e^{ikl} \end{pmatrix} = \begin{pmatrix} e^{-i\Delta\varphi_{01}} & 0 \\ 0 & e^{i\Delta\varphi_{01}} \end{pmatrix}, \quad (2.35)$$

<sup>2</sup>Lossless circuits, damping is discussed later.

where  $\Delta\varphi = kl = 2\pi(l/\lambda)$  is the phase difference picked up by a microwave with wavenumber  $k$  when propagating through a piece of transmission line of length  $l$ .

As in our final sample a segment of two transmission lines will be used, we define the transfer matrix of two transmission lines of equal length

$$\mathcal{T}_{\text{TL}}(\omega, l) = \left( \begin{array}{c|c} \mathcal{T}_{\text{TL},1}(\omega, l) & 0 \\ \hline 0 & \mathcal{T}_{\text{TL},1}(\omega, l) \end{array} \right) = \begin{pmatrix} t & 0 & 0 & 0 \\ 0 & \frac{1}{t} & 0 & 0 \\ 0 & 0 & t & 0 \\ 0 & 0 & 0 & \frac{1}{t} \end{pmatrix} \quad (2.36)$$

### Transmission spectrum

For the transfer matrix of a transmission line described above, the transmission magnitude simply is unity for all frequencies, as we did not incorporate any loss, which is a good approximation for superconducting circuits. The transmission phase decreases linear with frequency.

### Lossy transmission line

For real experiments, also lossy transmission lines at room temperature need to be modeled. Following Ref. [23], we define the complex propagation constant

$$\gamma = \alpha + i\beta. \quad (2.37)$$

We model the resistive components causing loss in a TL by considering a non-zero attenuation constant  $\alpha$ . This causes a frequency dependent damping of the signal propagating in a transmission line [30].

### 2.3.2 Transmission line resonator

A transmission line resonator can be fabricated by enclosing a piece of transmission line between two coupling capacitors, such as gaps in the center conductor (see Fig. 2.14). It is modeled in the same way as an LC-resonator, using an effective

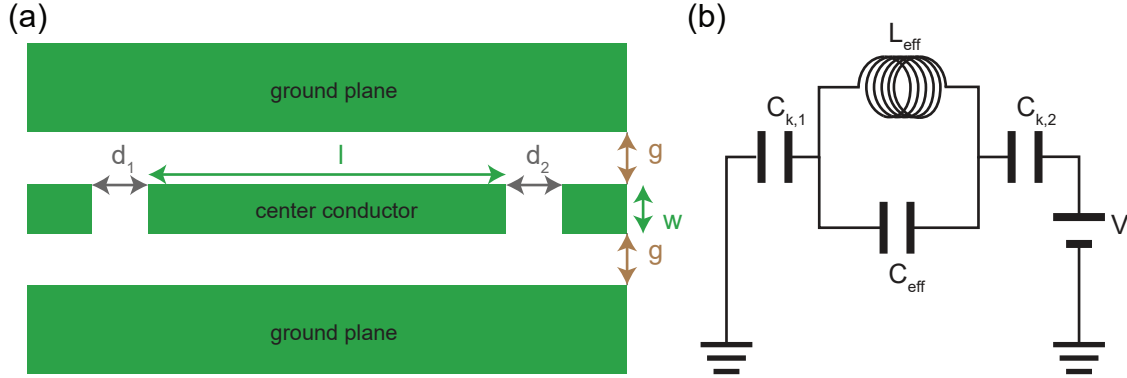


Figure 2.14: (a) Design of a half-wavelength transmission line resonator.  $g$  and  $w$  define the characteristic impedance of the TL and together with  $l$  the characteristic frequency of the resonator.  $d_{1,2}$  then define the coupling capacitors  $C_{k,1}$  and  $C_{k,2}$ . (b) Equivalent circuit for the design shown in (a).

inductance  $L_{\text{eff}}$  and an effective capacitance  $C_{\text{eff}}$ , which are mainly determined by the length of the piece of transmission line in between the coupling capacitances. In many experiments, the coupling capacitances  $C_{k,1}, C_{k,2}$  are implemented as a simple gap in the center conductor or as finger capacitor [31, 32]. As in this model dielectric losses are seen as resistive components, the theoretical description of the system comes down to a damped oscillator, even though resistance is zero in superconducting circuits [33, 34]. Close to the resonance frequency  $\omega_0$  and for high  $Q = \Delta\omega/\omega_0$ , where  $\Delta\omega$  is the full width at half maximum (FWHM) of the resonator transmission spectrum, the transmission spectrum of a TL-resonator can be approximated by a Lorentz function [32].

#### Hamiltonian

The transmission line resonator is modeled as a damped resonator with effective inductance  $L_{\text{eff}}$ , and effective capacitance  $C_{\text{eff}}$  [32]. Thus, the classical Hamiltonian is given as

$$H = \frac{1}{2C_{\text{eff}}}(Q - q_g)^2 + \frac{1}{2L_{\text{eff}}}\Phi^2. \quad (2.38)$$

---

Here,  $Q$  and  $\Phi$  are the conjugate variables for charge and flux, while  $q_g$  is the gate charge on the coupling capacitors. The resistive component is omitted for simplicity.

### 2.3.3 Quadrature hybrid beam splitter

One main building block for the experiments conducted throughout this thesis is a 50/50 beam splitter. Ideally, at the design frequency  $\omega_{BS}$ , it splits an incident wave such that half of the power goes to each of two output ports and none is reflected back. Figure 2.15 shows, one particular circuit for this task, the quadrature hybrid

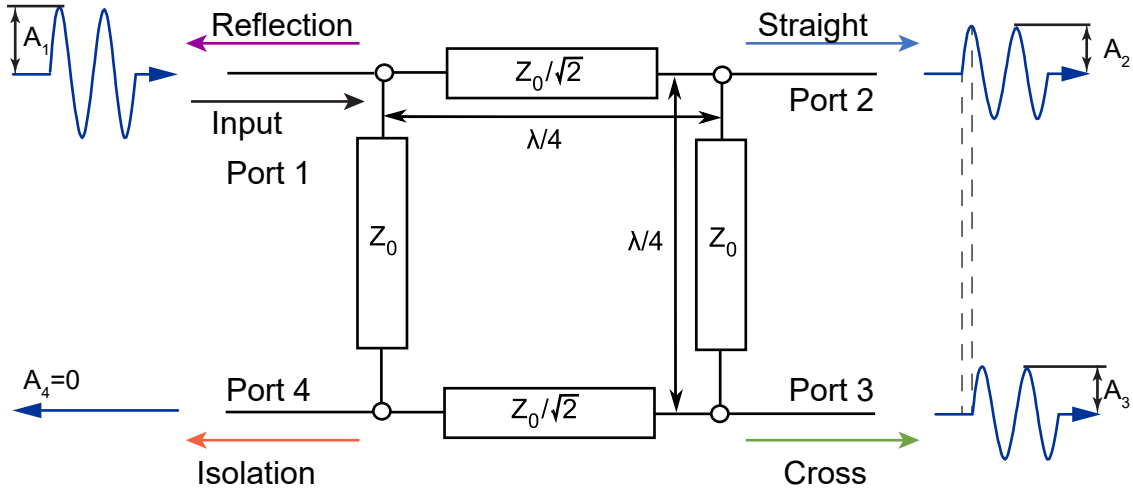


Figure 2.15: Circuit diagram of a quadrature hybrid beam splitter.

ring, a four-port device built from several T-junctions and lines of different characteristic impedance. At the design frequency  $\omega_{BS}$ , an input signal of amplitude  $A_1$  (port 1 in Fig. 2.15) is split into two outputs with  $A_{2,3} = (1/\sqrt{2})A_1$  of the original amplitude, but with a phase shift of  $90^\circ$  (ports 2 and 3 in Fig. 2.15). We make the convention to call port 2 *straight* and port 3 *cross*, due to geometry (Fig. 2.15). The length and characteristic impedance of the lines between the T-junctions is chosen such that the microwaves will constructively and destructively interfere at the output ports. As the working principle of this device relies on interference, it is frequency dependent. It has a design or working frequency  $\omega_{BS}$ , where it provides a perfect 50-50 splitting of the input signal. Fig. 2.18 shows the transmission spectrum of an ideal beam splitter.

The treatment of the Hamiltonian is omitted for beam splitter and interferometer, as it is not relevant for data analysis.

#### Transfer matrix

The transfer matrix of a beam splitter can be obtained by even-odd mode analysis[25, 35] or the transfer matrix formalism. For the latter, we start with the transfer

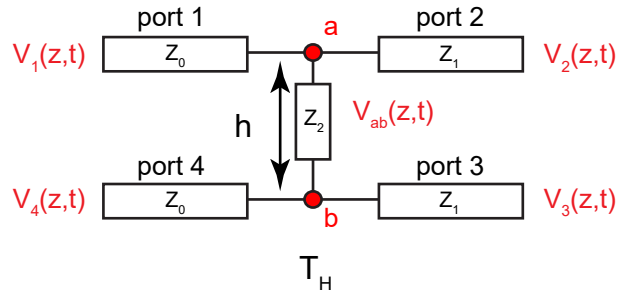


Figure 2.16: The H-section is the main building block for a microwave beam splitter. It consists of two T-junctions in nodes  $a$  and  $b$ .

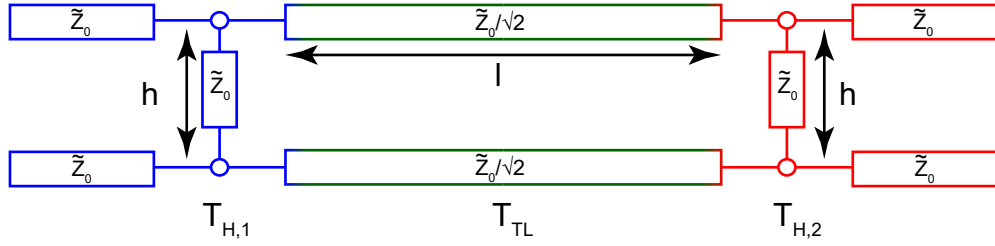


Figure 2.17: Two H-sections (blue, red) connected by two transmission lines (dark green) form a beam splitter. A theoretical description is obtained by multiplication of the according transfer matrices  $\mathcal{T}_{H,1}$ ,  $\mathcal{T}_{TL}$ , and  $\mathcal{T}_{H,2}$ .

matrix  $\mathcal{T}_H(\omega, h)$  for an H-section (see Fig. 2.16) with height  $h$ .  $\mathcal{T}_H(\omega, h)$  is derived from first principles by applying Kirchoffs rules for voltage and current. First, we define phasors [see Eq. (2.1)] for the waves in all parts of the H-section (see Fig. 2.16)

$$V_j(z, t) = V_j^+(z, t) + V_j^-(z, t), \text{ for } j = 1, 2, 3, 4, \text{ and} \quad (2.39)$$

$$V_{ab}(z, t) = V_{ab}^+(z, t) + V_{ab}^-(z, t), \quad (2.40)$$

where  $V_{ab}$  is the phasor of the microwave between nodes  $a$  and  $b$ , with  $V_{ab}^+(z, t)$  propagating towards  $b$ . The voltage phasors are continuous at each node. Thus we find a system of equations

$$V_1^+(z, t) + V_1^-(z, t) = V_{ab}^+(z, t) + V_{ab}^-(z, t), \quad (2.41)$$

$$V_1^+(z, t) + V_1^-(z, t) = V_2^+(z, t) + V_2^-(z, t), \quad (2.42)$$

$$V_4^+(z, t) + V_4^-(z, t) = V_{ab}^+(z, t)e^{-i2\pi(h/\lambda)} + V_{ab}^-(z, t)e^{i2\pi(h/\lambda)}, \quad (2.43)$$

$$V_4^+(z, t) + V_4^-(z, t) = V_3^+(z, t) + V_3^-(z, t). \quad (2.44)$$

Here,  $\lambda$  is the wavelength of the microwave signal. The spatial coordinate  $z$  is defined differently for each port. Equation (2.41) and Eq. (2.42) account for voltage phasors

in node  $a$ , while Eq. (2.43) and Eq. (2.44) account for node  $b$ . From the parameter  $h$ , giving the height of the H-section, we deduct that the wave at node  $b$  has to pick up an additional phase  $2\pi(h/\lambda)$ , compared to node  $a$ , and accounted for this in Eq. (2.43).

Second, we investigate the current phasors, whose relation is determined by the KCL. From Eq. (2.1) we know that voltage and current phasor are connected by the impedance  $Z$ . All currents in a node need to sum up to zero, thus we find two more equations

$$\frac{V_1^+(z, t) - V_1^-(z, t)}{Z_0} - \frac{V_2^+(z, t) - V_2^-(z, t)}{Z_1} - \frac{V_{ab}^+(z, t) - V_{ab}^-(z, t)}{Z_2} = 0 \quad (2.45)$$

$$\frac{V_4^+(z, t) - V_4^-(z, t)}{Z_0} - \frac{V_3^+(z, t) - V_3^-(z, t)}{Z_1} + \frac{V_{ab}^+(z, t)e^{i2\pi(h/\lambda)} - V_{ab}^-(z, t)e^{-i2\pi(h/\lambda)}}{Z_2} = 0 \quad (2.46)$$

Combining Eqs. (2.41-2.46), we find the frequency-dependent transfer matrix of a general H-section with parameters  $h, Z_0, Z_1, Z_2$  to be

$$\mathcal{T}_H(\omega, Z_0, Z_1, Z_2, h) = \begin{pmatrix} T_{H,11} & T_{H,12} & T_{H,13} & T_{H,14} \\ T_{H,21} & T_{H,22} & T_{H,33} & T_{H,24} \\ T_{H,31} & T_{H,32} & T_{H,43} & T_{H,34} \\ T_{H,41} & T_{H,42} & T_{H,43} & T_{H,44} \end{pmatrix}, \quad (2.47)$$

where

$$\begin{aligned} T_{H,11} &= \frac{(Z_0+Z_1)Z_2-iZ_0Z_1 \cot(2\pi s)}{2Z_0Z_2} & T_{H,12} &= \frac{(Z_0-Z_1)Z_2-iZ_0Z_1 \cot(2\pi s)}{2Z_0Z_2} \\ T_{H,13} &= \frac{iZ_1 \csc(2\pi s)}{2Z_2} & T_{H,14} &= \frac{iZ_1 \csc(2\pi s)}{2Z_2} \\ T_{H,21} &= \frac{(Z_0-Z_1)Z_2+iZ_0Z_1 \cot(2\pi s)}{2Z_0Z_2} & T_{H,22} &= \frac{(Z_0+Z_1)Z_2+iZ_0Z_1 \cot(2\pi s)}{2Z_0Z_2} \\ T_{H,23} &= -\frac{iZ_1 \csc(2\pi s)}{2Z_2} & T_{H,24} &= -\frac{iZ_1 \csc(2\pi s)}{2Z_2} \\ T_{H,31} &= \frac{iZ_1 \csc(2\pi s)}{2Z_2} & T_{H,32} &= \frac{iZ_1 \csc(2\pi s)}{2Z_2} \\ T_{H,33} &= \frac{(Z_0+Z_1)Z_2-iZ_0Z_1 \cot(2\pi s)}{2Z_0Z_2} & T_{H,34} &= \frac{(Z_0-Z_1)Z_2-iZ_0Z_1 \cot(2\pi s)}{2Z_0Z_2} \\ T_{H,41} &= -\frac{iZ_1 \csc(2\pi s)}{2Z_2} & T_{H,42} &= -\frac{iZ_1 \csc(2\pi s)}{2Z_2} \\ T_{H,43} &= \frac{(Z_0-Z_1)Z_2+iZ_0Z_1 \cot(2\pi s)}{2Z_0Z_2} & T_{H,44} &= \frac{(Z_0+Z_1)Z_2+iZ_0Z_1 \cot(2\pi s)}{2Z_0Z_2} \end{aligned}$$

with  $s = h/\lambda$  and  $\csc(z) = 1/\sin(z)$ . Here,  $\lambda$  is the wavelength of the propagating wave. The transfer matrices for the H-sections are now used to construct the beam splitter transfer matrix. As shown in Fig. 2.17, we set  $Z_0 = \tilde{Z}_0$ ,  $Z_1 = \tilde{Z}_0/\sqrt{2}$ ,  $Z_2 = \tilde{Z}_0$ , and  $h = \lambda_{BS}/4$  for the first H-section, with  $\lambda_{BS}$  being the wavelength corresponding to the design frequency  $\omega_{BS}$ . For signals at the design frequency, we find

$$\mathcal{T}_{H,1} = \mathcal{T}_H(\omega_{BS}, \frac{\lambda_{BS}}{4}, \tilde{Z}_0, \frac{\tilde{Z}_0}{\sqrt{2}}, \tilde{Z}_0) = \begin{pmatrix} \frac{2+\sqrt{2}}{4} & \frac{2-\sqrt{2}}{4} & \frac{i\sqrt{2}}{4} & \frac{i\sqrt{2}}{4} \\ \frac{2-\sqrt{2}}{4} & \frac{2+\sqrt{2}}{4} & -\frac{i\sqrt{2}}{4} & -\frac{i\sqrt{2}}{4} \\ \frac{i\sqrt{2}}{4} & \frac{i\sqrt{2}}{4} & \frac{2+\sqrt{2}}{4} & \frac{2-\sqrt{2}}{4} \\ -\frac{i\sqrt{2}}{4} & -\frac{i\sqrt{2}}{4} & \frac{2-\sqrt{2}}{4} & \frac{2+\sqrt{2}}{4} \end{pmatrix} \quad (2.48)$$

For the right H-section (see Fig. 2.17), we set  $Z_0 = \tilde{Z}_0/\sqrt{2}$ ,  $Z_1 = \tilde{Z}_0$ ,  $Z_2 = \tilde{Z}_0$ , and  $h = \lambda_{BS}/4$ . We then find

$$\mathcal{T}_{H,2} = \mathcal{T}_H(\omega_{BS}, \frac{\lambda_{BS}}{4}, \frac{\tilde{Z}_0}{\sqrt{2}}, \tilde{Z}_0, \tilde{Z}_0) = \sqrt{2} \begin{pmatrix} \frac{2+\sqrt{2}}{4} & -\frac{2-\sqrt{2}}{4} & \frac{i\sqrt{2}}{4} & \frac{i\sqrt{2}}{4} \\ -\frac{2-\sqrt{2}}{4} & \frac{2+\sqrt{2}}{4} & -\frac{i\sqrt{2}}{4} & -\frac{i\sqrt{2}}{4} \\ \frac{i\sqrt{2}}{4} & \frac{i\sqrt{2}}{4} & \frac{2+\sqrt{2}}{4} & -\frac{2-\sqrt{2}}{4} \\ -\frac{i\sqrt{2}}{4} & -\frac{i\sqrt{2}}{4} & -\frac{2-\sqrt{2}}{4} & \frac{2+\sqrt{2}}{4} \end{pmatrix} \quad (2.49)$$

Next, we combine the transfer matrix of the first H-section  $\mathcal{T}_{H,1}(\omega, h)$  with the matrix  $\mathcal{T}_{TL}(\omega, l)$  for a piece of transmission line of length  $l$  at every output port. Finally, we add the second H-section matrix  $\mathcal{T}_{H,2}(\omega, h)$  to construct a beam splitter transfer matrix (see Fig. 2.17 to identify the circuits represented by  $\mathcal{T}_{H,1}(\omega, h)$ ,  $\mathcal{T}_{TL}(\omega, l)$ , and  $\mathcal{T}_{H,2}(\omega, h)$ ). We fix  $l$  to be a quarter of the wavelength corresponding to the design frequency  $\omega = \omega_{BS}$  of the beam splitter. In this way, we get a matrix for the beam splitter, which depends only on  $\omega$ :

$$\mathcal{T}_{BS}(\omega, h, l) = \mathcal{T}_{H,1}(\omega, h) \cdot \mathcal{T}_{TL}(\omega, l) \cdot \mathcal{T}_{H,2}(\omega, h) \quad (2.50)$$

$$\mathcal{T}_{BS}(\omega) = \mathcal{T}_{H,1}(\omega, \lambda/4) \cdot \mathcal{T}_{TL}(\omega, \lambda/4) \cdot \mathcal{T}_{H,2}(\omega, \lambda/4) \quad (2.51)$$

At the design frequency  $\omega = \omega_{\text{BS}}$ , we expect perfect amplitude splitting of the input signal ( $A_{2,3} = A_0/\sqrt{2}$ ). The transfer matrix for  $\omega = \omega_{\text{BS}}$  becomes

$$\mathcal{T}_{\text{BS}}(\omega = \omega_{\text{BS}}) = \begin{pmatrix} \frac{i}{\sqrt{2}} & 0 & -\frac{1}{\sqrt{2}} & 0 \\ 0 & -\frac{i}{\sqrt{2}} & 0 & -\frac{1}{\sqrt{2}} \\ -\frac{1}{\sqrt{2}} & 0 & \frac{i}{\sqrt{2}} & 0 \\ 0 & -\frac{1}{\sqrt{2}} & 0 & -\frac{i}{\sqrt{2}} \end{pmatrix}. \quad (2.52)$$

### Transmission spectrum

The transmission matrix at the working frequency  $\mathcal{T}_{\text{BS}}(\omega = \omega_{\text{BS}})$  shown in Eq. (2.52) is rather simple. For  $\omega \neq \omega_{\text{BS}}$ , the transmission matrix  $\mathcal{T}_{\text{BS}}(\omega)$  depends on  $\omega$ , thus the transmission spectrum is more complex there. The full transmission spectrum for typical device parameters can be seen in Fig. 2.18.

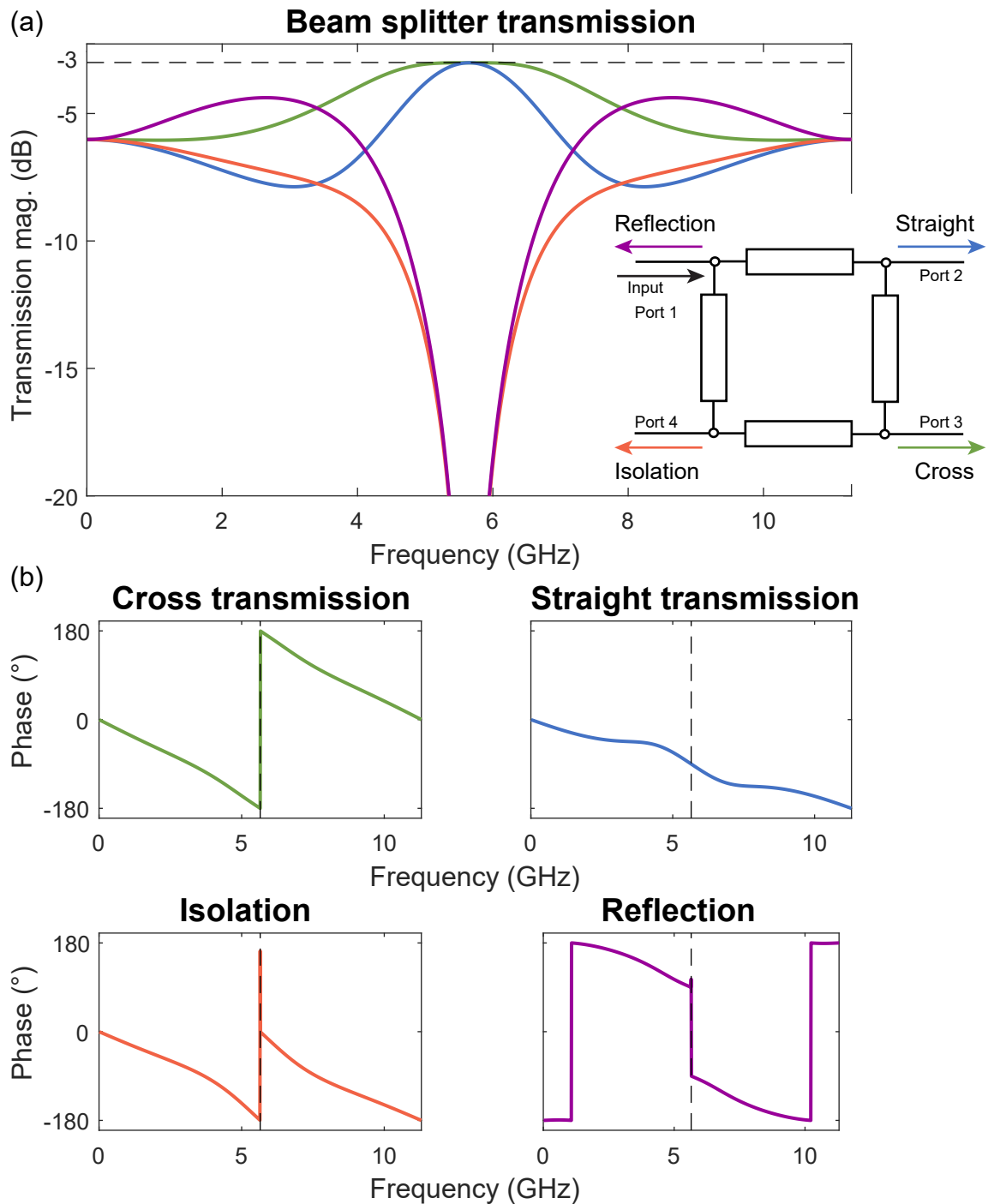


Figure 2.18: Calculated isolation, straight, and cross transmission / reflection spectrum of an ideal beam splitter (see inset) with  $\omega_{BS}/(2\pi) = 5.75$  GHz [Method equivalent to Ref. [25], using Eq. (2.51)]. (a) Magnitude (b) Phase

### 2.3.4 Mach-Zehnder interferometer

The Mach-Zehnder interferometer was brought up in 1891 [36] in the optical domain. While two half transparent mirrors are the main building block for the optical Mach-Zehnder interferometer, a microwave analog can be realized by combining two beam splitters (see Fig. 2.19). In full analogy to the optical case an object can be placed in

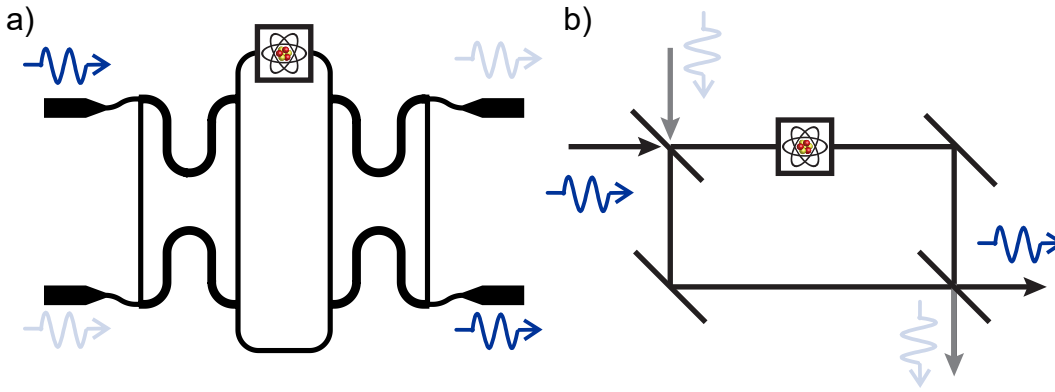


Figure 2.19: The structure presented in (a) is a microwave equivalent of a Mach-Zehnder interferometer in optics shown in (b). The scatterer (depicted as symbolic atom in a box), whose phase shift is measured, in our composite system will be replaced by a transmon qubit.

one arm of the interferometer and the phase shift resulting from the scattering of the wave at the object can be measured [see Fig. 2.19(b)]. To obtain a model of such a system, we again make use of the fact that a matrix product of transfer matrices can be used to model cascaded devices. Fig. 2.20 shows the equivalent circuit diagram of a Mach Zehnder type microwave interferometer composed of two microwave beam splitters connected by transmission lines of length  $L$ . Thus the transfer matrix for an interferometer can be constructed by combining the matrix for a beam splitter  $\mathcal{T}_{\text{BS}}$ , for two connecting transmission lines  $\mathcal{T}_{\text{TL}}$  [see Eq. (2.36)], and another beam splitter  $\mathcal{T}_{\text{BS}}$ . In the very same fashion as for Eq. (2.52), we derive:

$$\mathcal{T}_{\text{IF}}(\omega, l) = \mathcal{T}_{\text{BS}}(\omega) \cdot \mathcal{T}_{\text{TL}}(\omega, l) \cdot \mathcal{T}_{\text{BS}}(\omega) \quad (2.53)$$

$$\mathcal{T}_{\text{IF}}(\omega) = \mathcal{T}_{\text{BS}}(\omega) \cdot \mathcal{T}_{\text{TL}}(\omega, \lambda/4) \cdot \mathcal{T}_{\text{BS}}(\omega) \quad (2.54)$$

As the interferometer circuit is based on beam splitters with design frequency  $\omega_{\text{BS}}$ , it is not surprising, that it got the same design or working frequency  $\omega_{\text{IF}} = \omega_{\text{BS}}$ . For

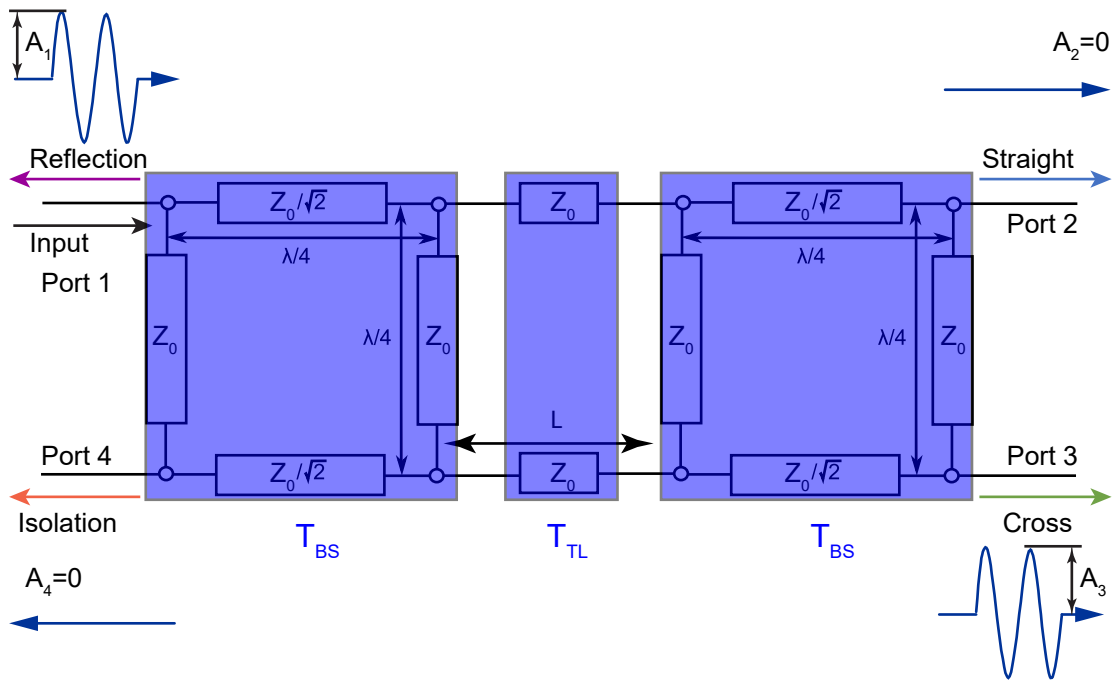


Figure 2.20: Circuit diagram of microwave interferometer (Mach-Zehnder type) with indication of transmission of an incident signal of frequency  $\omega_{\text{IF}}$  at port 1. Blue shaded areas mark parts of the circuit modeled by according transfer matrices.

$\omega = \omega_{\text{IF}}$ , we obtain

$$\mathcal{T}_{\text{IF}}(\omega = \omega_{\text{IF}}) = \begin{pmatrix} 0 & 0 & -1 & 0 \\ 0 & 0 & 0 & -1 \\ -1 & 0 & 0 & 0 \\ 0 & -1 & 0 & 0 \end{pmatrix} \quad (2.55)$$

From Eq. (2.55), we see that the output signal of an interferometer has the same amplitude as the input signal, but is phase shifted by  $180^\circ$ .

### Transmission spectrum

The transmission matrix at the working frequency  $\mathcal{T}_{\text{BS}}(\omega = \omega_0)$  shown in Eq. (2.55) is again simple. For  $\omega \neq \omega_0$ , the transmission matrix  $\mathcal{T}_{\text{IF}}(\omega)$  depends on  $\omega$ , thus the transmission spectrum is expected to be more complex there, which can be seen in Fig. 2.21.

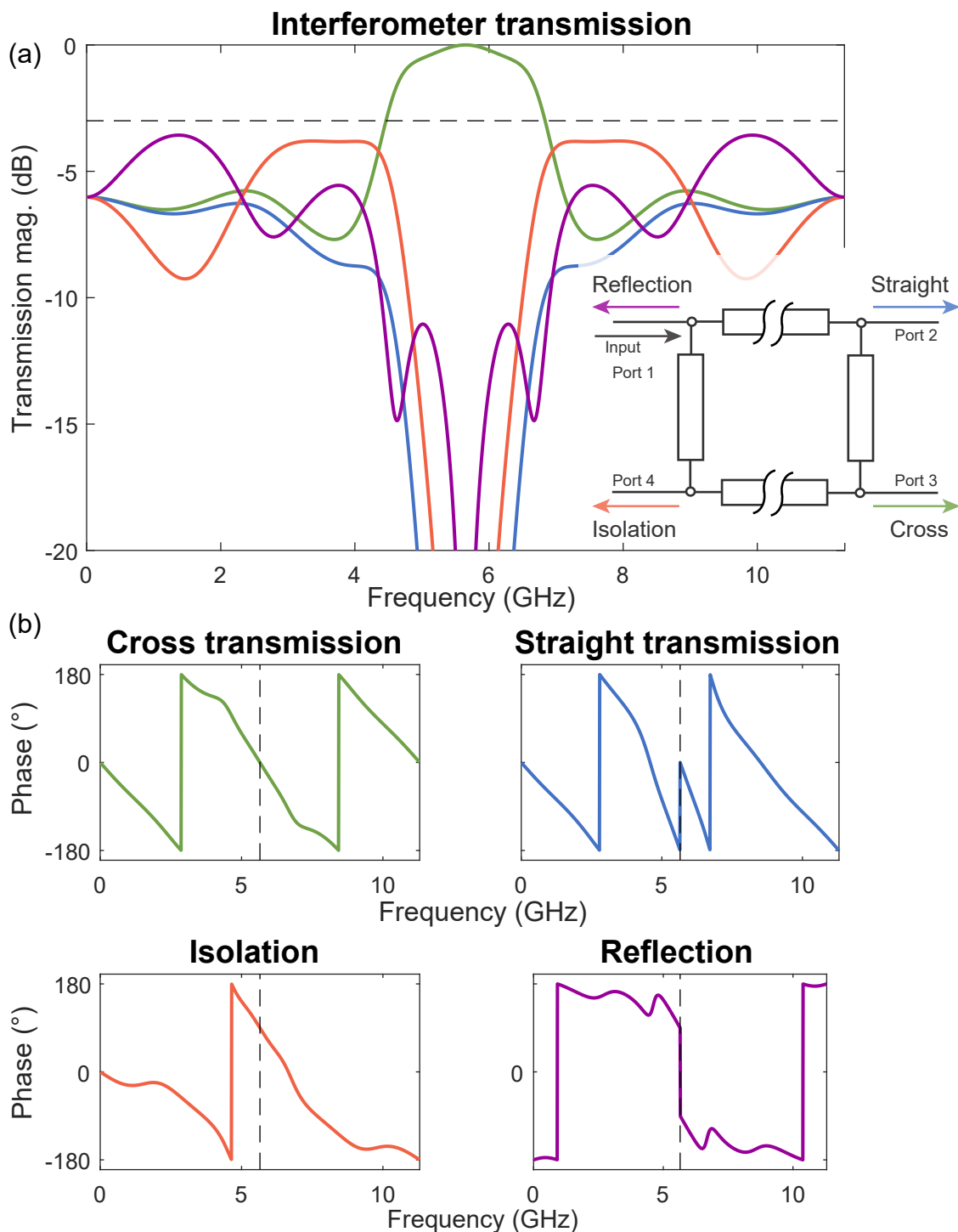


Figure 2.21: Calculated isolation, straight, and cross transmission / reflection spectrum of an ideal microwave interferometer with  $\omega_{IF} = 5.75$  GHz [Method equivalent to Ref. [25], using Eq. (2.54)]. (a) Magnitude (b) Phase

## 2.4 Superconducting quantum circuits

In this section, we present the quantum circuit theory for the transmission line and for the transmon qubit. No quantum mechanical treatment of beam splitter and interferometer is needed for the analysis done in the course of this thesis, classical transfer matrices for lossless circuits are sufficient.

To quantum mechanically analyze a circuit, we follow the procedure described in Sec. 2.2 and Refs [26, 37, 38] of constructing a Lagrangian, deriving the Hamiltonian of the system from it, and finally quantize it. For systems, where we already derived Hamiltonians based on flux  $\phi$  and charge  $Q$ , the quantization is done by a transition from descriptive variables to operators and introducing a commutation relation between them. The use of operators instead of variables is indicated in the notation by putting hats on top the variables, thus

$$Q \longrightarrow \hat{Q}, \quad \Phi \longrightarrow \hat{\Phi}. \quad (2.56)$$

In general, operators do not necessarily commute. For  $\hat{\Phi}$  and  $\hat{Q}$ , we find:

$$[\hat{Q}, \hat{\Phi}] = i\hbar. \quad (2.57)$$

where  $[x, y]$  is the commutation relation between  $x$  and  $y$ . Additionally, this leads to the Heisenberg uncertainty principle. Applied to charge and flux it reads:

$$\Delta\hat{Q}\Delta\hat{\Phi} \geq \frac{1}{2}\hbar, \quad (2.58)$$

for the standard deviation of the observables  $\Delta\hat{Q} = \sqrt{\langle\hat{Q}^2\rangle - \langle\hat{Q}\rangle^2}$  and  $\Delta\hat{\Phi} = \sqrt{\langle\hat{\Phi}^2\rangle - \langle\hat{\Phi}\rangle^2}$ .

### 2.4.1 LC-resonator

Based on the derivation of the classical Hamiltonian, for the lumped element LC-resonator we find the quantum mechanical Hamiltonian to be:

$$\hat{H}_{\text{LC-res}} = \frac{\hat{Q}^2}{2C_r} + \frac{\hat{\Phi}^2}{2L_r}. \quad (2.59)$$

## Creation and annihilation operators

We now look at the formal analogy between the Hamiltonian of a LC-resonator circuit and the motion of a particle in a harmonic potential. We conclude that we can use creation and annihilation operators to climb and descend on a ladder of energy levels in our circuit. Comparing the Hamiltonians of the two problems reveals their formal analogy [38]:

	LC- resonator circuit	Particle in harmonic potential
Hamiltonian	$\hat{H} = \frac{1}{2C}\hat{Q}^2 + \frac{1}{2L}\hat{\Phi}^2$	$\hat{H} = \frac{1}{2m}\hat{p}^2 + \frac{m\omega^2}{2}\hat{x}^2$
Commutation	$[\hat{\Phi}, \hat{Q}] = i\hbar$	$[\hat{x}, \hat{p}] = i\hbar$

Table 2.1: Formal analogy between LC-resonator and particle in a harmonic potential. We can see that the structure of the terms is similar.

From that we deduce that  $C$  takes the role of the particle mass  $m$  and  $L$  plays the role of the harmonic potential:

$$C \leftrightarrow m, \quad (2.60)$$

$$\frac{1}{2L} \leftrightarrow \frac{1}{2}m\omega^2 \quad (2.61)$$

Combining these mappings, we find the fundamental frequency of the LC-resonator to be  $\omega_0 = \frac{1}{\sqrt{LC}}$ . We define:

$$\hat{\Phi} = \Phi_{\text{ZPF}} (\hat{a} + \hat{a}^\dagger), \quad (2.62)$$

$$\hat{Q} = Q_{\text{ZPF}} \frac{1}{i} (\hat{a} - \hat{a}^\dagger), \quad (2.63)$$

with zero-point fluctuation amplitudes  $\Phi_{\text{ZPF}} = \sqrt{\frac{\hbar Z}{2}}$  and  $Q_{\text{ZPF}} = \sqrt{\frac{\hbar}{2Z}}$ . Here  $Z = L/C$  is the impedance and plays the role of the wavepacket size. We use this to explicitly express the annihilation and creation operator:

$$\hat{a} = \frac{\hat{\Phi}}{2\Phi_{\text{ZPF}}} + i\frac{\hat{Q}}{2Q_{\text{ZPF}}}, \quad (2.64)$$

$$\hat{a}^\dagger = \frac{\hat{\Phi}}{2\Phi_{\text{ZPF}}} - i\frac{\hat{Q}}{2Q_{\text{ZPF}}} \quad (2.65)$$

Thus, the standard formulation of the Hamiltonian of a particle in a harmonic potential with use of creation and annihilation operators can be used:

$$\hat{H} = \hbar\omega(\hat{a}^\dagger\hat{a} + \frac{1}{2}) = \hbar\omega(\hat{n} + \frac{1}{2}), \quad (2.66)$$

We obtain a set of equidistant energy levels (see Fig. 2.22).

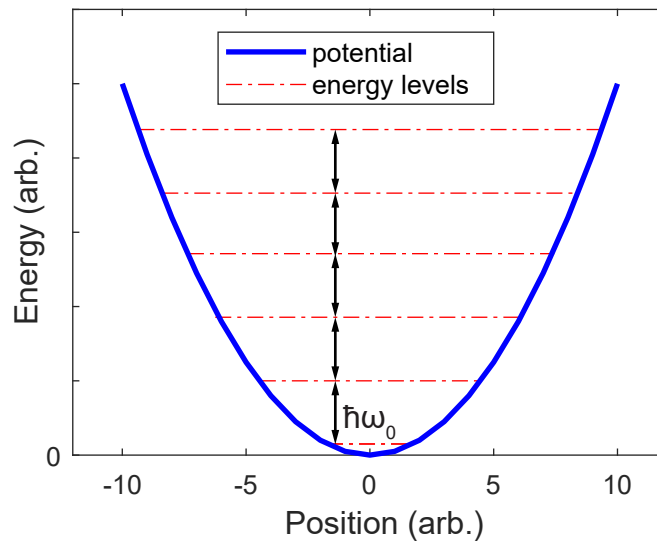


Figure 2.22: An LC resonator is analogous to a particle in a harmonic potential. Both are quantum harmonic oscillators with equidistant energy levels  $\Delta E = \hbar\omega_0$ .

### 2.4.2 Transmission line

We model the transmission line as an infinite sum of LC resonators (see App. D for details). After promoting the conjugate variables to operators, we get

$$\hat{H}_{\text{TL}} = \sum_{i=1}^N \hbar\omega_i \left( \hat{a}_i^\dagger \hat{a}_i + \frac{1}{2} \right). \quad (2.67)$$

### 2.4.3 Qubit

A quantum system with (effectively) only two energy levels is called a two level system (TLS). A TLS with sufficient level of external control implements a quantum bit (qubit) analog to classical computation, where the basic unit of information is called a binary digit (bit). A qubit is the basic unit of information in quantum information processing (QIP). The qubits quantum state is described as a superposition of its two basis states, the ground state  $|g\rangle$  and the excited state  $|e\rangle$

$$|\Psi\rangle = \alpha|g\rangle + \beta|e\rangle \quad (2.68)$$

$$= \cos\frac{\theta}{2}|g\rangle + e^{i\xi}\sin\frac{\theta}{2}|e\rangle, \quad (2.69)$$

with complex amplitudes  $\alpha = \cos(\theta/2)$ ,  $\beta = e^{i\xi}\sin(\theta/2)$ ,  $\alpha, \beta \in \mathbb{C}$ ,  $\xi \in [0, 2\pi[$ , and  $\theta \in [0, \pi]$ . Qubit states are graphically represented by a vector in the Bloch sphere (see Fig. 2.23) starting at the origin. For pure states, the amplitudes are normalized as  $\alpha^2 + \beta^2 = 1$  and the vector ends **on** the surface, for mixed states it ends inside the sphere.

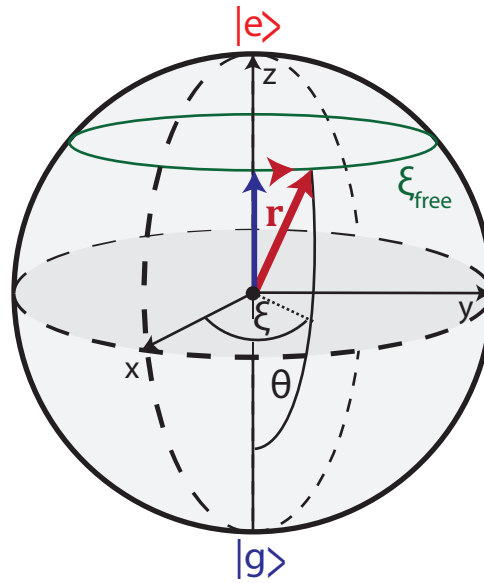


Figure 2.23: The Bloch sphere is a graphical representation of the quantum state of a qubit. The vector  $\mathbf{r} = (r \sin \theta \cos \xi, r \sin \theta \sin \xi, r \cos \theta)$  represents the qubit state  $|\psi\rangle = \cos\frac{\theta}{2}|g\rangle + e^{i\xi}\sin\frac{\theta}{2}|e\rangle$ . For free evolution in time, the state vector  $r$  precesses around the  $z$ -axis.

The state of a qubit can of course also be described by its density matrix, which

for a pure state is given as:

$$\rho = |\Psi\rangle\langle\Psi| = \begin{pmatrix} |\alpha|^2 & \alpha\beta^* \\ \alpha^*\beta & |\beta|^2 \end{pmatrix}, \quad (2.70)$$

In this matrix, the diagonal elements give information about the population of the ground and excited qubit state, while the off-diagonal elements carry information about dephasing.

### Pauli Operators

In full analogy to the ladder operators of an harmonic oscillator, we use Pauli matrices and Pauli operators to describe level transitions of a qubit:

$$\hat{\sigma}_x = \begin{pmatrix} 0 & 1 \\ 1 & 0 \end{pmatrix}, \hat{\sigma}_y = \begin{pmatrix} 0 & -i \\ i & 0 \end{pmatrix}, \hat{\sigma}_z = \begin{pmatrix} 1 & 0 \\ 0 & -1 \end{pmatrix} \quad (2.71)$$

$$\hat{\sigma}_+ = |e\rangle\langle g| = \begin{pmatrix} 0 & 0 \\ 1 & 0 \end{pmatrix}, \hat{\sigma}_- = |g\rangle\langle e| = \begin{pmatrix} 0 & 1 \\ 0 & 0 \end{pmatrix} \quad (2.72)$$

### Free evolution

The free evolution in time of  $|\Psi\rangle$  is given by the time evolution operator  $\exp(-i\hat{H}/\hbar)$ , thus its components evolve at its characteristic exponential factor due to their eigenenergy [39]. For pure superposition states this leads to precession of the state vector about the quantization axis, thus the z-axis (see Fig. 2.23).

### Driven evolution

A microwave pulse  $V_{\mu w} = A \cos(\omega_p t + \chi)$  applied to the circuit couples to  $\sigma_x$ , thus it can be used to rotate the qubit state about  $x$  or  $y$  axes, respectively, depending on the phase  $\chi$  of the applied pulse [40, 41].

### Decoherence

A pure qubit state can lose its information by either relaxing to the ground state or losing the phase information. The combination of these two processes is called decoherence. In a nutshell, the decoherence is mainly governed by environmental

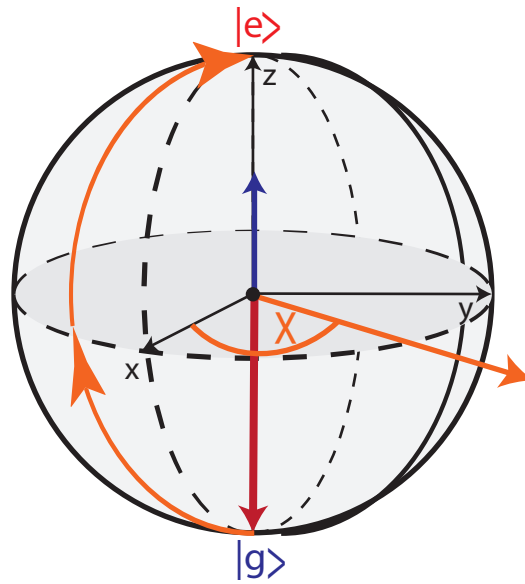


Figure 2.24: The phase  $\chi$  of the applied microwave pulse determines the axis of the rotation of the qubit state.

fluctuations at frequencies near the qubit transition frequency  $\omega = \omega_{\text{qb}}$  and at frequencies near zero  $\omega \rightarrow 0$  (see Fig. 2.37).

The transition of the qubit from  $|e\rangle$  to  $|g\rangle$  is called longitudinal relaxation with the according rate  $\Gamma_1$ . It is called longitudinal in remembrance of NMR as it is a change of the spin orientation along the z-orientation and the related state and energy change, which is per definition aligned with the strong external magnetic field there. Noise at the TLS transition frequency  $\omega \approx \omega_{\text{qb}}$  is the main source of such processes [see Fig. 2.37(b)]. It induces absorption or emission of a microwave photon. The second process is transverse relaxation (pure dephasing) at the rate  $\Gamma_\varphi$ . It gives the characteristic time scale on which the qubit will lose the information on the phase between the basis states. It is known to be mainly caused by low frequency noise ( $\omega \rightarrow 0$ )  $\ll \omega_{\text{qb}}$  [see Fig. 2.37(b)], inducing an adiabatic shift of the qubit transition frequency [42]. Together,  $\Gamma_1$  and  $\Gamma_\varphi$  define the decoherence rate<sup>3</sup>  $\Gamma_2$ :

$$\Gamma_2 = \frac{\Gamma_1}{2} + \Gamma_\varphi. \quad (2.73)$$

Summarizing, the time evolution of a qubit state is characterized by two rates, the relaxation rate  $\Gamma_1$  and the pure dephasing rate  $\Gamma_\varphi$ . These rates also define the

<sup>3</sup>in the Bloch-Redfield approach

characteristic timescales

$$T_1 = \frac{2\pi}{\Gamma_1} \dots \text{relaxation time,} \quad (2.74)$$

$$T_2 = \frac{2\pi}{\Gamma_2} \dots \text{decoherence time, and} \quad (2.75)$$

$$T_\varphi = \frac{2\pi}{\Gamma_\varphi} \dots \text{pure dephasing time.} \quad (2.76)$$

### Qubit realizations

Above, some general properties of qubits have been discussed and we have realized that potentially every TLS is a qubit. TLS are omnipresent in physical systems, but, in the following, we apply the term "qubit" solely to TLS realized in a controlled way by means of suitable superconducting circuits. Among others, there are several realizations of qubits based on the strong non-linearity introduced by Josephson junctions [19]. For the experiments conducted in this thesis, the transmon qubit, which is a special implementation in superconducting circuits, is used. It is described in the following section.

### Transmon qubit circuit

The transmon qubit design describes a non-linear electric circuit. Its quantized energy levels are not equidistant and thus can be addressed individually. We make use of this by regarding the lowest two energy levels of the transmon qubit as an artificial spin state. Starting from a Josephson junction placed in a dc SQUID circuit, we explain why we can do this.

### Josephson junction

A Josephson junction (JJ) is a trilayer of a superconductor, insulator, and superconductor, also known as SIS-structure [43] [see Fig. 2.25(a)]. We consider a lumped-element JJ and include all internal properties to material parameters. In electrical engineering, it is modeled as a capacitance in parallel to a perfect non-linear inductance, represented as a cross for the Josephson inductance  $L_J$  in parallel with a symbol representing the junction capacitance  $C_J$  [see Fig. 2.25(b)]. For this thesis we use only the description of a zero dimensional, thus pointlike JJ.

For the superconducting areas of the JJ, macroscopic wavefunctions  $\Psi_{1,2} = \sqrt{n}e^{i\theta_{1,2}}$  describe the superconducting condensate [see Fig. 2.25(a)], where  $|\Psi|^2$  is proportional to the density of Cooper pairs and  $\theta$  is the phase of the macroscopic wavefunction.

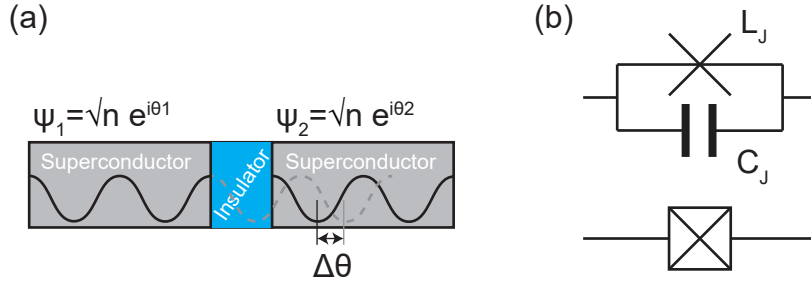


Figure 2.25: (a) A Josephson junction is a sandwich structure of two superconductors separated by a thin insulator-layer. Macroscopic wavefunctions model the superconducting areas of the junction. (b) Circuit diagram representation as inductor and capacitor (top) or as cross inside a square (bottom).

Despite an exponential decay of  $\Psi$  in the insulating barrier, for a thin enough barrier, the wavefunctions of the two superconductors overlap and allow for tunneling of Cooper pairs [depicted in Fig. 2.25(a)]. This tunneling of Cooper pairs between the two superconducting layers leads to the Josephson effect, predicted by Brian Josephsons in 1962 [44]. In Fig. 2.25(a), the light gray dashed line indicates how  $\Psi_1$  would extend, to visualize the difference of the wave function phases  $\Delta\theta = \theta_2 - \theta_1$ . We define the gauge invariant phase difference  $\varphi_{\text{SC}}$  of the macroscopic wave function across the junction [see Fig. 2.25(a)].

$$\varphi_{\text{SC}} = \Delta\theta - \frac{2\pi}{\Phi_0} \int_1^2 \mathbf{A}, \quad (2.77)$$

where  $\mathbf{A}$  is the magnetic vector potential. The integration path of  $\int_1^2$  is along the direction of current, thus across the insulating area shown in blue in Fig. 2.25(a). In the following, we will consider  $\varphi_{\text{SC}}$  as internal degree of freedom of the JJ (detailed derivation in Ref. [43]).

Then the voltage and current across a JJ is described by the first and second Josephson equation:

$$I = I_c \sin(\varphi_{\text{SC}}) \quad (2.78)$$

$$\frac{d\varphi_{\text{SC}}}{dt} = \frac{2\pi V}{\Phi_0}. \quad (2.79)$$

From Eq. (2.78) and Eq. (2.79), we see that a JJ has the same effect as a nonlinear inductance. An inductance is characterized by  $V = L\dot{I}$ . Using the chain rule on the first Josephson equation, Eq. (2.78), and combining the result with the second,

Eq. (2.79), we get:

$$V = \underbrace{\frac{\Phi_0}{2\pi I_C \cos(\varphi_{SC})}}_{L_J} \dot{I} = L_J \dot{I}. \quad (2.80)$$

Here,

$$L_J = \frac{\Phi_0}{2\pi I_C \cos(\varphi_{SC})} \quad (2.81)$$

is the Josephson inductance, which depends on cosine of the gauge invariant phase difference  $\varphi_{SC}$ . This cosine shaped dependency is at the heart of the nonlinearity for this circuit element.

A JJ has two relevant energy scales,  $E_C$  and  $E_J$ . The charging energy  $E_C$  is the energy needed to store one elementary charge in the capacitance of the junction:

$$E_C = \frac{e^2}{2C_J}, \quad (2.82)$$

where  $e$  is the elementary charge and  $C_J$  is the capacitance of the JJ.

The Josephson energy  $E_J$  is the kinetic energy of the supercurrent flowing in the Josephson inductance ( $LI^2$ ).  $E_J$  can also be interpreted as a kind of molecular binding energy comparable to a dimer, resulting from the overlap of the two macroscopic wavefunctions in superconducting electrodes of the JJ.

$$E_J = E_{J0}(1 - \cos(\varphi_{SC})), \quad (2.83)$$

where  $E_{J0} = \Phi_0 I_c / (2\pi)$  is the maximum Josephson energy determined by the critical current  $I_c$  of the junction.

### dc SQUID

A dc superconducting quantum interference device (SQUID) is a superconducting loop interrupted by two JJ [see Fig. 2.26(a)], which is very sensitive to magnetic flux. The loop has inductance  $L_{SQ}$  and the two JJs have the same critical current  $I_c$ . We assume that the flux caused by the loop inductance  $L_{SQ}$  is small compared to an applied external flux  $\Phi_{ext}$ , which is denoted by a negligible screening parameter  $\beta_L = 2I_c L_{SQ} / \Phi_0 \ll 1$  for the dc SQUID. In this situation, the Josephson energy depends directly on the external magnetic frustration  $f_{ext} = \Phi_{ext} / \Phi_0$  of the SQUID loop.

The condition  $\beta_L \ll 1$  implies that the SQUID can be considered a single JJ

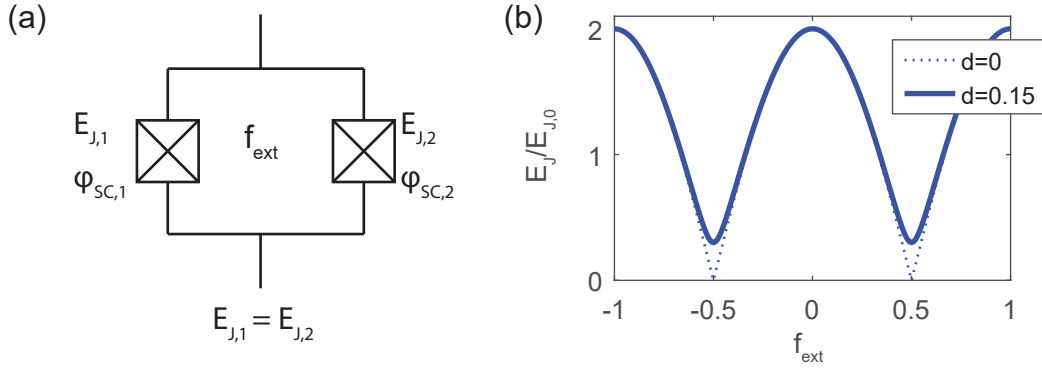


Figure 2.26: (a) An ideal dc SQUID consists of a superconducting ring interrupted by identical two JJs ( $E_{J,1} = E_{J,2}$ ). (b) The coupling energy of a dc SQUID is modulated by the external frustration  $f_{\text{ext}} = \Phi_{\text{ext}}/\Phi_0$  with asymmetry parameters  $d = 0$  and  $d = 0.15$ .

with a Josephson energy which is tunable by the external flux threading the loop. Its dependence on the external flux is given as:

$$E_{J,\text{SQ}}(f_{\text{ext}}) = 2 \frac{\Phi_0 I_c}{2\pi} |\cos(\pi f_{\text{ext}})|. \quad (2.84)$$

We see, that the Josephson energy of a dc SQUID  $E_{J,\text{SQ}}$  is related to the cosine of the external magnetic frustration  $f_{\text{ext}}$ . To be able to later on treat imperfect SQUIDs as a single Josephson junction, we define is the asymmetry parameter

$$d = \frac{E_{J,1} - E_{J,2}}{E_{J,1} + E_{J,2}}, \quad (2.85)$$

where  $E_{J,1}$  and  $E_{J,2}$  are the Josephson energies of the two Josephson junctions in the SQUID. The parameter  $d$  also appears in the flux dependent  $E_J$  of an asymmetric SQUID[40] (see Fig.2.26):

$$E_{J,\text{SQ}}(f_{\text{ext}}) = 2 \frac{\Phi_0 I_c}{2\pi} |\cos(\pi f_{\text{ext}})| \sqrt{1 + d^2 \tan^2(\pi f_{\text{ext}})}. \quad (2.86)$$

### Transmon qubit

The transmission line shunted plasma oscillation (transmon) qubit has historically developed from the charge qubit design or Cooper pair box (CPB) [45]. It consists of a dc SQUID circuit shunted by additional capacitances  $C_{\text{sh}}/2$  [45, 46] [see Fig. 2.27(a)]. Here, plasma oscillation refers to the oscillation of the superconducting phase particle in the potential of the SQUID. Due to the non-linear  $L_{\text{SQ}}$  of the SQUID, this potential is not shaped like a perfect parabola, causing a distinguish-

able energy levels. The shunt capacitances are added to the capacitance  $C_J$  of the JJ, resulting in an accumulated capacitance<sup>4</sup>

$$C_\Sigma = C_J + C_{\text{sh}}. \quad (2.87)$$

Effectively, this lowers the capacitive energy of the JJ, as due to Eq. (2.82),  $E_C \propto \frac{1}{2C_\Sigma}$ . The large effective capacity and thus low capacitive energy suppresses the sensitivity of the transmon to charge noise, but at the other hand causes a smaller difference between the energy levels.

A ratio of  $E_J/E_C \approx 50$  between Josephson and charging energy has been found to be an optimal. The Hamiltonian is constructed from capacitive and Josephson energy and reads (see App. B.2)

$$\hat{H}_{\text{TM}} = \frac{1}{2C_\Sigma} \left( \hat{Q}_a - Q_g \right)^2 - \frac{2\pi}{\Phi_0} E_{J,\text{SQ}}(f_{\text{ext}}) \cos(\hat{\varphi}_{\text{SC}}), \quad (2.88)$$

where  $E_{J,\text{SQ}}$  is the energy of the dc SQUID given by Eq. (2.84),  $C_\Sigma = C_J + C_{\text{sh}}$  is the total capacitance,  $Q_g$  is the externally induced charge,  $\hat{Q}_a$  is the operator of charge on the SC island, and  $\hat{\varphi}_{\text{SC}}$  is the phase operator. Here and in the following, we treat the dc SQUID in the transmon qubit as a single Josephson junction with flux-tunable  $E_{J,0} = E_{J,\text{SQ}}(f_{\text{ext}})$  and a single phase degree of freedom,  $\varphi_{\text{SC}}$ . This assumption is well justified because  $\beta_L \ll 1$  holds for our devices.

By applying a Taylor expansion to the cosine part of the Hamiltonian in Eq. (2.88) and neglecting terms of order higher than four, the qubit Hamiltonian can be approximated by the Hamiltonian of a nonlinear (Duffing) oscillator [47]:

$$\hat{H}_{\text{TM}} \approx \frac{1}{2} C_\Sigma \left( \frac{\Phi_0}{2\pi} \right)^2 \dot{\hat{\varphi}}_{\text{SC}}^2 + \frac{1}{2} E_{J,\text{SQ}}(f_{\text{ext}}) \hat{\varphi}_{\text{SC}}^2 - E_{J,\text{SQ}}(f_{\text{ext}}) \frac{\hat{\varphi}_{\text{SC}}^4}{24} + \mathcal{O}(\hat{\varphi}_{\text{SC}}^6). \quad (2.89)$$

In the transmon regime  $E_J/E_C > 20$ , we can deduce simple analytic expressions for the lowest transition energies. Specifically, we obtain

$$E_{01} = \hbar\omega_{\text{qb}}, \quad (2.90)$$

$$E_{12} = \hbar\omega_{\text{qb}} - E_C, \quad (2.91)$$

where  $\omega_{\text{qb}} = \omega_p = \sqrt{8E_J E_C}/\hbar$  is the plasma frequency extracted from the harmonic part of the potential [48] [see Fig. 2.27(b)]. The perturbation to the harmonic case in Eq. (2.89) gives rise to the qubit anharmonicity  $\hbar\alpha = E_{12} - E_{01} \approx -E_C$ . The energy

---

<sup>4</sup>For a transmon connected to a drive, also a coupling capacitor  $C_g$  is taken into account.

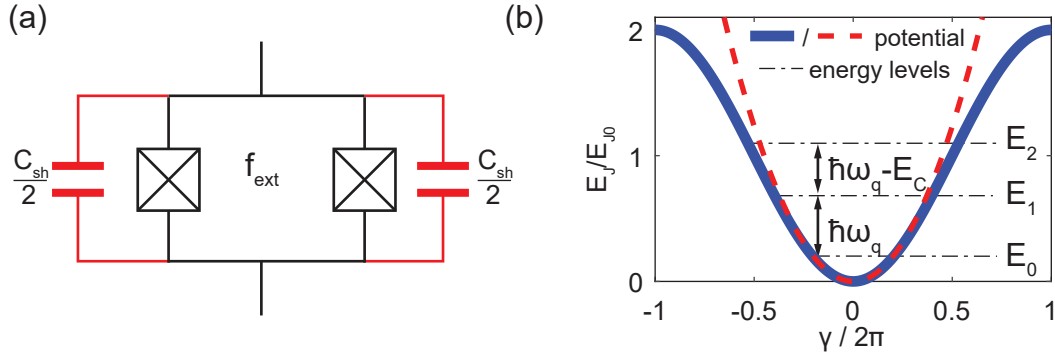


Figure 2.27: (a) Equivalent circuit of a transmon qubit. The branches marked in red are additional in comparison to a dc SQUID. (b) Potential and energy levels of a transmon. The blue line shows the transmon potential, the dashed red line a harmonic potential.

levels in the transmon potential significantly differ from the equidistant harmonic levels and thus can be addressed individually. By restricting our considerations to the first two energy levels  $E_0$  and  $E_1$ , we can regard this circuit an artificial two level system (TLS). We regard the level  $E_0$  as the ground state  $|g\rangle$  and the level  $E_1$  as the excited state  $|e\rangle$ . For a derivation of the Hamiltonian of a CPB in the laboratory frame see Appendix B. Thus, we find

$$\hat{H}_{\text{CPB/TM}} = -\frac{1}{2} (E_{\text{ch}}(n_g)\hat{\sigma}_z + E_J\hat{\sigma}_x), \quad (2.92)$$

with the Josephson energy  $E_J = E_J(f_{\text{ext}})$  depending on the external flux frustration  $f_{\text{ext}} = \Phi_{\text{ext}}/\Phi_0$  and the charging energy  $E_{\text{ch}}(n_g) = E_Q(1 - 2n_g)$ , gate charge  $n_g$  and Pauli  $\sigma$ -operators.

### Qubit-resonator coupling

In Sec. 2.4.3, we have seen that the transmon qubit has evolved from the charge qubit design. In 2004, it was shown that a Cooper pair box (CPB, the simplest charge qubit) can be strongly coupled to a microwave field on the single photon level inside a transmission line resonator [31]. The qubit acts in analogy to a natural atom in the radiation field, thus it is sometimes called an artificial atom. This situation can also be achieved with a transmon qubit [49, 50]. The equivalent circuit is shown in Fig. 2.28. The corresponding Hamiltonian is:

$$H = H_{\text{res}} + H_{\text{qb}} + H_{\text{int}}, \quad (2.93)$$

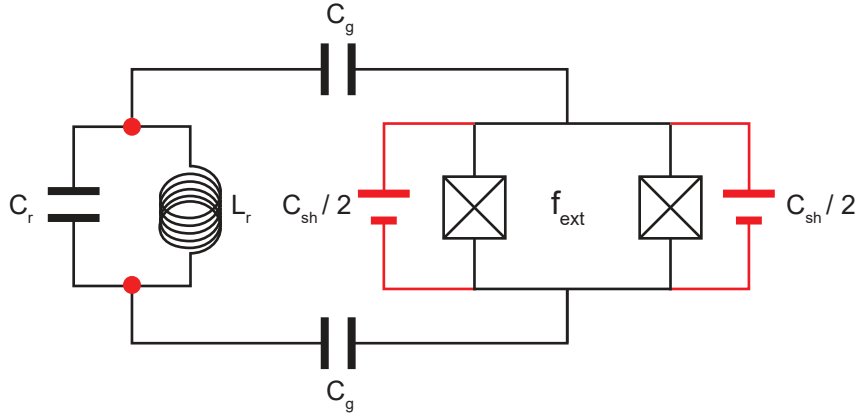


Figure 2.28: Transmon qubit coupled to a single resonator. Both entities are modeled with their equivalent circuits.

where  $H_{\text{res}}$  is the bare resonator Hamiltonian,  $H_{\text{qb}}$  is the qubit Hamiltonian and  $H_{\text{int}}$  gives the interaction terms describing how excitations are exchanged between the resonator and the qubit. From Eq. (2.59), Eq. (2.66), and Eq. (2.92) we already know the Hamiltonians for the LC-resonator  $H_{\text{res}}$  and for a qubit  $H_{\text{qb}}$ . The interaction term  $H_{\text{int}}$  describes the interaction between the resonator, or more precise the electric field  $\hat{\mathbf{E}}$  in it (a single mode field) and the qubit. Light-matter interaction is treated within the multipole expansion for electromagnetic fields [51]. Following the picture of an artificial atom, the qubit couples to the electric field via the electric dipole moment. Thus,  $\hat{H}_{\text{int}} = -\hat{\mathbf{d}} \cdot \hat{\mathbf{E}}$  is the negative product of the operators for the atomic dipole moment of the qubit  $\hat{\mathbf{d}}$  and the electric field  $\hat{\mathbf{E}}$ , where  $\hat{\mathbf{d}} \propto (\hat{\sigma}^+ + \hat{\sigma}^-)$  [40] and  $\hat{\mathbf{E}} \propto (\hat{a}^\dagger + \hat{a})$  [38]. Here,  $\hat{\sigma}^+, \hat{\sigma}^-$  are the creation and annihilation operators of the qubit and  $\hat{a}^\dagger, \hat{a}$  are the ladder operators of the resonator. Thus, we get:

$$\begin{aligned}\hat{H}_{\text{res}} &= \frac{\hat{Q}^2}{2C_r} + \frac{\hat{\Phi}^2}{2L_r} = \hbar\omega_{\text{res}}(\hat{a}^\dagger\hat{a} + \frac{1}{2}), \\ \hat{H}_{\text{qb}} &= \hbar\omega_{\text{qb}}\hat{\sigma}_z, \\ \hat{H}_{\text{int}} &= hg(\hat{\sigma}^+ + \hat{\sigma}^-)(\hat{a}^\dagger + \hat{a}),\end{aligned}$$

where the coupling constant  $g$  absorbs all proportionality constants and is a measure of how strong the light field couples to the qubit, or vice versa. Using the rotating wave approximation, we arrive at the Jaynes-Cummings model [52, 53], with

$$\hat{H}_{\text{JC}} = \underbrace{\hbar\omega_{\text{res}}(\hat{a}^\dagger\hat{a} + \frac{1}{2})}_{H_{\text{res}}} + \underbrace{\hbar\omega_{\text{qb}}\hat{\sigma}_z}_{H_{\text{qb}}} + \underbrace{hg(\hat{\sigma}^+\hat{a} + \hat{\sigma}^-\hat{a}^\dagger)}_{H_{\text{int}}} \quad (2.94)$$

The Jaynes-Cummings Hamiltonian  $\hat{H}_{\text{JC}}$  has two interesting regimes, the dispersive regime, where  $|g| < |\omega_{\text{res}} - \omega_{\text{qb}}|$ , and the resonant regime, where  $|\omega_{\text{res}} - \omega_{\text{qb}}| = 0$  (see Fig. 2.29). In the dispersive regime, energy levels of the combined qubit-resonator system are blue or red shifted due to ac Stark and Lamb shift [54]. In the resonant regime, states, with an energy degeneracy of  $\pm \hbar g \sqrt{n+1}$  are formed, where  $n$  is the number of excitations in the resonator. In the transmission spectrum

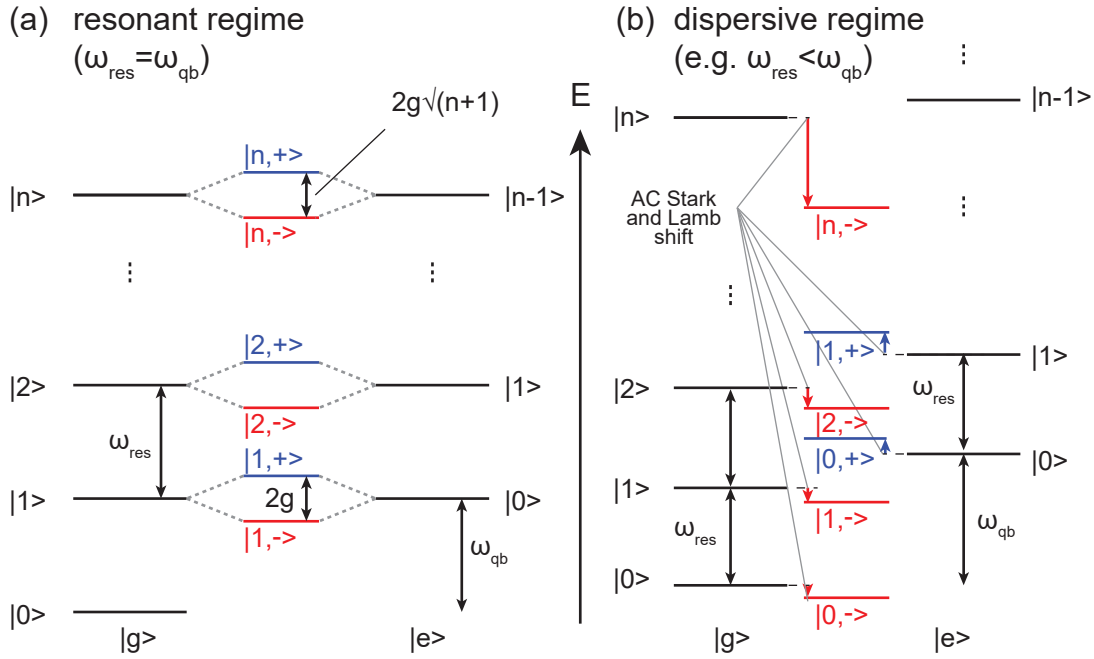


Figure 2.29: The energy levels of the JC Hamiltonian. (a) In the resonant regime, energy levels of degenerate doublets split due to the coupling  $g$ . (b) In the dispersive regime, where qubit and resonator are strongly detuned, the coupling gives rise to dressed states with ac-Stark- and Lamb-shifted energy levels.

of a qubit-resonator system with tunable qubit frequency  $\omega_{\text{qb}}$  this leads to avoided crossings, meaning that the spectral lines of the combined system repel each other where they would intersect for the noninteracting systems (see Fig. 2.30).

The resonant frequency  $\omega_{\text{QR}}$  of a qubit-resonator system can be used to extract the parameters of the underlying resonator and transmon qubit by fitting [49] the spectral data.

$$\omega_{\text{QR}} = \omega_{\text{res}} \pm \frac{1}{2} \left( \Delta(f_{\text{ext}}) + \sqrt{4g^2 + \Delta(f_{\text{ext}})^2} \right), \quad (2.95)$$

with

$$\Delta(f_{\text{ext}}) = \omega_{\text{qb}}(f_{\text{ext}}) - \omega_{\text{res}}$$

and

$$\omega_{\text{qb}}(f_{\text{ext}}) = \omega_{\text{qb, max}} \sqrt{|\cos(f_{\text{ext}})| \sqrt{1 + d^2 \tan^2(f_{\text{ext}})} - E_{\text{offset}}/\hbar}. \quad (2.96)$$

Here,  $\omega_{\text{QR}}$  is the frequency of the coupled system and  $d$  is the asymmetry parameter.

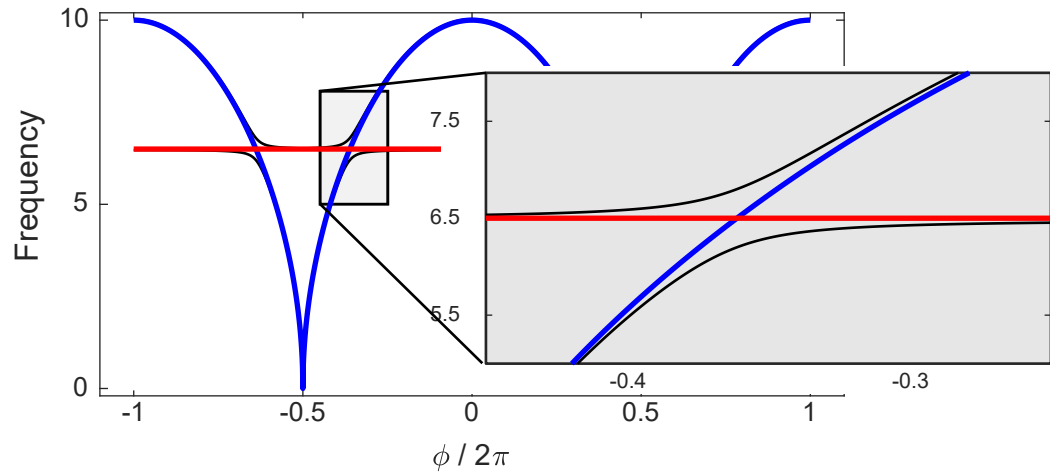


Figure 2.30: The transmission spectrum of the qubit-resonator system. Coupled system (black), noninteracting resonator (red), noninteracting qubit (blue).

### Qubit- transmission line coupling

Similarly to the way a transmon qubit couples to the single mode of a resonator, it can couple to the continuum of modes of an EM field. To model this situation, we replace one of the infinitely many LC-resonators in the model of a transmission line by a transmon qubit (see Fig. 2.31). Thus, we obtain a Hamiltonian constituted of

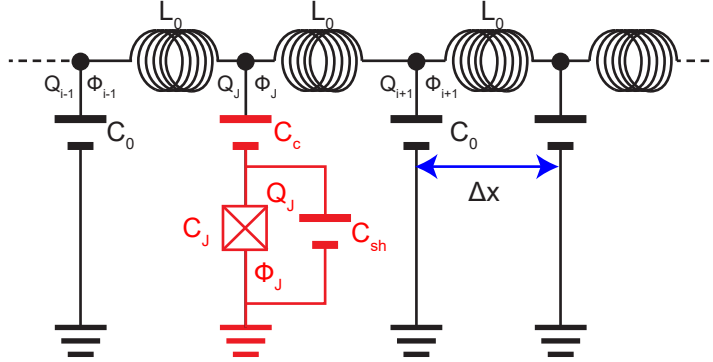


Figure 2.31: In the equivalent circuit of a transmission line, one of infinitely many LC-resonators is replaced by a transmon qubit.

three parts:

$$H = \underbrace{\sum_k \hbar\omega_k (\hat{a}_k^\dagger \hat{a}_k + \frac{1}{2})}_{H_{\text{TL}}} + \underbrace{\frac{\hbar\omega_{\text{qb}}}{2} \hat{\sigma}_z}_{H_{\text{qb}}} + \underbrace{\sum_k g_k (\hat{\sigma}^+ \hat{a}_k + \hat{\sigma}^- \hat{a}_k^\dagger)}_{H_{\text{int}}} \quad (2.97)$$

where  $H_{\text{TL}}$  is the transmission line Hamiltonian [see Eq. (2.67)],  $H_{\text{qb}}$  is the qubit Hamiltonian [see Eq. (2.88)], and  $H_{\text{int}}$  is the interaction Hamiltonian. Its structure is similar to one of Eq. (2.94), but this time the coupling of the qubit  $g_k \propto \sqrt{\omega_k}$  [38] to each modes of transmission line is considered.

This is a special case of the spin-Boson Hamiltonian. The spin-Boson Hamiltonian describes a qubit coupled to a bosonic bath and has many applications in solid-state physics and solid-state quantum information [16]. We will draw more attention on this in Sec. 2.5.1.

### Transfer matrix

To find the transfer matrix of a qubit in a transmission line, we analyze the reflection and transmission coefficients of a qubit in a transmission line. We start by an impedance analysis of a transmission line, whose characteristic impedance  $Z_{\text{eff}}$  value at a certain position is different to the rest of the line. The deviant impedance

is caused by capacitively coupling the qubit there. In this approach, we approximate the transmon qubit with an LC resonator (see Fig. 2.32). For low power, this approximation is valid, as the transmon potential still is very close to a harmonic potential for low excitation numbers [see Fig. 2.27(b)].

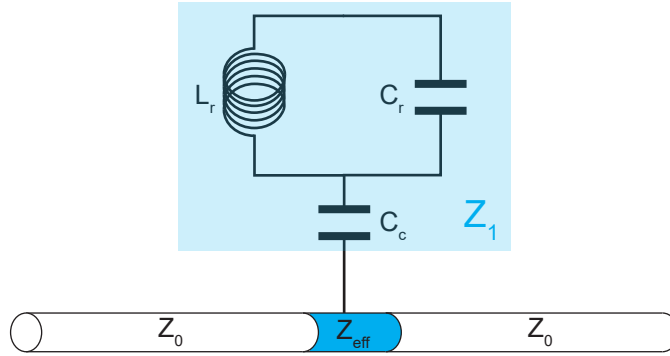


Figure 2.32: A transmission line of characteristic impedance  $Z_0$  (white), with a small piece having a different characteristic impedance  $Z_{\text{eff}}$  (dark blue), caused by an LC resonator circuit and a coupling capacitor (light blue).

At the position where the characteristic impedances changes from  $Z_0$  to  $Z_{\text{eff}}$ , a wave propagating in the transmission line is partly reflected. The ratio of the incident and reflected wave phasor is given by the reflection coefficient (see Sec. 2.1)

$$r = \frac{Z_{\text{eff}} - Z_0}{Z_{\text{eff}} + Z_0}, \quad (2.98)$$

where  $Z_0 = \sqrt{L_0/C_0}$  is the characteristic impedance of the transmission line,  $Z_{\text{eff}}$  is the impedance of the piece of transmission line which is coupled to the LC resonator. As in the actual sample, the transmon qubit is capacitively coupled to the line, a coupling capacitor is used to model the coupling of the LC resonator. Thus  $Z_1$  is the impedance of the coupling capacitor  $C_c$  in series with the LC resonator and can be obtained by simply adding the individual impedances  $Z_1 = Z_C + Z_{\text{LC}}$ , where  $Z_C = 1/(i\omega C_c)$  is the impedance of the coupling capacitor.  $Z_{\text{LC}}$  is obtained as the impedance of a capacitor and an inductor in parallel. It is given by the reciprocal sum of the reciprocals of the individual components

$$Z_{\text{LC}} = \left( \frac{1}{Z_L} + \frac{1}{Z_C} \right)^{-1}. \quad (2.99)$$

With the impedance  $Z_L = i\omega L_R$  for the inductor in the LC resonator, we obtain an effective impedance for the LC resonator and the coupling capacitor as

$$Z_1 = \frac{1}{i\omega C_c} + \left( \frac{1}{i\omega L_R} + i\omega C_R \right)^{-1}. \quad (2.100)$$

By applying the rule for the impedance of parallel components another time, the effective impedance of the line at the location of the LC resonator is obtained:

$$Z_{\text{eff}} = \frac{Z_0 Z_1}{Z_0 + Z_1} \quad (2.101)$$

Inserting Eq. (2.101) into Eq. (2.98), we obtain an exact expression for reflection coefficient

$$r = -\frac{i(-1 + \omega^2(C_c + C_R)L_R)Z_0}{i - i\omega^2(C_c + C_R)L_R + \omega C_c(-1 + \omega^2 C_R L_R)Z_0}, \quad (2.102)$$

Following Ref. [40], the above formula can be rewritten as

$$r = \frac{1 - i\Delta\omega/\Gamma_{\text{cl}}}{1 + \Delta\omega^2/\Gamma_{\text{cl}}^2}, \quad (2.103)$$

where  $\Gamma_{\text{cl}} = (\omega_0^2 C_c^2 Z_0)/(4(C_c + C_R))$ ,  $\Delta\omega = \omega_p - \omega_0$  with probe frequency  $\omega_p$  and resonance frequency  $\omega_0$  of the LC resonator [40]. This model is only valid for small powers below the one photon limit, where the harmonic potential is a good approximation for the qubit potential. A more detailed quantum mechanical analysis is given in Refs. [9, 40, 55]. They take into account relaxation rate  $\Gamma_1$ , decoherence rate  $\Gamma_2$  and drive power  $\Omega$  into the equation and find

$$r = r_0 \frac{1 - i(\Delta\omega_p/\Gamma_2)}{1 + (\Delta\omega_p/\Gamma_2)^2 + \Omega_p^2/(\Gamma_1\Gamma_2)}, \quad (2.104)$$

$$t = 1 - r, \quad (2.105)$$

where  $\Delta\omega_p = (\omega_p - \omega_{\text{qb}})$ , in full analogy to  $\Delta\omega$ , is the difference between probe frequency  $\omega_p$  and qubit transition frequency  $\omega_{\text{qb}}$ . In the limit of zero drive power,  $\Omega = 0$ , and  $r_0 = 1$ , we obtain the same result for the classical LC oscillator and the exact quantum mechanical equations within the analogy  $\Gamma_{\text{cl}} \Leftrightarrow \Gamma_2$ . We find the transfer matrix to be:

$$\mathcal{T}_{\text{QB}} = \begin{pmatrix} t - \frac{r^2}{t} & \frac{r}{t} \\ -\frac{r}{t} & \frac{1}{t} \end{pmatrix}, \quad (2.106)$$

with  $r$  defined in Eq. (2.103).

### Transmission spectrum

We use  $\mathcal{T}_{\text{QB}}$  [see Eq. (2.106)] to plot magnitude and phase of a transmon qubit in a transmission line at low drive powers. At the qubit working frequency, we expect suppressed transmission, while for reflection an increased magnitude is to be observed. This can be explained by absorption and re-emission of a photon by the qubit, which is known as resonance fluorescence [9]. Constructive and destructive interference leads to the observed increased and suppressed transmission magnitude. Taking into account that the decoherence rate  $\Gamma_2$  is composed of relaxation rate  $\Gamma_1$  and pure dephasing rate  $\Gamma_\varphi$ , it becomes apparent that one can obtain these important rates by fitting to measurement data. Figure 2.33 shows magnitude and phase of a qubit in a TL plotted from Eq. (2.104) and Eq. (2.105) for different values of  $\Gamma_1, \Gamma_\varphi$ , respectively.

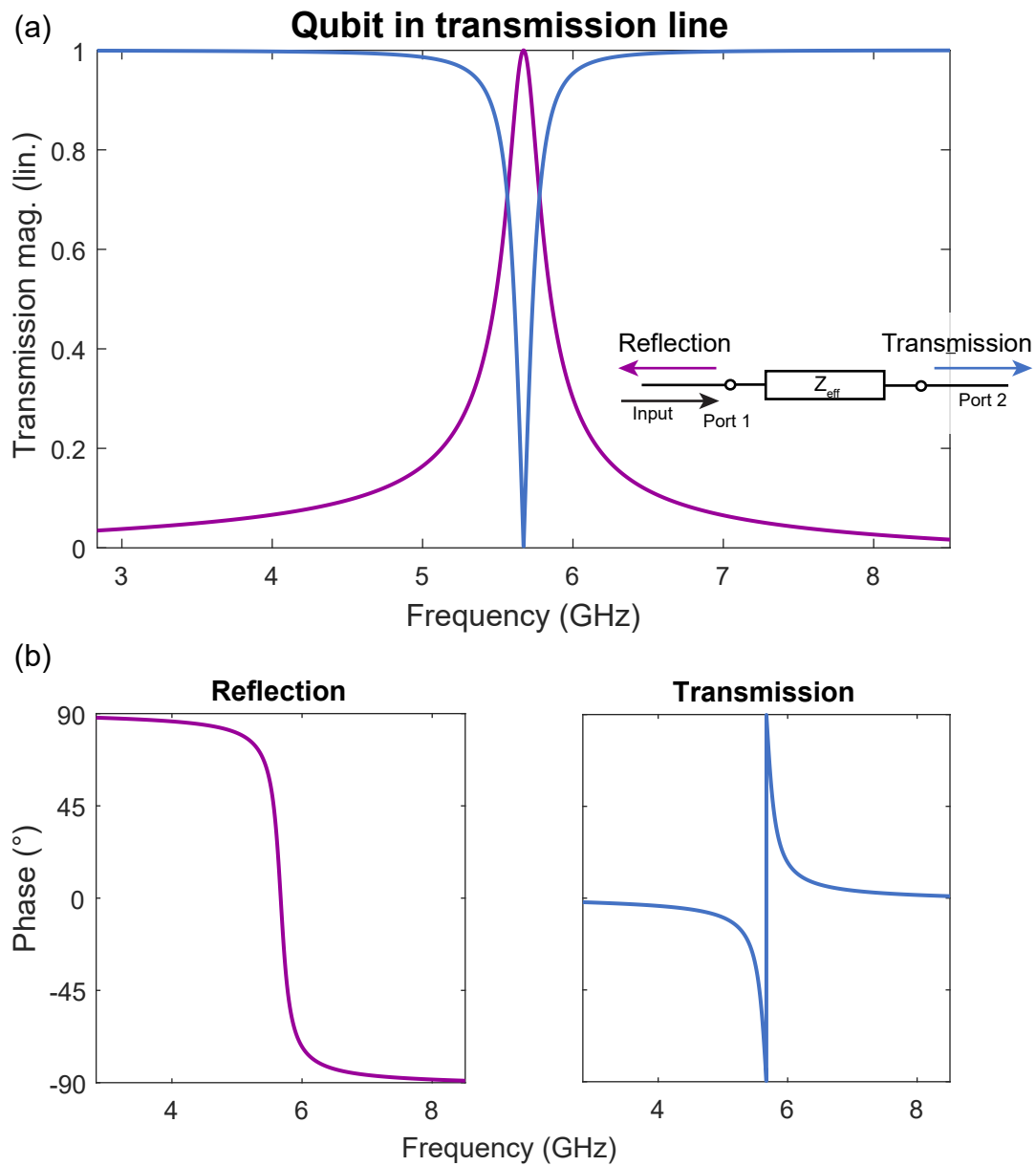


Figure 2.33: The transmission and reflection spectrum of an qubit in a transmission line in the low power limit. (a) Transmission magnitude (b) Phase.

### 2.4.4 Qubit in a microwave interferometer

In the previous sections, we have developed transmission matrices for interferometer and a transmon qubit in a transmission line. The investigations in this thesis focus on a transmon qubit in an microwave interferometer. Thus here, we derive the transfer matrix for a transmon qubit in one arm of an interferometer [see Fig. 2.34(a)]. To

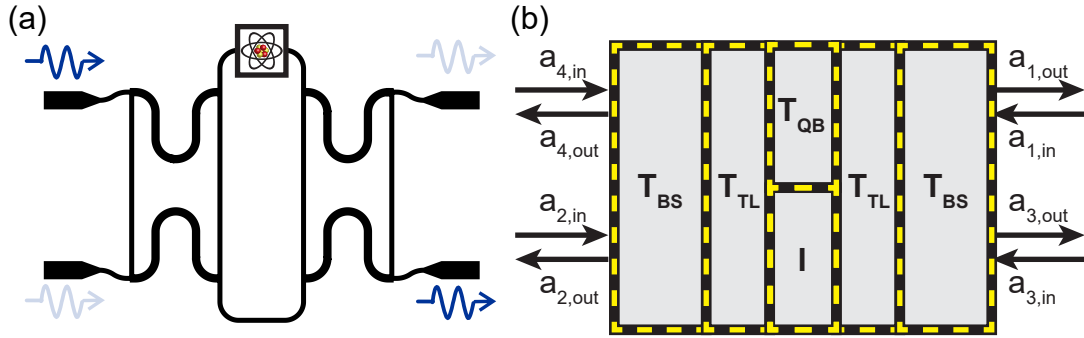


Figure 2.34: (a) A transmon qubit placed in one arm of a microwave interferometer. (b) Transfer matrix to model circuit in (a).

deduce the transfer matrix for our composite sample we combine the individual transfer matrices of beam splitter  $\mathcal{T}_{\text{BS}}$  [Eq. (2.52)], transmission line  $\mathcal{T}_{\text{TL}}$  [Eq. (2.35)] and transmon qubit in a transmission line  $\mathcal{T}_{\text{QB}}$  [Eq. (2.106)]. The scheme in Fig. 2.34 reflects that this circuit is composed of two beam splitters, connected by a bare transmission line in one arm, and by a transmission line with a transmon qubit placed in it in the other arm. The transfer matrices can be combined by simply matrix multiplication. Solely the inner parts with a negligible small piece of bare transmission line in one arm and a transmission line with a qubit inside in the other arm of the interferometer is not completely straightforward. Nevertheless it is easy to nest the  $2 \times 2$  matrix  $\mathcal{T}_{\text{QB}}$ , accounting for the qubit, and a  $2 \times 2$  identity matrix  $\mathcal{I}$ , accounting for the infinitesimal small piece of bare transmission line, in a  $4 \times 4$  matrix and multiply it on the two beam splitter and transmission line matrices  $\mathcal{T}_{\text{BS}}$  and  $\mathcal{T}_{\text{TL}}$ . Thus we find

$$\mathcal{T} = \mathcal{T}_{\text{BS}} \mathcal{T}_{\text{TL}} \left( \begin{array}{cc|cc} \mathcal{T}_{\text{QB}, 11} & \mathcal{T}_{\text{QB}, 12} & 0 & 0 \\ \mathcal{T}_{\text{QB}, 21} & \mathcal{T}_{\text{QB}, 22} & 0 & 0 \\ \hline 0 & 0 & 1 & 0 \\ 0 & 0 & 0 & 1 \end{array} \right) \mathcal{T}_{\text{TL}} \mathcal{T}_{\text{BS}}, \quad (2.107)$$

where  $\mathcal{T}_{\text{BS}}$  is the transfer matrix of a beam splitter,  $\mathcal{T}_{\text{TL}}$  is the transfer matrix of two

parallel transmission lines, and  $\mathcal{T}_{\text{QB}, ij}$  are the components of a transmission line and a qubit in transmission line transfer matrix, respectively. Figure 2.35 shows the a schematic of the sample design we use in most of our experiments and indicates the components corresponding to the matrices  $\mathcal{T}_{\text{BS}}$ ,  $\mathcal{T}_{\text{TL}}$ , and  $\mathcal{T}_{\text{QB}}$ .

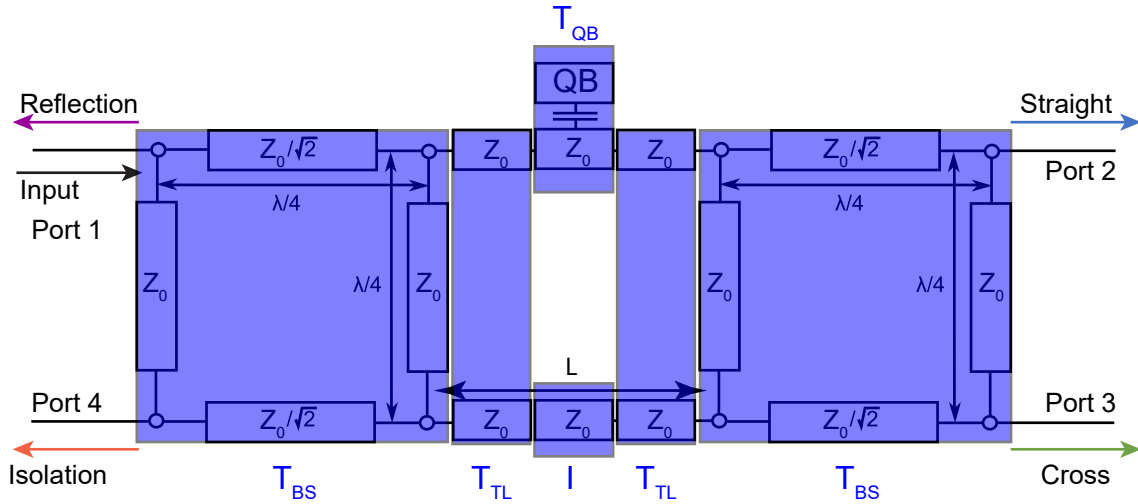


Figure 2.35: Circuit diagram of a transmon qubit placed in one arm of a microwave interferometer. The transfer matrices of the individual components are marked in blue.

## Transmission spectrum

The transmission spectrum for the composite design is mostly the same as for an interferometer, except for the region near the qubit frequency. As discussed in Sec. 2.4.3, the qubit transition frequency can be tuned by applying an external field.

## 2.5 Open quantum systems

In an open quantum system, a subsystem  $S$  of interest is coupled to another system  $B$  often called "bath" or "environment". The number of degrees of freedom of  $S$  is sufficiently small to allow for a rigorous treatment on the microscopic level. Quite on the contrary, the bath has so many degrees of freedom that its effect on  $S$  can only be evaluated by certain macroscopic parameters [see Fig. 2.36(a)]. In many scenarios, it is sufficient to evaluate the impact of these macroscopic parameters on the evolution of the subsystem  $S$ .

In open systems, the standard situation is that the action of the bath into the open system dynamics is determined by a single function, called the spectral function [Eq. (2.109)]. In more detail, the bath will perturb  $S$  with a noise whose statistical or spectral properties will be fully determined by such a function. We use this to analyze the noise properties of the interferometer (corresponding to the bath  $B$ ) in our experiments using the transmon qubit (corresponding to the system  $S$ ).

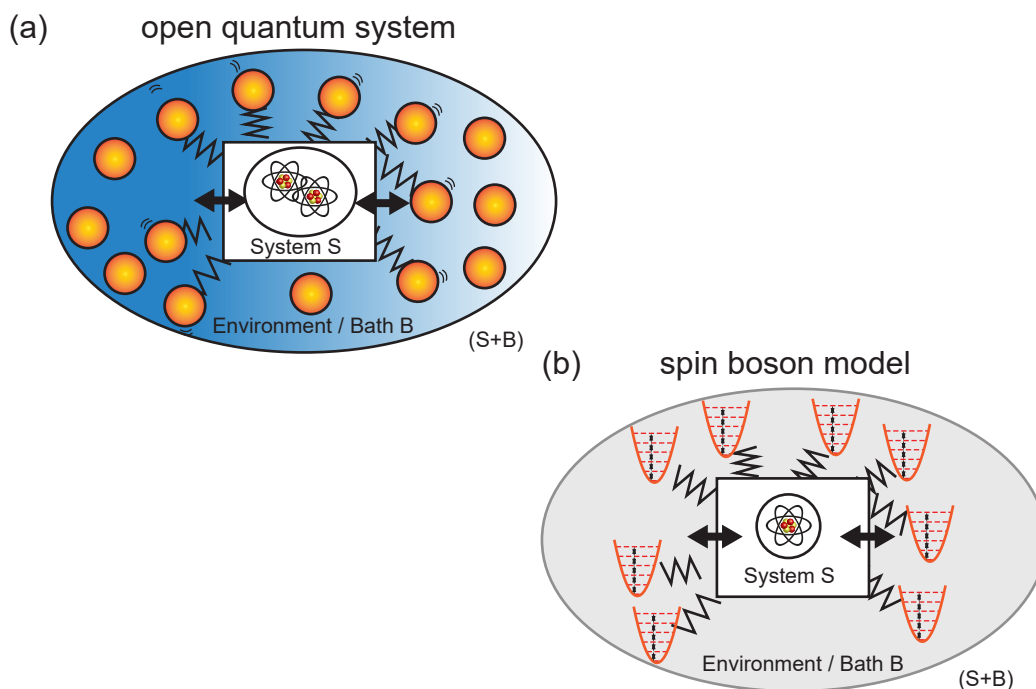


Figure 2.36: (a) Open quantum systems consider a small system  $S$  coupled to a system  $B$  with many degrees of freedom, called bath or environment. (b) The spin boson model (SBM) describes an open quantum system, where the system  $S$  is a single spin and all modes of the bath  $B$  are bosonic.

### 2.5.1 Spin-boson model

The spin-Boson model (SBM) is one of the most paradigmatic models to describe an open quantum system. Here,  $S$  is a single spin and the bath is constituted of bosonic modes. The complete Hamiltonian of the open system in this case is of the form:

$$H_{\text{SBM}} = \underbrace{\sum_k \hbar\omega_k (\hat{a}_k^\dagger \hat{a}_k + \frac{1}{2})}_{H_{\text{Bath}}} + \underbrace{\frac{\epsilon}{2} \hat{\sigma}_z + \hbar \frac{\Delta_0}{2} \hat{\sigma}_x}_{H_{\text{Spin}}} + \underbrace{\sum_k g_k \hat{\sigma}_z (\hat{a}_k + \hat{a}_k^\dagger)}_{H_{\text{Int}}} \quad (2.108)$$

where  $H_{\text{Spin}}$  is the Hamiltonian of the spin system,  $H_{\text{Bath}}$  is the bosonic bath Hamiltonian and  $H_{\text{Int}}$  describes the interaction between spin system and bath.  $H_{\text{Spin}}$  is equivalent to the Hamiltonian of a spin 1/2-particle in a magnetic field, which can be diagonalized with eigenvalues  $\pm(\epsilon^2 + (\hbar\Delta_0)^2)^{1/2}$ . [16]

The effects of the environment onto the spin dynamics (for instance its characteristic time scales) are solely encoded in the spectral function  $J$  [16, 38], where

$$J(\omega) = 2\pi \sum_k \frac{|g_k|^2}{\hbar^2} \delta(\omega - \omega_k). \quad (2.109)$$

The spectral function is a measure for the ability of the environment to emit or absorb energy of a certain frequency and thus a measure for the coupling strength at those frequencies. The properties of the SBM strongly depend on the choice of the spectral function. For many systems of interest, it takes the form

$$J(\omega) = \pi\alpha\omega^s, \quad (2.110)$$

where three further subregimes are distinguished by the exponent  $s$  of  $\omega$ . For  $s = 1$  the system is in the ohmic regime of the SBM, whereas  $s < 1$  is called subohmic and  $s > 1$  is called superohmic [16, 38].

Comparing Eq. (2.108) to Eq. (2.97), we see that the Hamiltonian for a qubit in a transmission line is a special case of the general SBM Hamiltonian with  $g_k(\omega_k) \propto \sqrt{\omega_k}$ . This dependence results in an Ohmic spectral density ( $s = 1$ ) and  $\alpha = \tilde{d}^2/(\hbar c \epsilon_0)$ , with the Planck constant  $\hbar$ , the speed of light  $c$ , the electrical vacuum permittivity  $\epsilon_0$ , and the qubit dipole moment divided by the cross-sectional area of the CPW  $\tilde{d}$  [56].

## 2.5.2 Noise and decoherence

In quantum information processing and quantum computation, the decoherence time is an important figure of merit. It gives the typical time a quantum mechanical state retains its information and thus can be used for experiments or computations. In this sense, it also tells us about the characteristic timescale on which quantum coherence is lost due to interaction with the environment. This also is at the heart of the third DiVincenzo criterion for quantum computing [57].

Here, we consider the particular scenario of an open quantum system, where the subsystem  $S$  is a single qubit. For this system we investigate decoherence properties, based on the assumption that relaxation is caused by noise at the qubit transition frequency, while pure dephasing is caused by low frequency noise (see Fig. 2.37).

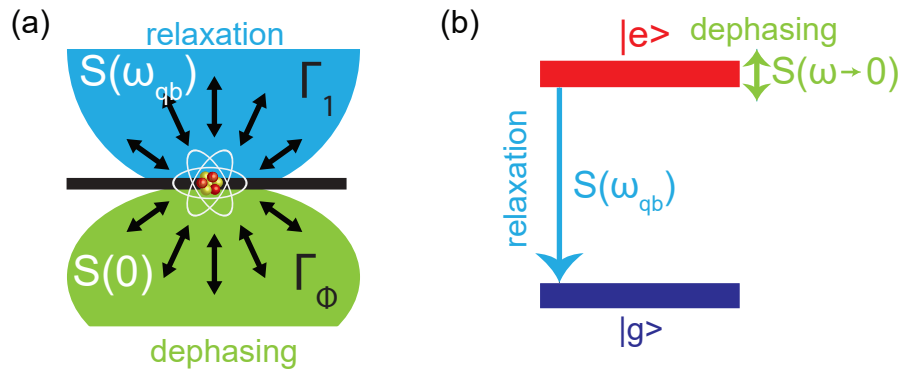


Figure 2.37: The bath drives two types of decoherence processes in the qubit. Relaxation is governed by interactions at the transition frequency of the qubit, thus  $S(\omega = \omega_{qb})$  is of special interest in this case. Dephasing is mainly caused by interactions at low frequencies,  $S(\omega \rightarrow 0)$ , which are not driving state transitions.

### Relaxation

For dissipation of energy from the system  $S$ , a qubit, we will model the bath  $B$  to be bosonic and thus use the SBM. State transitions of a qubit happen in a statistical mixture of excitation (transition from  $|g\rangle$  to  $|e\rangle$ ) at a rate  $\Gamma_{1,\uparrow}$  and relaxation (decay from  $|e\rangle$  to  $|g\rangle$ ) at a rate  $\Gamma_{1,\downarrow}$ .

$$\Gamma_1 = \Gamma_{1,\uparrow} + \Gamma_{1,\downarrow} \quad (2.111)$$

Fermi's golden rule states that the rates are  $\Gamma_{1,\uparrow} = N(\omega_{qb})J(\omega_{qb})$  and  $\Gamma_{1,\downarrow} = (1 + N(\omega_{qb}))J(\omega_{qb})$ , where  $N(\omega_{qb}) = 1/(e^{-\hbar\omega_{qb}/k_bT} - 1)$  is the Bose-Einstein distribution, which determines the number of excitations in the field exciting at the

qubit frequency. Experiments with superconducting qubits like in this thesis are conducted at millikelvin temperatures, where  $k_b T \ll \hbar \omega_{\text{qb}}$ , and therefore we can consider that  $\Gamma_{1,\uparrow} \approx 0$ , while  $\Gamma_{1,\downarrow} \approx J(\omega_{\text{qb}})$ . Using Eq. (2.111), we find

$$\Gamma_1 = \Gamma_{1,\downarrow} = J(\omega_{\text{qb}}) \quad (2.112)$$

This equation relates the spectral function at the qubit frequency to the measurable parameter  $\Gamma_1$ . In other words, the qubit probes the noise of the environment. We note that Eq. 2.112 is only valid for baths satisfying the Markovian approximation (e.g., Ohmic baths), where excitations emitted to the environment are not allowed to excite the qubit again.

## Dephasing

Dephasing is typically determined by the low-frequency properties of the bath. In practice, these are dominated by non-Markovian processes such as  $1/f$ -noise. We therefore consider the particular scenario of an open quantum system, where the subsystem  $S$  is a single qubit, while the bath  $B$  is characterized by an arbitrary spectral density. When interacting with a bath  $B$ , the qubit Hamiltonian  $\hat{H}_0$  is modified by the interaction with the bath. Thus, from the point of view of the qubit, interactions with the bath can be considered as noise. The modification of the qubit Hamiltonian caused by the bath is described with second order perturbation theory as

$$\hat{H}(\lambda + \delta\lambda) = -\frac{1}{2} \left[ \vec{H}_0(\lambda_0) + \frac{\partial \vec{H}_0}{\partial \lambda} \delta\lambda + \frac{\partial^2 \vec{H}_0}{\partial \lambda^2} \delta\lambda^2 \right] \cdot \vec{\sigma}. \quad (2.113)$$

Here, the dimensionless parameter  $\lambda$  describes the physical quantity mediating the interaction between the qubit and the bath, e.g. the normalized external magnetic flux  $\Phi_{\text{ext}}/\Phi_0$ . Thus,  $\lambda$  is called the qubit-bath coupling parameter.  $\vec{\sigma}$  is a vector of Pauli operators. The parameter  $\lambda = \lambda_0 + \delta\lambda$  can be chosen to be any physical quantity influencing the qubit transition frequency, e.g.  $\delta\lambda = \delta E_J, \delta\Phi, \delta E_C, \dots$  [41, 42, 58]. The perturbed Hamiltonian can be written as

$$\hat{H} = -\frac{1}{2} \hbar \left[ \omega_{\text{qb}} \hat{\sigma}_z + \left( D_{\lambda,z} \delta\lambda + D_{\lambda^2,z} \frac{\delta\lambda^2}{2} + \dots \right) \hat{\sigma}_z + \left( D_{\lambda,\perp} \delta\lambda + \dots \right) \hat{\sigma}_\perp \right], \quad (2.114)$$

with

$$D_{\lambda,z} \equiv \frac{\partial \omega_{\text{qb}}}{\partial \lambda}, \quad (2.115)$$

$$D_{\lambda^2,z} \equiv \frac{\partial^2 \omega_{\text{qb}}}{\partial \lambda^2} - \frac{D_{\lambda,\perp}^2}{\omega_{\text{qb}}}, \text{ and} \quad (2.116)$$

$$D_{\lambda,\perp} \equiv \frac{\partial \omega_{\perp}}{\partial \lambda}. \quad (2.117)$$

The interactions between the bath  $B$  and the system  $S$  (qubit) results in a time evolution of the qubit density matrix  $\rho$  [Eq. (2.70)], which can be written as [41]

$$\rho(t) = \begin{pmatrix} 1 + (|\alpha|^2 - 1)e^{-\Gamma_1 t} & \alpha\beta^* e^{i\Delta\omega t} e^{-\frac{\Gamma_1}{2}t} e^{-\chi(t)} \\ \alpha^* \beta e^{-i\Delta\omega t} e^{-\frac{\Gamma_1}{2}t} e^{-\chi(t)} & (|\beta|^2) e^{-\Gamma_1 t} \end{pmatrix}, \quad (2.118)$$

where  $\Delta\omega = \omega - \omega_{\text{qb}}$ ,  $e^{-\chi(t)}$  is the so-called decay function<sup>5</sup> and  $\chi(t)$  is called coherence function. For coupling to environments with an arbitrary spectrum, we expect a non-trivial decay and coherence function [42] in Eq. (2.118)

$$\chi(t) = \frac{t^2}{2} (D_{\lambda,z})^2 \int_{-\infty}^{\infty} S_{\lambda}(\omega) \text{sinc}\left(\frac{\omega t}{2}\right)^2 d\omega. \quad (2.119)$$

Here,  $S_{\lambda}(\omega)$  is the noise power spectral density, which describes the spectral behavior of environment or bath  $B$  the open system  $S$  couples to. Thus, it describes the noise seen by the system  $S$ . It is used to differentiate different types of noise. For example, white noise has a flat spectral distribution  $S_{\lambda}(\omega) = \text{const.}$ , while  $1/f$ -noise has a spectral distribution as implied by the name  $S_{\lambda}(\omega) \propto 1/\omega$  (see Fig. 2.38). The noise spectral density is given by the Fourier transform of the autocorrelation function of  $\lambda$ :

$$S_{\lambda}(\omega) = \int_{-\infty}^{\infty} d\tau \langle \lambda(\tau)\lambda(0) \rangle e^{-i\omega\tau}, \quad (2.120)$$

where  $c_{\lambda} = \langle \lambda(\tau)\lambda(0) \rangle$  is the autocorrelation function of the fluctuating parameter. Here, we consider the bath  $B$  as the only source of noise.

---

<sup>5</sup> $f_z$  in [42]

For white noise, characterized by  $S_\lambda = \text{const.}$ , in Eq. (2.120) we find

$$\chi(t) = \frac{t^2}{2} (D_{\lambda,z})^2 \int_{-\infty}^{\infty} S_\lambda(\omega) \text{sinc}\left(\frac{\omega t}{2}\right)^2 d\omega \quad (2.121)$$

$$= \frac{t^2}{2} (D_{\lambda,z})^2 \frac{\pi}{t} = t \frac{\pi}{2} (D_{\lambda,z})^2. \quad (2.122)$$

From this expression, we obtain the decay function  $e^{-\chi(t)}$  and a characteristic rate  $\Gamma_\varphi$

$$e^{-\chi(t)} = e^{-(\frac{\pi}{2}(D_{\lambda,z})^2)t} = e^{-\Gamma_\varphi t} \quad (2.123)$$

$$\Rightarrow \Gamma_\varphi = \Gamma_\varphi(\omega) \propto (D_{\lambda,z})^2. \quad (2.124)$$

For  $1/f$  noise, where  $S_\lambda = \sigma/\omega$  (with noise strength  $\sigma$ ), the same analysis according to Eq. (2.120) leads to [42]

$$e^{-\chi(t)} = e^{-(\sqrt{\sigma \ln(2)} D_{\lambda,z} t)^2} = e^{-(\Gamma_\varphi(\omega) t)^2} \quad (2.125)$$

$$\Rightarrow \Gamma_\varphi(\omega) \propto D_{\lambda,z}, \quad (2.126)$$

Next, we assume that pure dephasing is caused by flux noise, thus

$$D_{\lambda,z} = D_{\Phi,z} \propto \frac{\partial \omega_{\text{qb}}}{\partial \Phi}, \quad (2.127)$$

where  $\Phi$  is the magnetic flux threading the SQUID loop of the transmon qubit. Looking at Eq. (2.124) and Eq. (2.126), we can use the functional dependence of the pure dephasing rate  $\Gamma_\varphi = \Gamma_\varphi(\omega_{\text{qb}})$  to distinguish between white- and  $1/f$ -noise in the system [41, 42, 58].

$$\Gamma_\varphi(\omega_{\text{qb}}) \begin{cases} \propto (D_{\lambda,z})^2 \equiv \left(\frac{\partial \omega_{\text{qb}}}{\partial \Phi}\right)^2 & \text{white noise} \\ \propto D_{\lambda,z} \equiv \frac{\partial \omega_{\text{qb}}}{\partial \Phi} & 1/f \text{ noise} \end{cases} \quad (2.128)$$

Figure 2.38(a) shows a plot of  $\Gamma_\varphi(\omega_{\text{qb}})$  for white and  $1/f$ -noise, respectively. In other words, the functional dependence of  $\Gamma_\varphi(\omega_{\text{qb}})$  can be used to conclude on the spectral distribution  $S_\lambda(\omega)$  of the noise in the system.

### 2.5.3 Ornstein-Uhlenbeck model

For the low frequency regime of our experiments, we expect to find a mixture of  $1/f$  and white noise. Two level fluctuators are known to dominate this frequency

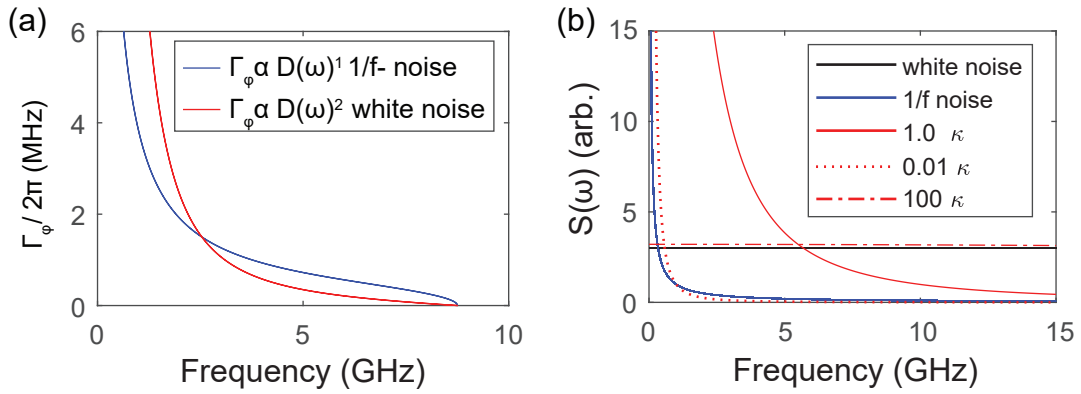


Figure 2.38: (a) Functional dependence of  $\Gamma_\varphi(\omega_{\text{qb}})$  if caused by white-, compared to  $1/f$ -noise. (b) The spectral distribution characterizes noise sources. The Ornstein-Uhlenbeck model smoothly interpolates between its limiting cases  $1/f$ , and white noise by introducing a parameter  $\kappa$  (see Sec. 2.5.3 for details).

regime and a white noise background is expected from the fact that experiments are conducted at millikelvin temperatures, which still produces nonnegligible white noise for frequencies on the order of the inverse experimental timescales.

To characterize the properties of these noise sources, we model the noise in the system via an Ornstein-Uhlenbeck process [59, 60], which allows us to smoothly interpolate between the limits of fast (white) and slow (low-frequency dominated, colored) noise. We note that the latter limit is similar, but does not exactly correspond to  $1/f$  noise. To first order, the transmon qubit transition frequency fluctuates as  $\omega_{\text{qb}}(t) = \omega_{\text{qb}} + \delta\omega_{\text{qb}}(t)$ , where the deviations  $\delta\omega_{\text{qb}}(t)$  are related to random flux fluctuations via the first derivative as,

$$\delta\omega_{\text{qb}}(t) = \frac{\partial\omega_{\text{qb}}}{\partial\Phi} \delta\Phi(t). \quad (2.129)$$

In addition, our noise model relies on a specific autocorrelation function for random flux fluctuations,

$$\langle \delta\Phi(0)\delta\Phi(\tau) \rangle = \sigma^2 e^{-\kappa|\tau|}. \quad (2.130)$$

Here,  $\sigma$  describes the flux noise amplitude and  $\kappa$  is a rate describing the temporal range of the correlations or “speed of noise”. The noise spectrum corresponding to this model is  $S(\omega) = \int e^{i\omega\tau} \langle \delta\omega_{\text{qb}}(0)\delta\omega_{\text{qb}}(\tau) \rangle d\tau$ . In the white noise limit, for  $\kappa \rightarrow \infty$ , we expect fast noise, because  $\lim_{\kappa \rightarrow \infty} S(\omega)$  becomes constant. The model smoothly connects this limit to the opposite case,  $\kappa \rightarrow 0$ , where one obtains colored quasi-static Gaussian noise, because  $\lim_{\kappa \rightarrow 0} S(\omega)$  diverges at low frequencies. This limit would correspond to a Gaussian decay envelope in a Ramsey or spin echo type

time domain experiment [42]. Figure 2.38(b) illustrates the effect of small and large  $\kappa$  on the modeled noise spectrum. Based on numerical simulations, quantitative parameters of the Ornstein-Uhlenbeck process and possible white noise background can be fitted to the data of  $\Gamma_\varphi(\omega_{\text{qb}})$  and thus be used to characterize the noise causing it.

### Full frequency noise spectrum

In the previous sections, we have investigated noise in different frequency regions. To obtain a picture of the overall noise spectrum we combine information on the

- white noise floor, which is expected to be constant at any frequencies.
- low frequencies noise spectrum from  $\Gamma_\varphi(\omega_{\text{qb}})$ ,
- high frequency noise spectrum from  $\Gamma_1$  (assumed to be ohmic in the sense of the SBM),

As mentioned earlier, the low frequency noise spectrum is described by the Ornstein-Uhlenbeck model, which assumes a bath supporting  $1/f$  noise and thus goes beyond the SBM. The high frequency contributions are assumed to be Ohmic within the SBM, thus linear in frequency.

# Chapter 3

## Experimental techniques

In this chapter, we introduce the experimental techniques and technical equipment used throughout this thesis. This includes cryogenics, fabrication, packaging, and measurement setup & devices. First, we briefly introduce cryogenics. Next, we present the fabrication of our sample chips and their design. We then explain the packaging of the samples, which ensures an environment where the environmental noise is reduced as much as possible. Finally, we describe the measurement techniques used to obtain our data.

### 3.1 Cryogenics

Most experiments presented in this work are done at cryogenic temperatures. Precharacterization measurements of PCBs, beam splitters and interferometer devices are conducted in helium bath cryostats, while experiments involving transmon qubits are performed in dilution refrigerators with base temperatures of 30 – 50 mK. Our beam splitter and interferometer structures are made of Nb with a critical temperature  $T_{c,\text{bulk}} \simeq 9.3\text{ K}$ , which easily is reached in helium bath cryostats. For circuits including transmon qubits not only the lower superconducting transition temperature of Aluminum (Al)-structures ( $T_{c,\text{bulk}} \simeq 1.2\text{ K}$ ) has to be reached, but also thermal noise from microwave lines of higher temperature stages has to be taken into account. To ensure that thermal noise is small enough to avoid noise driven state transitions of our quantum mechanical system, the circuits are measured in a dilution refrigerator. Even at absolute zero, we would need to consider vacuum fluctuations. At finite temperatures, we expect noise from black body radiation. Since, for a typical sample temperature of  $T = 50\text{ mK}$ , the corresponding frequency scale is  $k_{\text{B}}T/h \approx 1\text{ GHz}$ , the residual thermal population in the frequency range

of our measurements (4 – 8 GHz) is well below unity. Furthermore, the superconducting gap of Al protects the qubit from excitations in the continuous spectrum of the solid-state materials forming the circuits. The cryogenic temperatures are provided by home-made  $^3\text{He}/^4\text{He}$  dilution refrigerators at the WMI. In appendix A we describe the implementation of relevant cryogenic apparatuses in more detail.

## 3.2 Fabrication

The sample chips used for this thesis are fabricated in a process widely established in the field of quantum information processing with superconducting circuits[3, 31, 45, 61]. We deposit a thin film of superconducting material (either Nb or Al) on a polycrystalline Si-substrate and pattern an electrical circuit into the film via photolithography or electron-beam lithography. The more complex structures needed for the transmon qubits consist of two layers of Al.

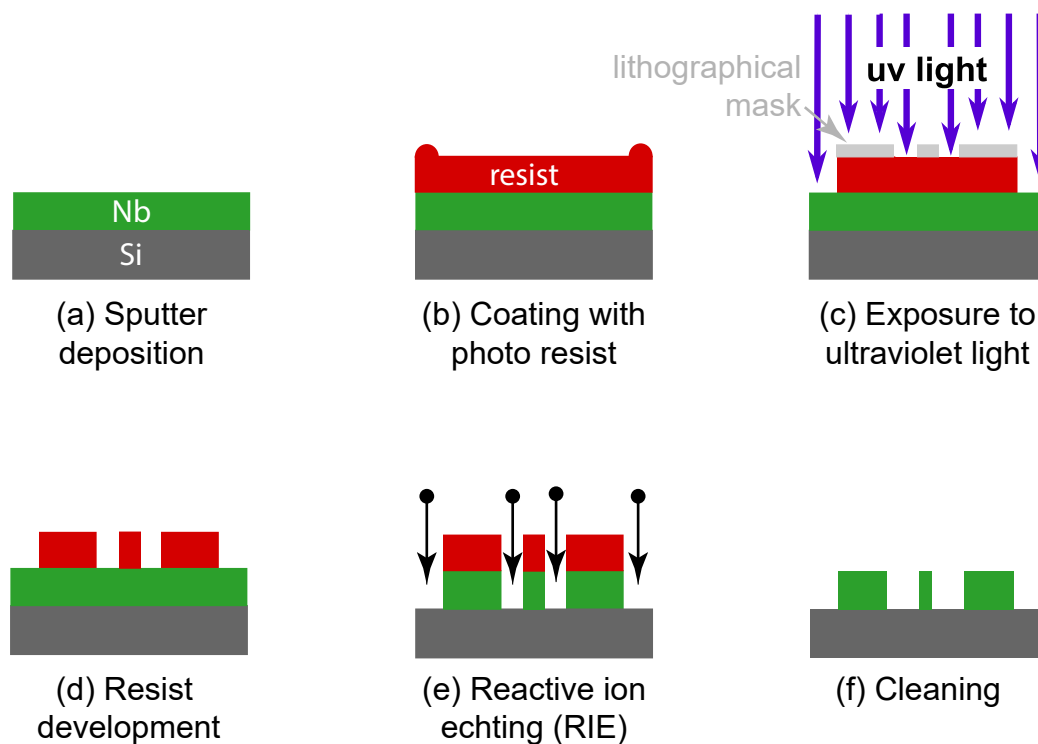


Figure 3.1: Fabrication steps for Nb structures.

### 3.2.1 Niobium structures

Beam splitters and interferometers are fabricated from niobium (Nb). Nb has a critical temperature  $T_{c,\text{bulk}} \simeq 9.3 \text{ K}$ , the fabrication of Nb-structures is well established at WMI and the patterning can be done fast and easily by optical lithography. To this end, first, a 100 nm thin film of polycrystalline Nb is sputter-deposited on a  $525 \mu\text{m}$  thick silicon substrate (insulating at low temperatures), covered with approximately 50 nm of thermal insulating oxide [see Fig. 3.1(a)]. In order to pattern the necessary structures for the CPWs into this film, we use optical lithography. We then cover the Nb-film with AZ 5214 E photo-resist [Fig. 3.1(b)] and exposure it by ultraviolet (UV)-light through a lithographic contact-mask of chrome coated glass [Fig. 3.1(c)] using a mask aligner (Carl Süss MJB 3). Developing the resist with AZ 726 MIF photo developer removes the resist from the areas which were exposed to the UV light [Fig. 3.1(d)]. Finally, by the Nb film not covered with resist is etched away by reactive ion etching (RIE)[62, 63] using a process gas [Fig. 3.1(e)]. After a cleaning protocol using acetone and isopropanol in an ultrasonic bath, and thus removing the remaining resist, we obtain the desired structure in the Nb-film on the Si substrate [Fig. 3.1(f)]. As the metal film finally residing on the substrate is inverted compared to the mask, this is called a negative process.

### 3.2.2 Aluminum structures

Structures which incorporate JJ are made of Al at WMI based on electron beam lithography and a two-angle shadow evaporation procedure[41, 61, 63, 64]. To this end, a substrate is covered with a suitable two-layer e-beam resist, which is exposed by e-beam lithography (EBL) in the areas which finally shall be covered by an Al film. After this, the resist is developed in a temperature controlled process (see [51] for a detailed description). Now, the sample is cleaned using the standard cleaning process described before (using acetone followed by isopropanol in an ultrasonic bath), which results in the non-activated resist sticking to the substrate and the rest being removed. In this way, we obtain a patterned resist film on the substrate representing the inverted circuit structure. After depositing Al, the circuit structure is patterned on the chip. Al which has been deposited onto the resist is removed during the cleaning procedure (lift-off). As we exposure the e-beam resist in those areas we finally want to be metalized, this is called a positive process.

The Al-AlO<sub>x</sub>-Al sandwich structure forming the JJ, is fabricated by facilitating resist bridges and double-angle shadow evaporation. To this end, the substrate

is coated by two layers of photo resist with different sensitivity (lower layer with high sensitivity: PMM/MA 33%, upper layer with low sensitivity: PMMA 950K). Exposing this system to electron beam doses suited to develop specific regions on the chip allows one to pattern openings, bridges and undercut structures into the resist. After resist development, Al is evaporated on the substrate under two different angles (in the shadow of the resist bridge). This step is called double-angle shadow evaporation (see Fig. 3.2).

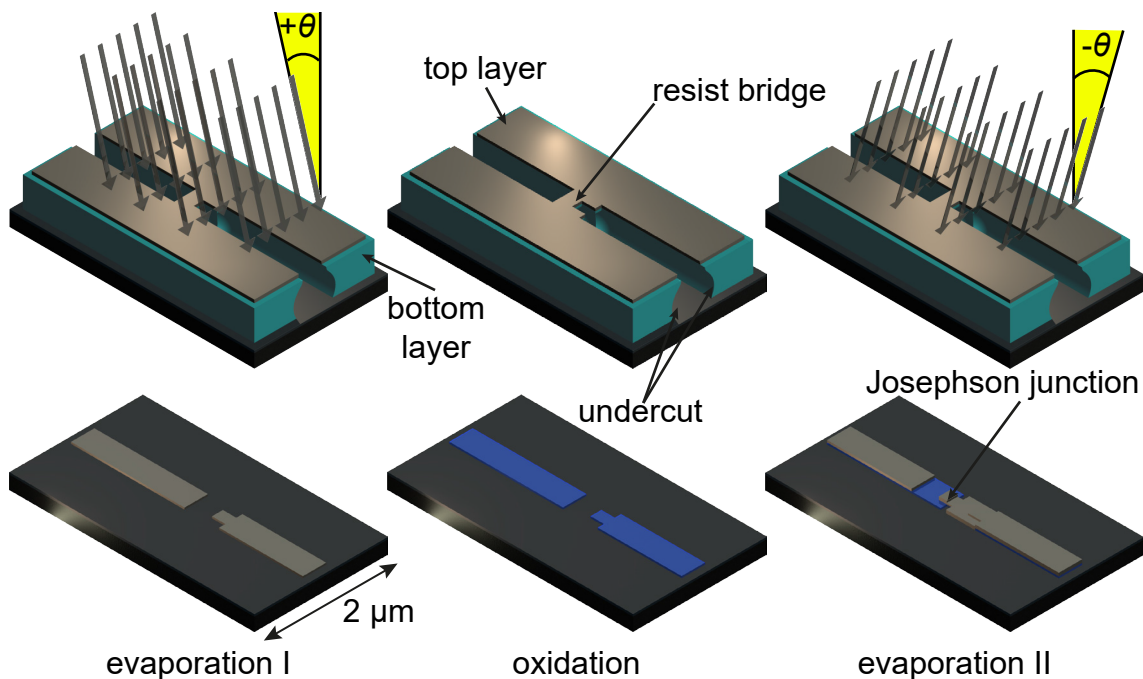


Figure 3.2: Double-angle shadow evaporation process to make nanoscale Josephson junctions. Process steps are shown from left to right. Top: Resist system, Bottom: Material layers on the substrate (Figure used with kind permission of Jan Goetz).

### 3.2.3 Designs

Here, we present the designs for the samples used in the experiments in this thesis. We start with the microwave beam splitter and the microwave Mach-Zehnder type interferometer.

#### Beam splitter

A microwave beam splitter (see Sec. 2.3.3) is a four port device composed of CPWs with different characteristic impedance and four T-junctions. The characteristic impedance of the lines is adjusted by having different ratios between width of center

conductor and gap of the CPW, respectively, while the T-junction provides two propagation paths for the signal [see Figs. 3.3(a,c,d)]. This design has the disadvan-

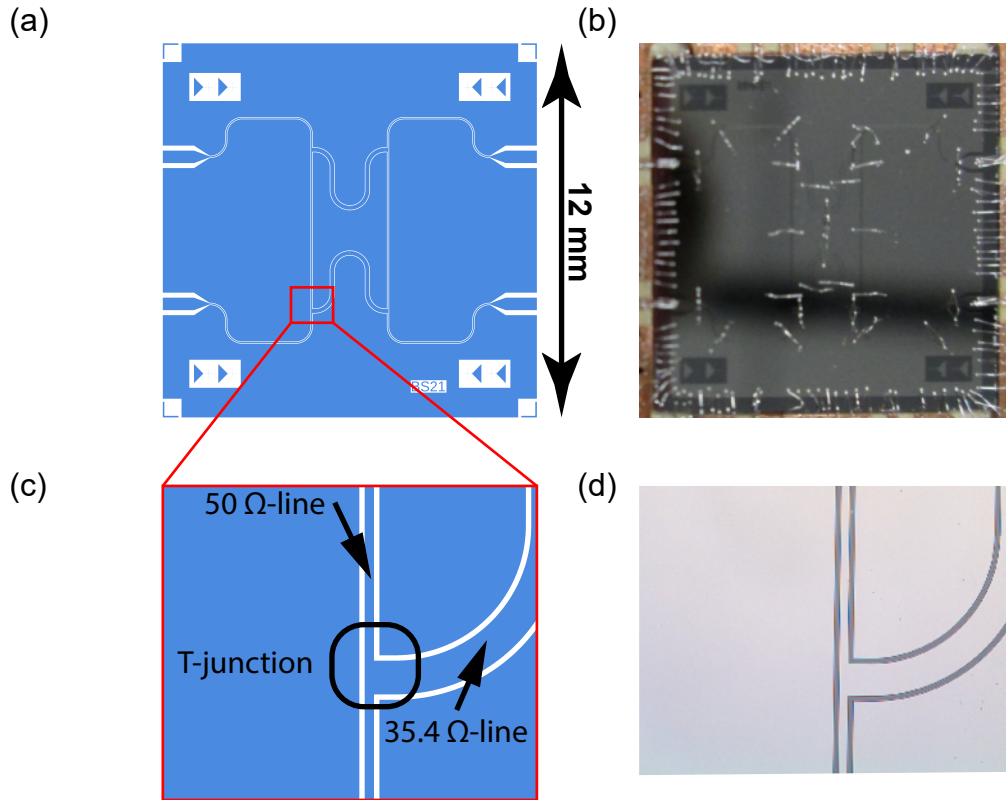


Figure 3.3: Quadrature hybrid design: (a) Design of whole chip, (blue...Nb structures, white...substrate), (b) Photograph of the sample chip, (c) Detail with T-junction and CPWs of  $50\ \Omega$  and  $35.4\ \Omega$  characteristic impedance, respectively. (d) Optical micrograph of same detail as in (c).

tage to divide the ground plane of sample into two galvanically unconnected entities. We use wire bonds to ensure that all ground plane parts are on the same electrical potential [Fig. 3.3(b)].

property	$50\ \Omega$	$36.4\ \Omega$
inner conductor width	$34.4\ \mu\text{m}$	$125.2\ \mu\text{m}$
gap width	$20\ \mu\text{m}$	
Nb thickness	100 nm	
Si substrate thickness	$525\ \mu\text{m}$	

Table 3.1: CPW design parameters of beam splitter lines with an impedance of  $50\ \Omega$  and  $36.4\ \Omega$

### Interferometer

In complete analogy to a Mach-Zehnder interferometer in the optical domain, we construct our microwave interferometer by using two beam splitters (BS) in series [Fig. 3.4(a)]. Fig. 3.4(b) shows a photograph of the chip. At its working frequency, the first BS splits the signal into two waves of equal amplitude with  $90^\circ$  phase shift, while the second BS recombines it. Any phase difference gained by the split signals will cause imperfect recombination and thus manifest in interference effects.

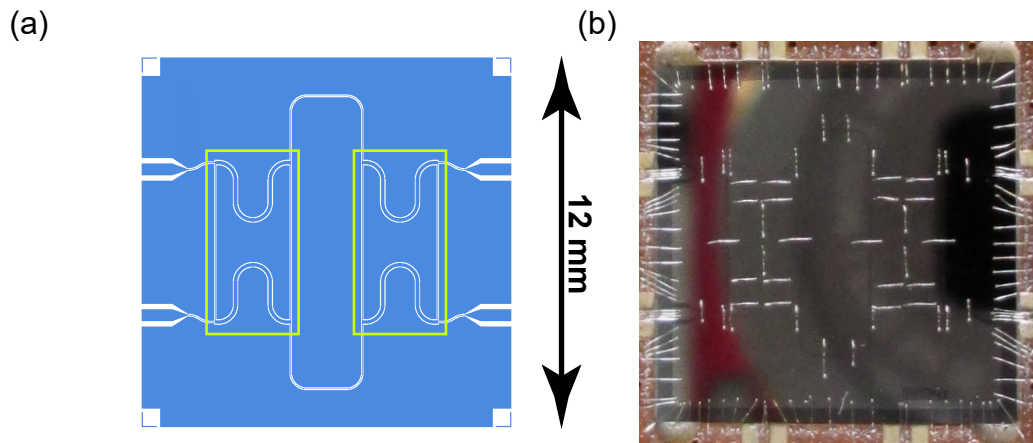


Figure 3.4: Interferometer: (a) In the design (blue...Nb structures, white...substrate) it is clearly recognizable that the interferometer is composed of two beam splitters (yellow rectangles), (b) On the sample picture we see that again on-chip wire bonds are used to ensure a good electrical connection between all parts of the ground plane.

### Transmon qubit in $\lambda/4$ -resonator

In order to check the functionality of our qubit design, we put a transmon qubit in a  $\lambda/4$  resonator. The design of the sample chip is shown in Fig. 3.5. Here, two qubit-resonator systems have been put on one  $12\text{ mm} \times 12\text{ mm}$  chip, which is cut into two pieces for conducting measurements. The experiments for this precharacterization were done in course of a Master's thesis [49]. Since the geometries of qubit and CPW are the same as for the interferometer studied later, we expect similar coupling in both devices.

The transmon itself constitutes of a small SQUID loop shunted by a large capacitance formed by two finger capacitors. The SQUID loop, as well as the finger capacitors, can be seen in Fig. 3.5(b). The position of one Josephson junction of the SQUID is marked by a red rectangle, also in Fig. 3.5(b).

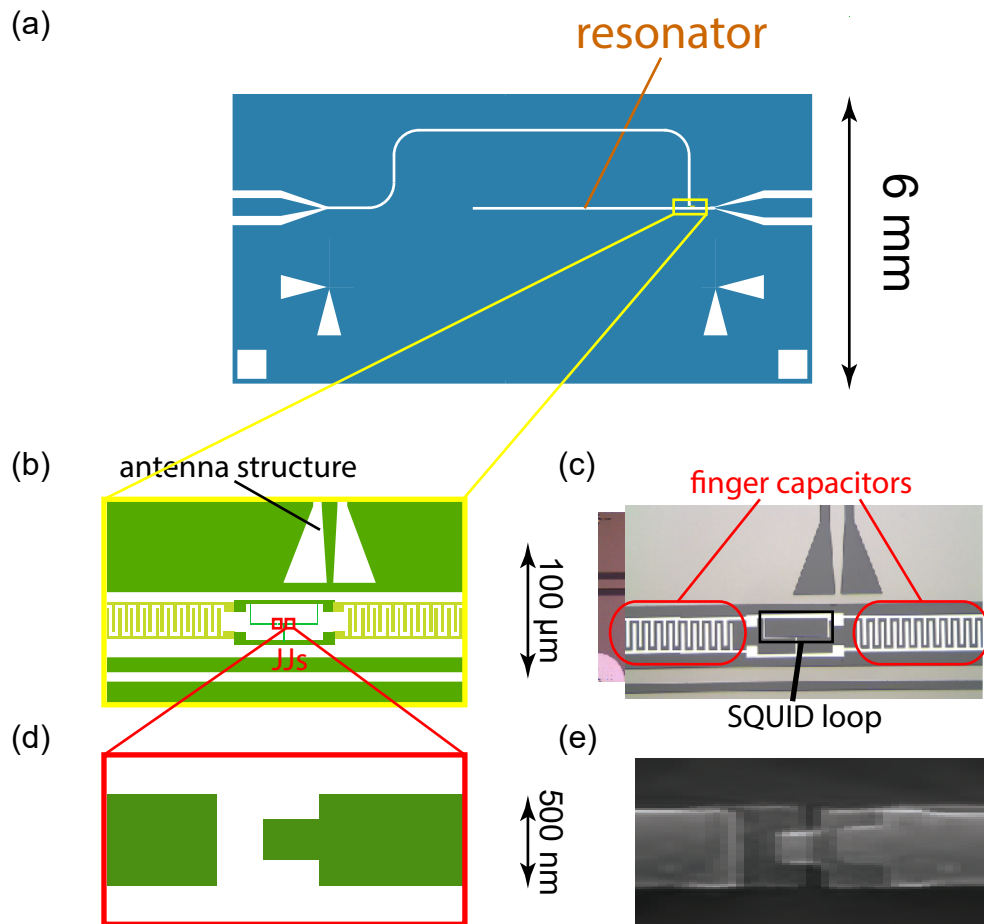


Figure 3.5: Transmon qubit in  $\lambda/4$  resonator: (a) Chip design (blue...Nb structures, green...Al structures, white...substrate). The yellow rectangle marks the position of the transmon qubit. (b) Zoom onto the transmon circuit (green...Al structures, white...substrate). Red rectangles mark the position of Josephson junctions (c) Micrograph of transmon qubit. Black: SQUID loop. Red: Finger capacitors of the transmon structure, (d) Mask layout of a Josephson junction. (e) SEM image of a Josephson junction.

### Transmon qubit in interferometer

The most important sample design is the interferometer with a transmon qubit in its bottom arm. Fig. 3.6(a) shows the design, which at first sight looks alike the interferometer design shown in Fig. 3.4. The magnified view in Fig. 3.6(c) reveals

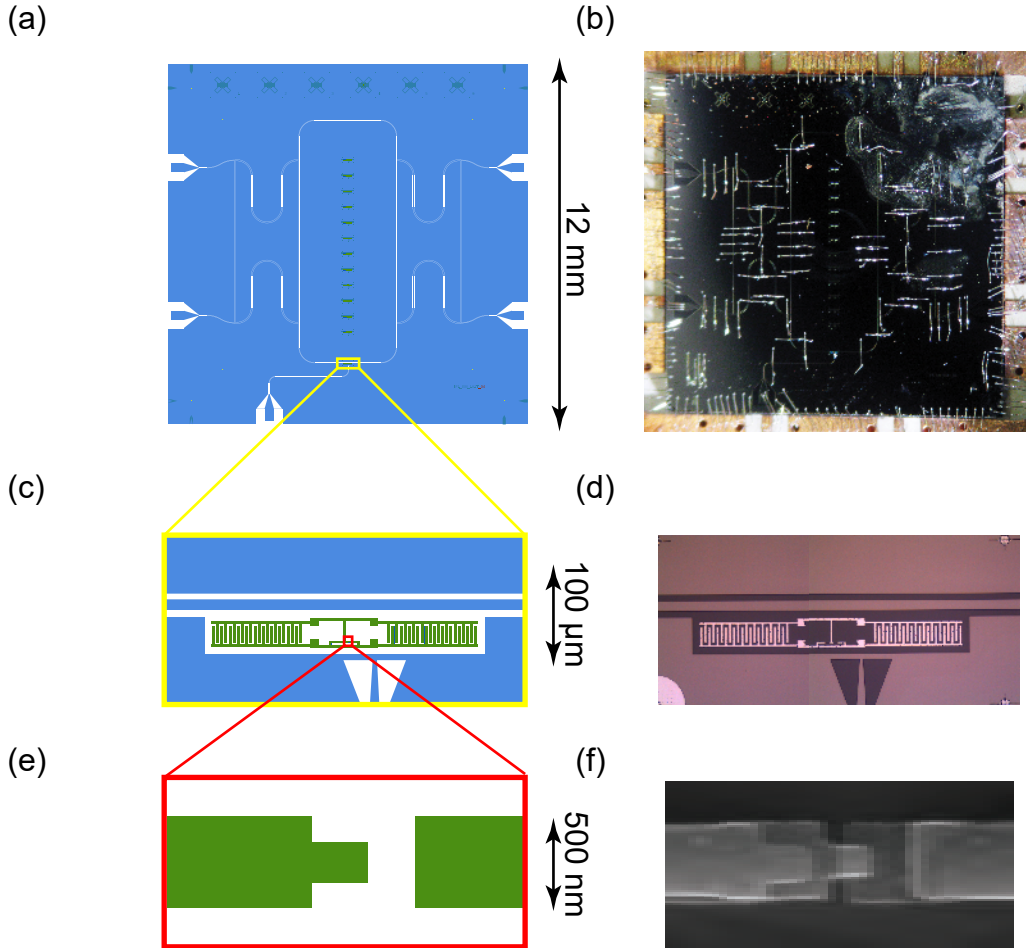


Figure 3.6: Transmon qubit in interferometer. Left: (a/c/e) Design and details (designs: blue...Nb structures, green...Al structures, white...substrate), Right: (b/d/f) Photographs of sample chip, micrograph of transmon qubit and SEM image of a Josephson junction. Left and Right are to the same scale.

the transmon structure placed in one of the interferometer arms. Figures 3.6(b),(d), and (f) show photo- and micrographs and SEM-pictures of the sample. Comparing the design of the bare interferometer in Fig. 3.4 and the design of the interferometer with a transmon qubit in the bottom arm in Fig. 3.6, it is evident that these designs use the same parameters for the CPWs, which is indeed the case. For this reason we expect these samples to have very similar measured spectra, except around the working frequency of the transmon qubit. Wire bonds were used to assure the equal

---

electrical potential at the ground planes (Fig. 3.6).

### 3.3 Measurement setup

To perform circuit QED experiments, we have to take an elaborate technological effort in terms of cooling, shielding, control, and measurement. A schematic view next to a photograph of the setup mainly used in this thesis is shown in Fig. 3.7

**Packaging, housing, shielding**— The sample chip is mounted in a specially tailored sample box and additionally shielded from parasitic magnetic fields for the experiments (see Sec. 3.3.1).

**Control**— A source-meter (Keithley 2450) provides a current-source working with high accuracy even at the required low currents in the range of micro-amperes. We feed it through a superconducting coil with approx 8000 windings to generate a magnetic field in the SQUID loop of the transmon qubit. In this way, we tune the transmon qubit to different working frequencies. Current source and coil are connected by superconducting twisted-pair wires passing through a room-temperature low-pass filter (see Fig. 3.7). The coil is mounted at the sample stage and thus also is cooled to Millikelvin temperatures.

**Sensing**— A Rohde & Schwarz ZVA24 four-port vector network analyzer (VNA) connects two heavily attenuated and filtered microwave lines to the input ports of the sample. Two lines are used to guide the filtered output signals back to the remaining ports of the VNA after amplification by a cryogenic HEMT amplifier and a room-temperature amplifier (see Fig. 3.7). The attenuation of the input lines prevents thermal noise of high-temperature stages from disturbing the sample. Experiments are done with a signal power of  $P = -140$  dBm at the transmon qubit, half populating the first qubit transition. These low powers are realized by further attenuating the signal at the VNA output ( $P = -33$  dBm) with attenuators (87 dBm), cabling (17 dBm), and the on-chip beam splitter (3 dBm) inside the cryostat. Spectroscopic measurements with this setup are at the heart of the data acquisition for this theses and are described in detail in Sec. 3.4.

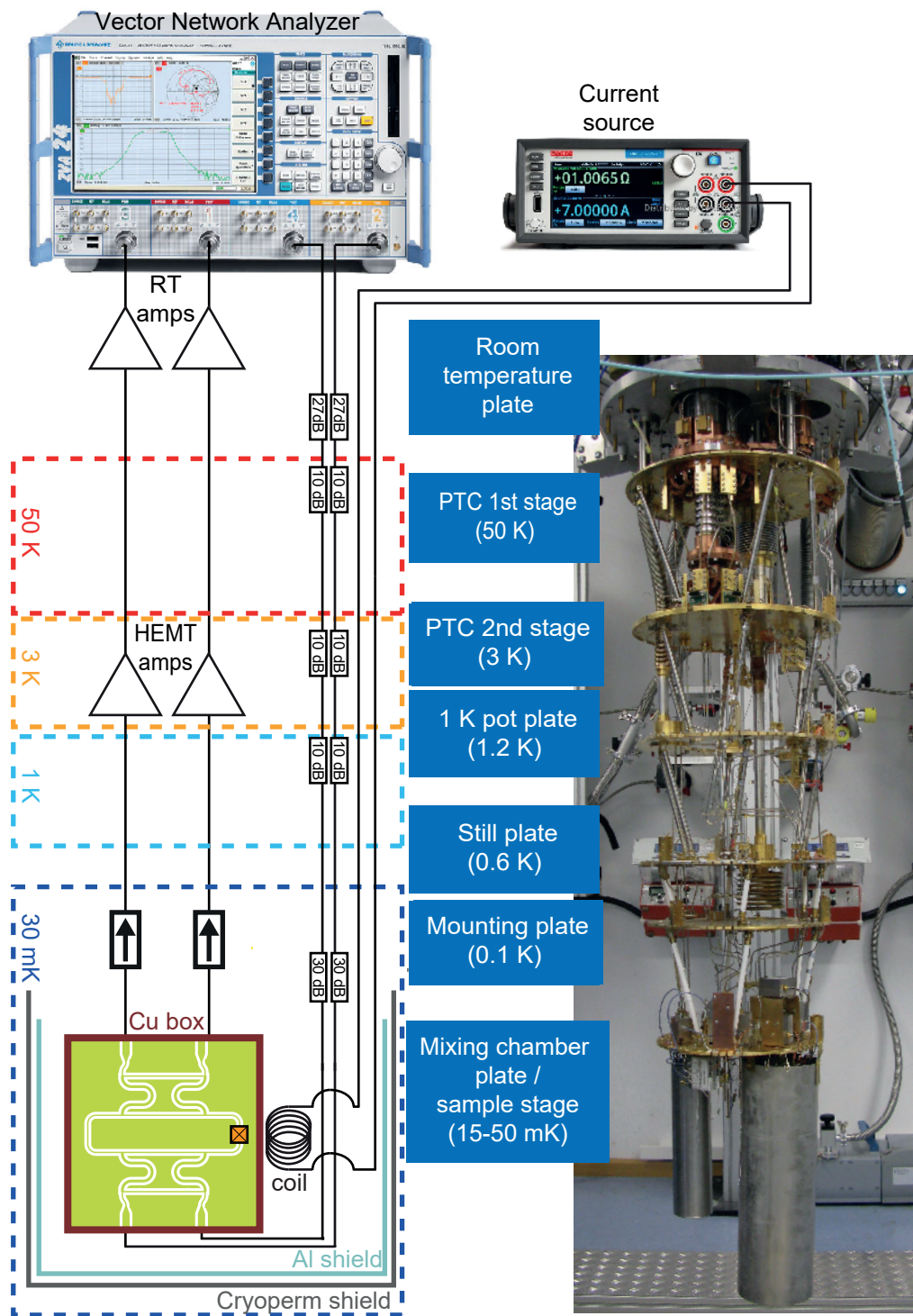


Figure 3.7: Setup of the experiment including cryogenics, cabling, etc. Left: Schematic, Right: Photograph.

### 3.3.1 Packaging

In order to conduct sensitive measurements at the quantum level (1 POA), the samples have to be shielded well against parasitic microwave signals and magnetic fields originating from other simultaneously running experiments or others uncontrollable sources like cell phones etc. Another difficulty is that standard SMA microwave connectors are bulky (diameter 11 mm) and up to eight lines have to be connected for future experiments. To meet these requirements, a special sample holder and packaging has been designed throughout this thesis. In this section, we describe this sample box, and packaging of the samples.

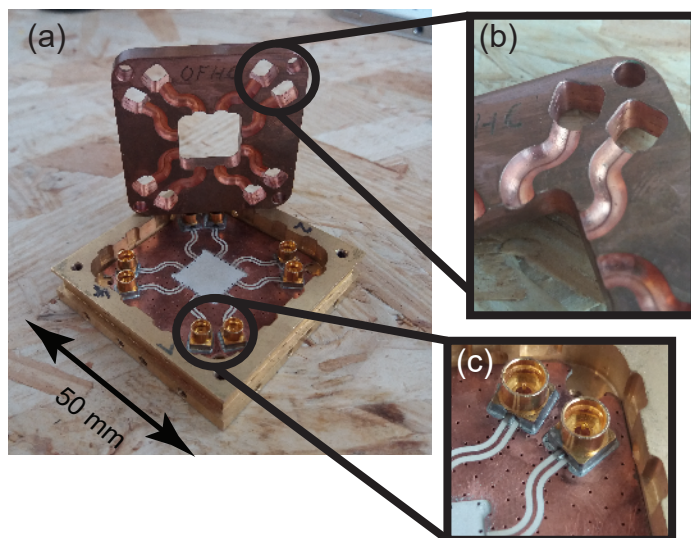


Figure 3.8: (a) Sample box with details: (b) Mode confinement for CPW-lines on PCB. (c) Surface mount connectors.

#### Printed circuit board, sample box, & microwave connectors

To overcome the problem of limited space for components as connectors to connect the microwave cables to the on-chip sample feedlines, we use a printed circuit board (PCB) as an interconnection. The PCB is connected to the micrometer sized on-chip feedlines using wire bonds [see Fig. 3.9(c)].

To generate a clean electromagnetic environment for our quantum circuits, we use a Cu-box confining the microwave field. This minimizes the possible influence of other experiments residing in the same cryostat on our device under test. The sample box is shown in Fig. 3.8 and Fig. 3.9(a,c).

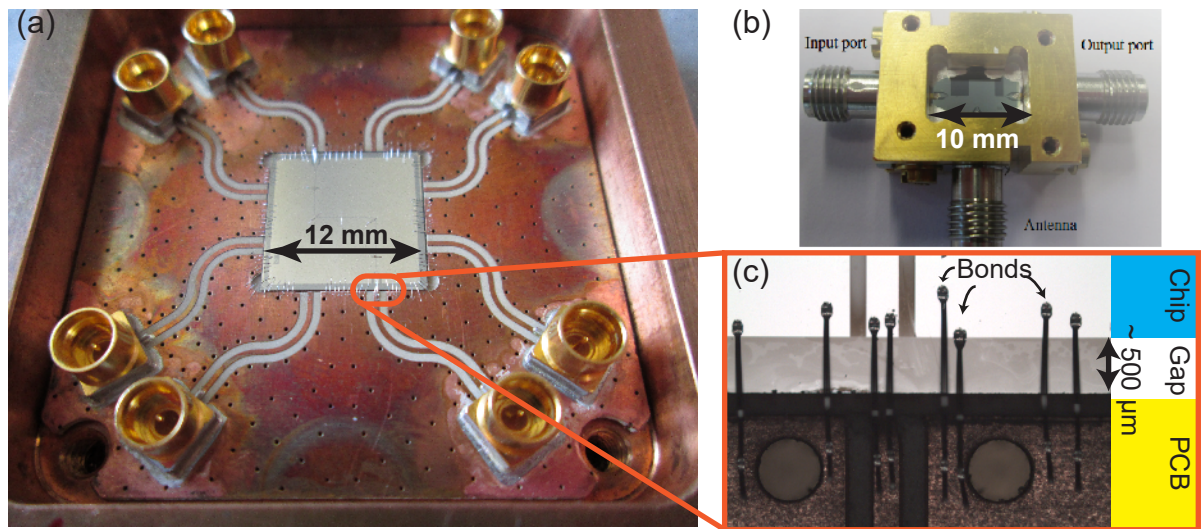


Figure 3.9: (a) PCB with surface mount connectors and CPW-lines. (b) Box with connectors directly mounted on sample chip with silver glue. (c) Close-up on the transition from the PCB to the sample chip. Center conductors and ground planes are connected by wire bonds.

As we use a PCB to interconnect the microwave-cabling to the on-chip feedlines, we need to establish a stable electrical connection guiding our microwave signals from the cables through the PCB and finally onto the sample chip. The microwave cables with sub-miniature push-on (SMP) connectors are connected to the PCB by off-the-shelf surface mount connectors [see Fig. 3.8(a)]. Guiding the microwave signals from the chip to the PCB allows for placing the surface mount connectors such that a lot of input, control and output- lines can be used, as there is enough area on the board to position the connectors on it. The last connection is the one between the PCB and the chip. Here, we decided to go for a well-established solution using wire bonds. In this way, we do not need to position the chip very accurately, because the wire bonds can be adjusted in length and position to overcome the gap between sample and PCB. Compared to using silver-glu [see Fig. 3.9(b)], which was done in earlier experiments at WMI, this technique is superior, because the results are reproducible and the connection does not age. Figure 3.9(c) shows the wire bonds at the PCB to chip transition in detail.

### 3.3.2 Magnetic shielding

To avoid the influence of the earth magnetic field or magnetic fields generated by devices in our lab, we place the sample box inside two cylindrical shields. The outer one is made of cryoperm, the inner one of Al. Cryoperm is a high-permeability

magnetic shielding metal with  $\mu \approx 160\,000 - 250\,000$ , in a temperature range from room temperature down to cryogenic temperatures. The effect of this shield is to have low or none magnetic field inside the probe volume during cooldown. The inner tube is made from Al, which turns superconducting below 1.2 K and thus will freeze the remaining magnetic field. As the magnetic field is negligible during the cooldown process and the inner tube becomes superconducting at base temperature, it prevents fields from entering the probe volume. Thus, we avoid uncontrolled external magnetic fields at our sample chip during the experiments. The result is a very stable working point of the transmon qubit.

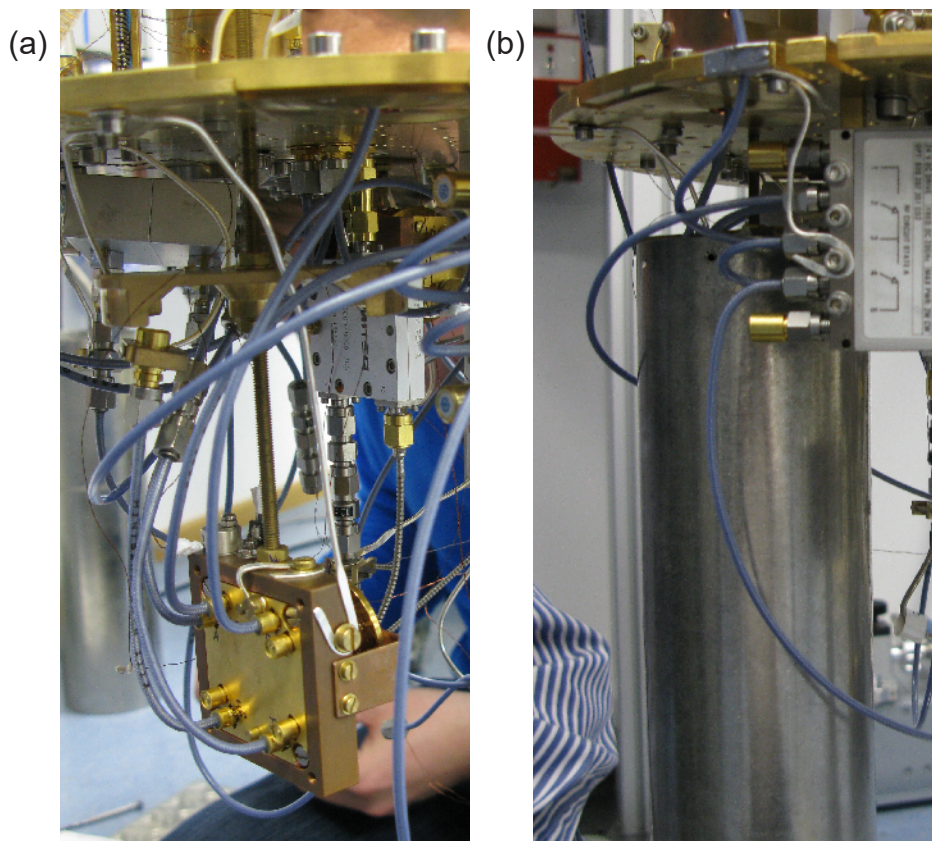


Figure 3.10: (a) The sample box is connected to the microwave lines via SMP connectors. (b) Cryoperm shield. Inner Al-shield and sample box are not visible in (b).

### 3.4 Measurement techniques

For our experiments, we rely on spectroscopic measurements with a VNA. We measure the microwave transmission from one port to the other ports of our sample chips, thus we determine the scattering- or S-parameters [23] of the system (see Sec. 2.1). The characterization of samples without a transmon qubit can be done at higher powers and samples do not consist of tunable circuitry, thus sufficient averaging is done to obtain clear measurement results. No sophisticated data analysis is needed in those cases. In contrast to this, in the following, we want to focus on the measurement of the sample chip, which is composed of an interferometer and a tunable transmon qubit in one of its arms (see Sec. 3.2.3). This sample is measured at very low powers at the level of one photon on average. As explained in Sec. 2.3, the transmon qubit is treated as a scattering potential acting on the incident microwaves. Thus it causes a feature in the transmission spectrum near the frequency  $\omega_{\text{qb}}$ , the qubit working point. The transition frequency of the transmon qubit can be tuned by changing the coil current through the superconducting coil in our setup (see Fig. 3.7), thus setting a transition frequency or working point for the qubit is the same as setting the coil current. In practice, two different data sets are recorded:

- A reference spectrum (without effects caused by the qubit).
- Individual spectra for different qubit working points.

We scan a frequency window of  $\omega_{\text{qb}}/(2\pi) \pm 200$  MHz at different qubit working frequencies  $\omega_{\text{qb},i}$ , where a calibration is conducted for each frequency window with the qubit working frequency set to  $\omega_{\text{qb-cal},i}$  [see Fig. 3.11(b)]. In each of these frequency windows, for several working points of the transmon qubit, transmission magnitude and phase have to be recorded for straight and cross transmission from each input port to the two output ports [see Fig. 3.11(a)].

#### Calibration

To be able to retrieve clean measurement data we perform a specific calibration procedure. We assume that the transmon qubit only affects the transmission spectrum in a small range near its working frequency (see Chapter 2). To measure the spectrum for a qubit working frequency  $\omega_{\text{qb},i}$ , we tune the qubit working frequency to  $\omega_{\text{qb-cal},i}$ , outside the actual measured frequency window by changing the coil current. Then we do a reference measurement for calibration [see Fig. 3.11(b)]. This refer-

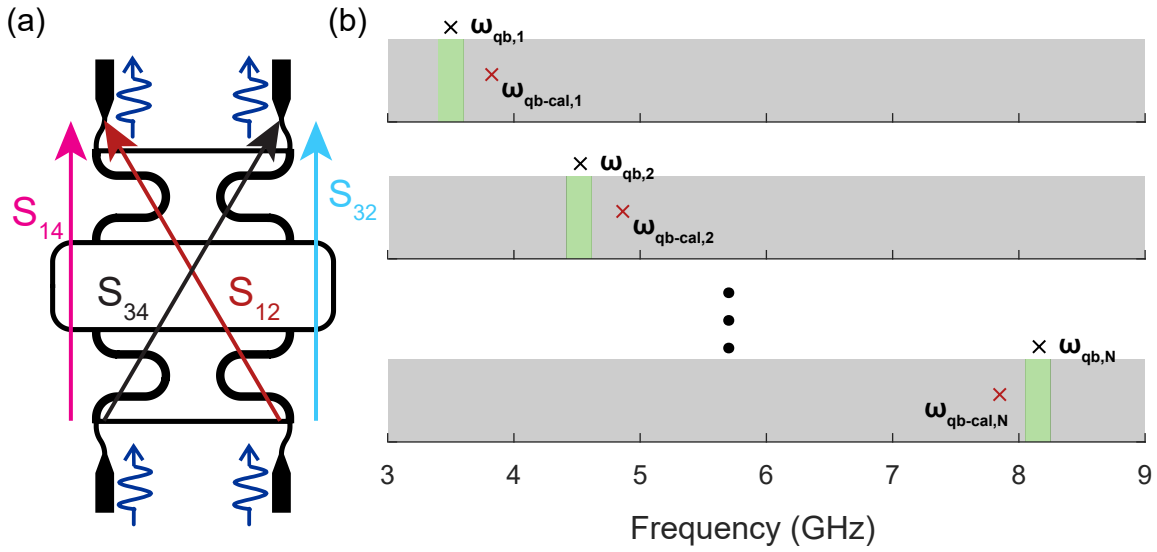


Figure 3.11: (a) Measurement paths for an interferometer (b) We scan a frequency window of  $\omega_{qb}/(2\pi) \pm 100$  MHz at different qubit working frequencies  $\omega_{qb,i}$ . A calibration is conducted for each scan, with the qubit frequency set to  $\omega_{qb-cal,i}$ .

ence can be used for all transmon frequencies we wish to investigate within this particular 200 MHz-window. This reference spectrum we assume to be the spectrum of a bare interferometer for this frequency window.

## Detecting weak signals

Our measurements are conducted using a VNA at powers of  $P \approx 10$  aW at frequencies  $f = 4 - 8$  GHz, thus on very low power at microwave frequencies. Even though we use HEMT amplifiers with low noise figures (typically 10-20 noise photons are added to the signal at 5 GHz [65]), a single shot measurement is not feasible at this power level. To overcome this we do our measurements at a low IF bandwidth setting of 1 Hz of the VNA and do average 10 of these single measurements. This means that the frequency spectrum we look at, usually  $\pm 100$  MHz around the working frequency of the transmon qubit, in a single measurement is scanned for 1 s at every captured frequency. For frequencies in the range of 4 – 8 GHz this means that  $4 \times 10^9 - 8 \times 10^9$  full periods of the probe signal are captured. We conduct such a measurement at every full Megahertz in range  $\omega_{qb} \pm 100$  MHz (201 data points). In this way, we average out most of the statistical errors. The time needed for measuring the spectral vicinity of a single working frequency is  $t_{meas} = 10 \times 201 / (1 \text{ Hz}) = 2010$  s. Adding an initialization time  $t_{init} \approx 90$  s, we end up at about half an hour for measuring the 200 MHz-vicinity for each coil current setting, which is fast compared to time scales

of drifts in the system. Such drifts are expected to happen on the order of several hours.

## Analysis

We record spectra for more than 100 working points of the transmon qubit and use the transfer matrix formalism described in Sec.2.4 to fit the measured data. Thus, determine the relaxation rate  $\Gamma_1$  and the pure dephasing rate  $\Gamma_\varphi$  by numerical fitting of the measured transmission data. Fitting four spectra [two times cross- and two times straight- transmission, see Fig. 3.11(a)], each for magnitude and phase needs serious computational efforts. We handle this by self-written Matlab<sup>®</sup>-routines, based on the usage of parallel computing methods already implemented by internal fitting procedures. For the fitting routines it is important to mention, that we use a two step approach.

First the interferometer parameters center frequency  $\omega_{\text{IF}}$  and arm length  $l$  are varied to fit the data. This is done based on the combined reference data collected at all different qubit working frequencies. In this way we obtained a dataset for the bare interferometer over a broad frequency range of approximately 4 – 8 GHz.

Second, the parameters qubit frequency  $\omega_{\text{qb}}$ , relaxation rate  $\Gamma_1$  and the pure dephasing rate  $\Gamma_\varphi$  are fitted for each individual spectrum associated to a certain qubit working point. Figure 3.12 shows typical transport measurement data and a fitted theory curve. In addition, theory curves with altered parameters are shown to demonstrate the influence of the fitting parameters on the fitted curve.

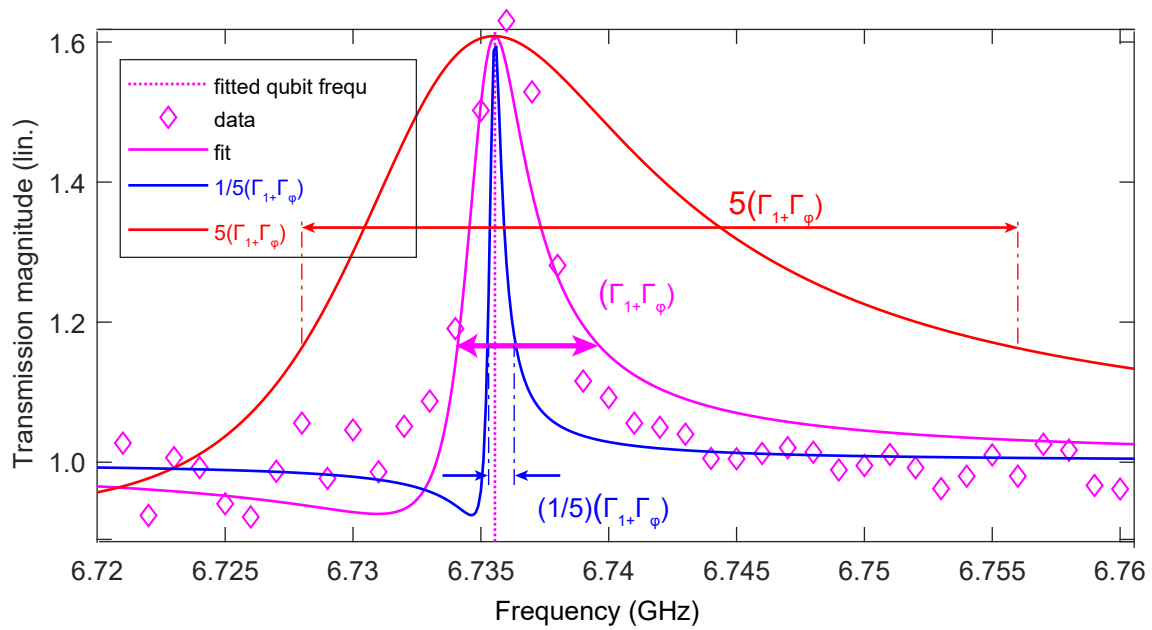


Figure 3.12: Measurement and fit of transmission magnitude and phase for S-parameter  $S_{12}$  around a center frequency of  $\omega_{qb,0}/(2\pi) \approx 6.735$  GHz.

# Chapter 4

## Quantum probe of a broadband on-chip interferometer

This chapter discusses the experimental results obtained throughout this thesis. First, we cover the component tests for the beam splitter, the microwave interferometer, and the transmon qubit, which are the fundamental building blocks of the composite sample used to do the central measurements in this thesis. Finally, we present and interpret data obtained from measurements of the composite sample. These are measurements of the relaxation rate  $\Gamma_1$  and the pure dephasing rate  $\Gamma_\varphi$ , which are used to give insight on the properties of the environment of the transmon placed in one of the arms of the microwave interferometer on our sample chip.

### 4.1 Fundamental building blocks

To learn about the individual components of our final sample design (see Sec. 3.2.3), we first fabricate and test them individually. Thus, in the following, we show characterization measurements for the beam splitter, interferometer, and transmon qubit.

## Beam splitter

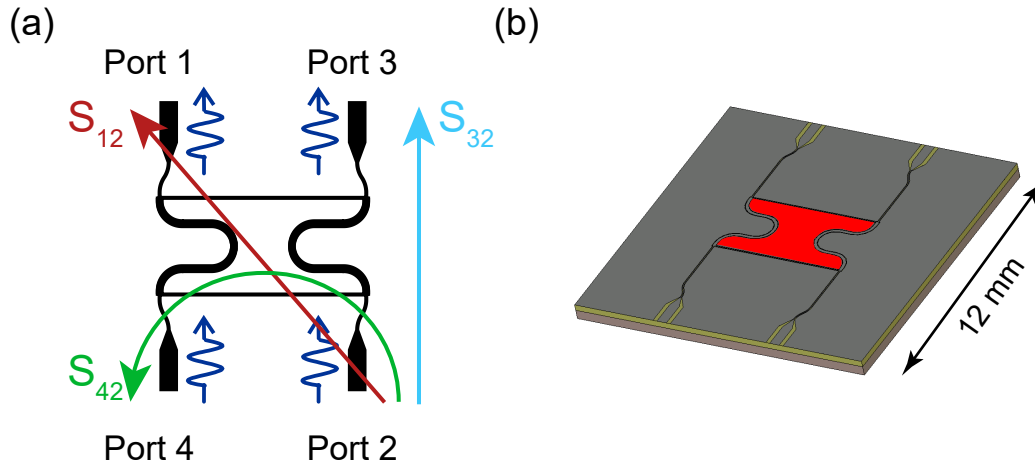


Figure 4.1: (a) Schematic for the beam splitter ports and measured scattering parameters. Red - cross transmission  $S_{12}$ , blue - straight transmission  $S_{32}$ , and green - isolation  $S_{42}$ . (b) Cartoon of sample chip. The CPWs intersect the ground plane and create a floating island in the middle of the chip (red).

Preliminary measurements of beam splitters have been published in the diploma thesis of Ferdinand Loacker [66], showing that we can realize an on-chip beam splitter in the spirit of Ku *et al* [67]. Even though the design can be implemented straightforwardly, some aspects have to be considered.

First, the quadrature hybrid ring design shown in Fig. 4.1(b) contains a conducting island in the middle of the chip. As this island is not electrically connected to the ground plane, it allows for uncontrolled modes. Fig. 4.2 shows simulations of the transmission spectrum of a chip with and without this island being connected to the ground plane. From these simulations, it can be clearly seen that bringing the island to the potential of the ground plane leads to a spectrum much closer to the theoretically expected one. For the actual sample chip the island is connected to the ground plane by on-chip wire bonds to avoid any effects caused by the floating island.

Second, simulations and design studies performed by Michael Fischer and Christian Schneider<sup>1</sup> have revealed that also microwave resonance modes in the Si-substrate of the chip allow for unintended modes and thus have to be considered.

Figure 4.1 shows a schematic and a cartoon of the beam splitter measured as a reference device for the design of our final sample chip. The transmission spectrum of the fabricated on-chip beam splitter has been measured and is depicted in

<sup>1</sup>Data used with kind permission of the authors [25, 68]. Analysis reevaluated for this thesis.

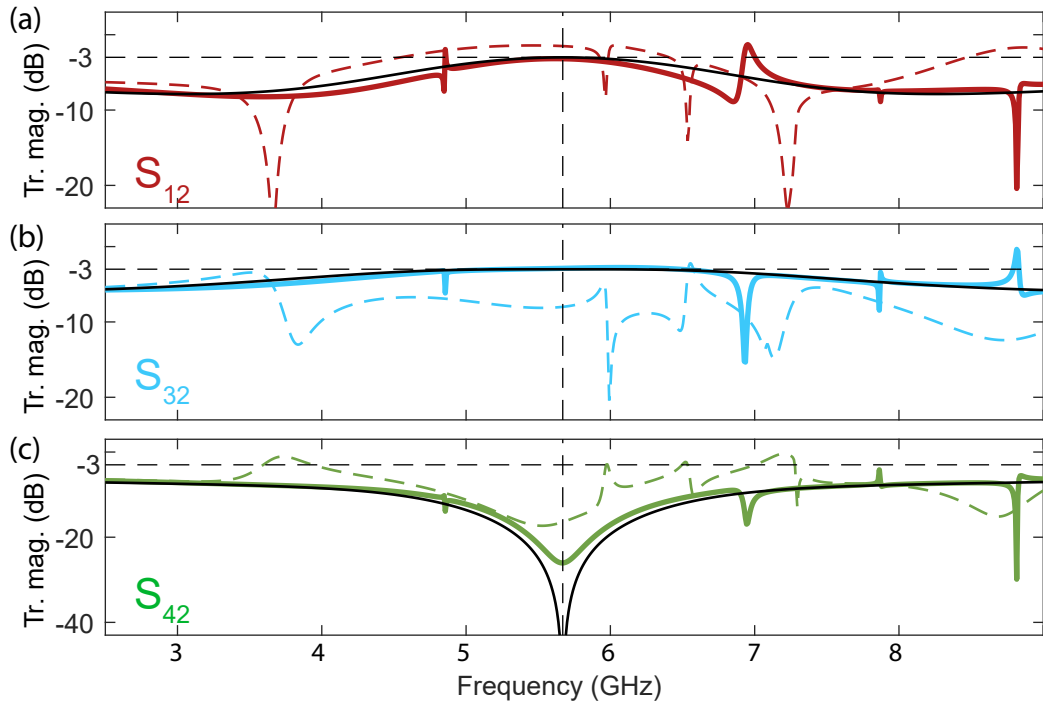


Figure 4.2: Effect of “floating island” in the middle of the beam splitter chip. Solid black lines represent the transmission magnitude (Tr. Mag.) of an ideal beam splitter spectrum, dashed colored lines simulated data with an island of undefined potential and solid colored lines simulation data for the island connected to the outer CPW ground planes (a) Red - Cross transmission  $S_{12}$ , (b) Blue - Straight transmission  $S_{32}$ , and (c) Green - Isolation transmission  $S_{42}$ . The horizontal dashed line marks the 50 percent signal attenuation, the vertical dashed line the beam splitter design frequency  $\omega_{BS}$ .

Fig. 4.3. It shows almost perfect 50-50 splitting for a coherent input signal. In the frequency spectrum, we observe a cross-transmission ( $S_{12}$ ) magnitude of  $-3$  dB in a broad region around the design frequency of  $(\omega_{BS} \pm \Delta\omega)/(2\pi) = 5 - 6.5$  GHz, which is the theoretically expected behavior for a beam splitter (see Sec. 2.3.3). At other frequencies, the spectrum qualitatively follows the theory expectations (see Fig. 4.3), with slight deviations for frequencies far from the designed working frequency.

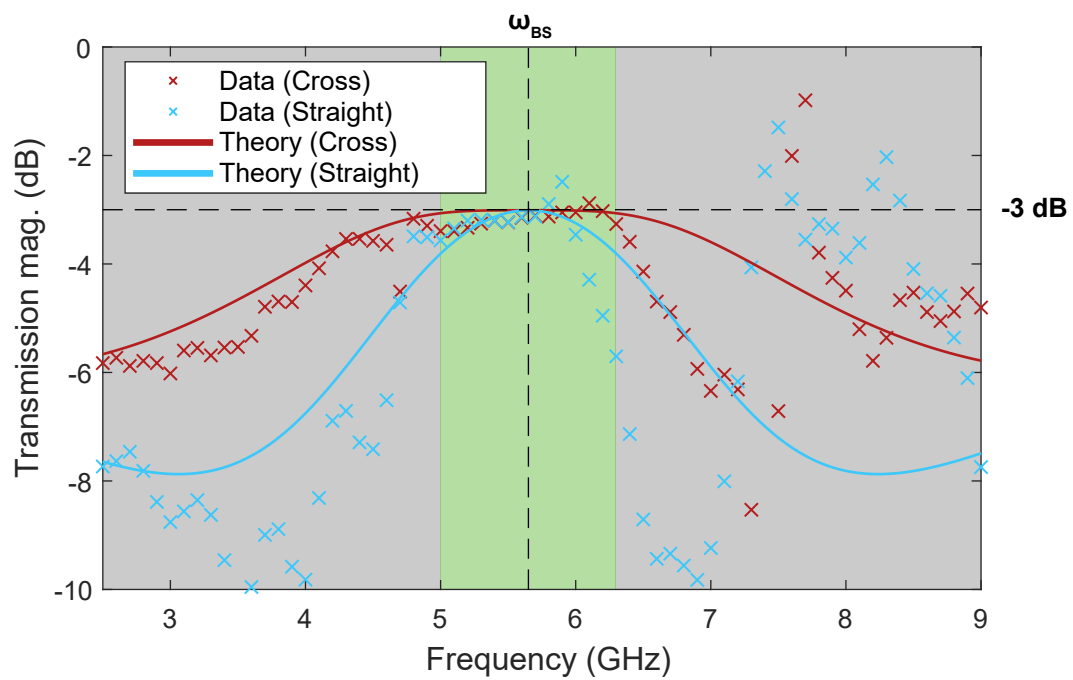


Figure 4.3: The measured spectrum of the beam splitter is close to theory in the frequency range marked green around the working frequency and qualitatively follows the expected behavior for other frequencies.

## Interferometer

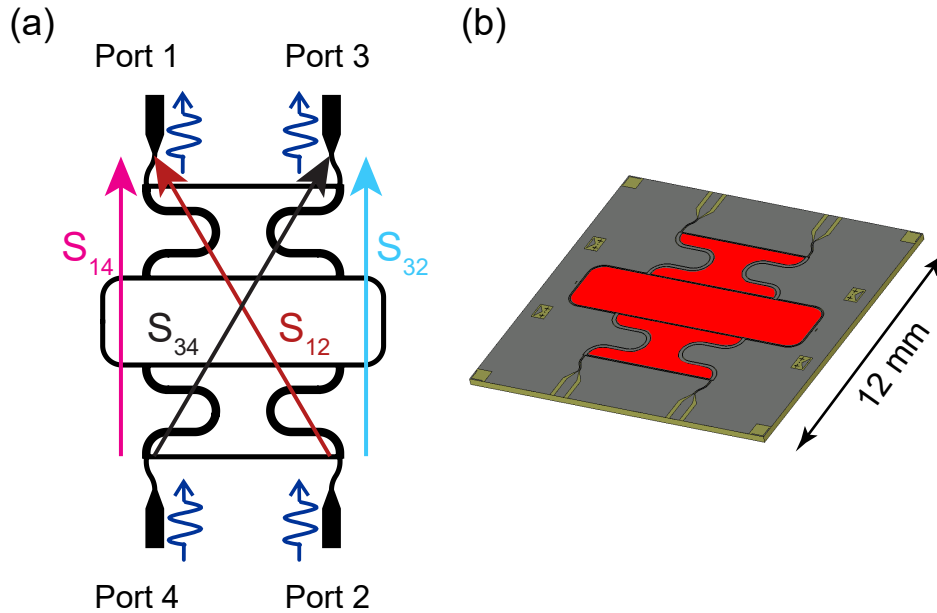


Figure 4.4: (a) Schematic of the interferometer with ports and S-parameters. Cross transmission ( $S_{12}$  and  $S_{34}$ ) and straight transmission ( $S_{14}$  and  $S_{32}$ ). (b) Cartoon of sample. We can identify three islands not connected to the other ground planes (red).

Based on the work of Loacker [66], Schneider [25] and Fischer [68] designed a Mach-Zehnder type microwave domain interferometer. In simulations and measurements, the influence of deviations in key parameters such as characteristic impedance was investigated. For example, the length of the transmission lines (joints) connecting the two beam splitters constituting the interferometer has been investigated. Figure 4.5 shows the theory curves for joints slightly shorter and longer than quarter of a wavelength  $\lambda/4$ . It can be seen that the length of these joints mainly influences the straight transmission in a region where it is highly suppressed. Thus, it can be assumed that imperfections in the joint length will not have negative influence on the performance of an interferometer. From the findings in Refs. [25, 66, 68], an optimized design has been derived, a sample chip has been fabricated and its spectrum has been measured in the frequency range from 2.5 – 9 GHz at liquid helium temperature (for S-Parameter configuration see Fig. 4.4). Additionally, it has been simulated with CST MICROWAVE STUDIO<sup>®</sup>. Theory (lines), simulation (dots) and measurement data (crosses) are compiled in Fig. 4.6. As expected from the behavior of the beam splitter design, in a broad region around the center frequency  $\omega_{IF}/(2\pi) = 5 - 6.5$  GHz the measured interferometer data, qualitatively

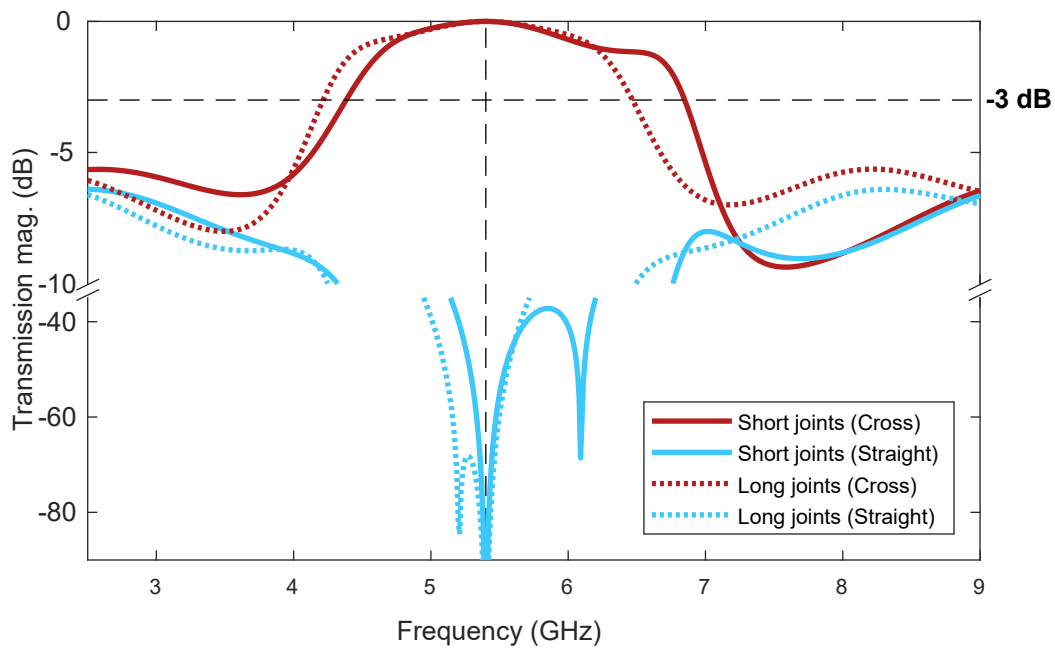


Figure 4.5: Comparison of interferometers with transmission lines of different length  $l$  in between the two constituting beam splitters. Transmission magnitude is shown for  $l = 4.0 \text{ mm} < \lambda/4$  (solid lines) and for a length  $l = 6.0 \text{ mm} > \lambda/4$  (dashed lines), where  $\lambda/4 = 5.2 \text{ mm}$ .

follows the expected behavior of perfect transmission in a calibrated measurement.

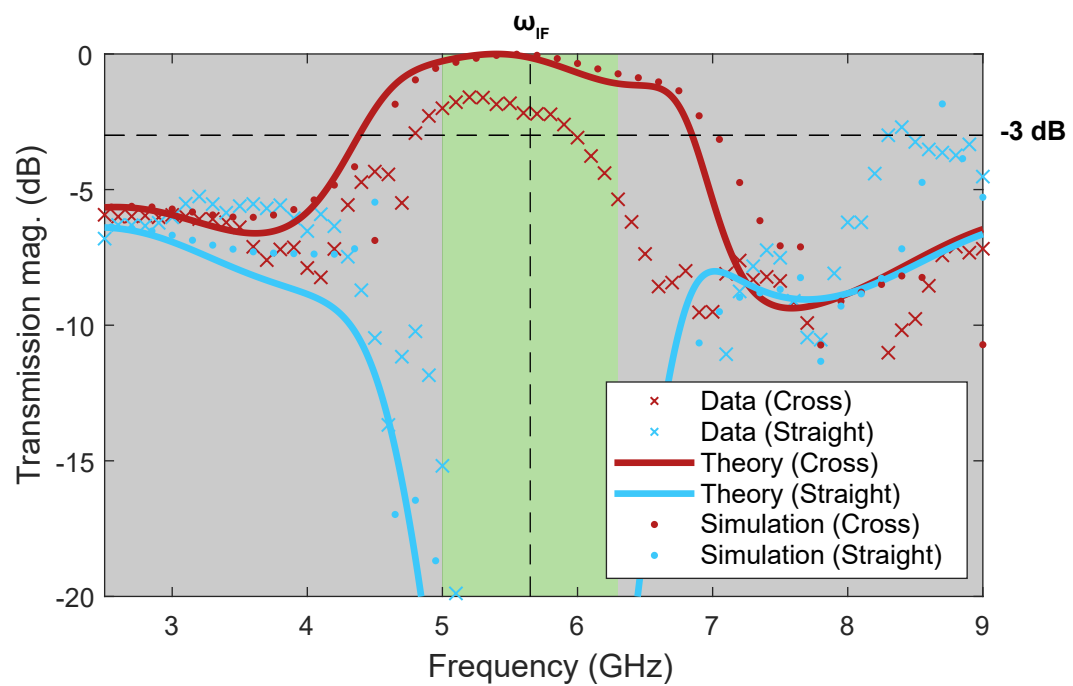


Figure 4.6: Transmission magnitude vs. frequency for the interferometer ( $l = 5.2 \text{ mm} = \lambda/4$ ) in the frequency range from 2.5 – 9 GHz, measured at liquid helium temperature.

## Transmon qubit

To characterize the transmon qubit, the design from Sec. 3.2.3 has been realized inside a  $\lambda/4$  resonator<sup>2</sup>. We use single- and two-tone measurements, depending on the measurement regime [49], to do transmission measurements. In order to tune the qubit transition frequency, a superconducting coil is generating magnetic flux threading the SQUID loop of the transmon qubit. Figure 4.9 shows the qubit transition frequency as a function of the coil current. Here, the data near the anticrossing is measured using single-tone spectroscopy, while, for frequencies far off the bare resonator frequency  $\omega_{\text{res}}/(2\pi) = 6.54$  GHz, two-tone spectroscopy is used. The inset in Fig. 4.9 gives a detailed view on the anticrossing, showing more measurements than the main plot. We observe a full period in modulation of the qubit frequency with flux for a change in current of about 1 mA. This allows for a relation between the coil current and the flux threading the SQUID loop of the transmon qubit with  $1 \Phi_0 \leftrightarrow 995.4 \mu\text{A}$ .

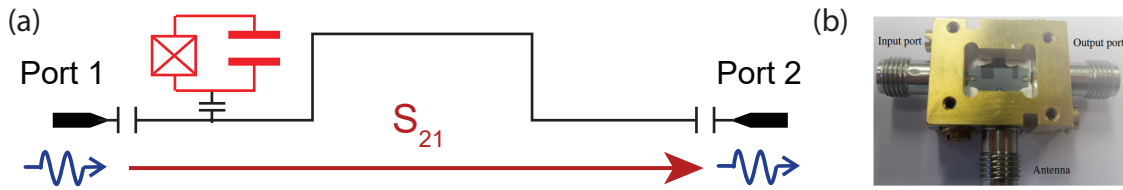


Figure 4.7: (a) Schematic of the transmon qubit in a resonator. Transmission is measured via the  $S_{21}$ -parameter. (b) Photograph of sample in a box with SMA-connectors.

From the data, we fit the characteristic parameters of the transmon qubit. The Josephson energy is found to be  $E_J/h = 20.0$  GHz, the charging energy  $E_C/h = 592.4$  MHz and the coupling to the  $\lambda/4$  resonator  $g/(2\pi) = 71.3$  MHz. These parameters<sup>3</sup> are summarized in Tab. 4.1.

<sup>2</sup>Data used with kind permission of Javier Puertas[49]. Analysis reevaluated for this thesis.

<sup>3</sup>Small deviations compared to the thesis are not relevant, as the fabricated sample is used for the proof of principle and to know the parameter regimes. The actual sample is not used to produce the main results of this thesis.

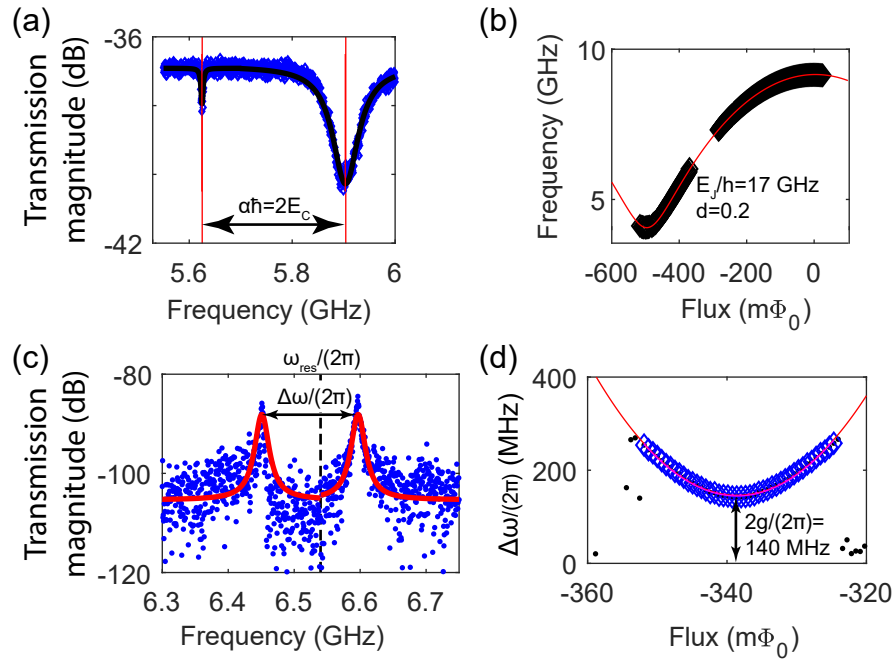


Figure 4.8: Reevaluated from Ref. [49]: (a) Qubit anharmonicity (b) Josephson energy  $E_J$  and asymmetry parameter  $d$  (see Sec. 2.4.3). (c) Avoided crossing (d) Qubit-resonator coupling

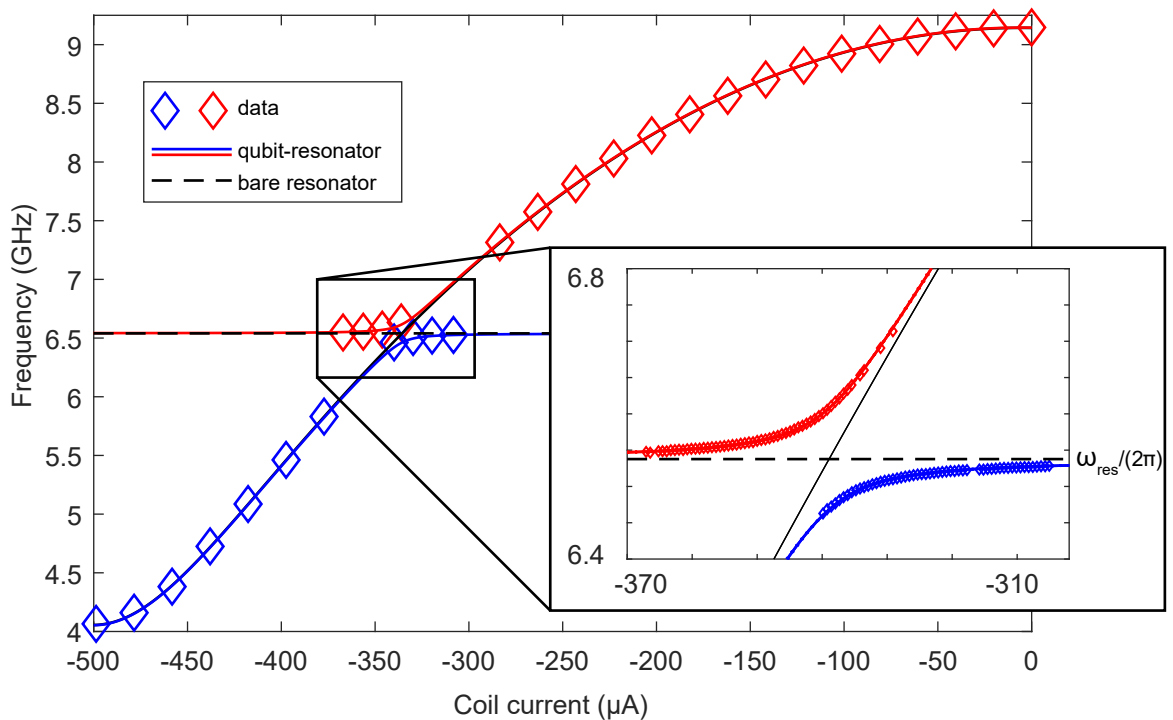


Figure 4.9: Flux dependence of the transmon qubit transition frequency measured by a resonator using two-tone spectroscopy [49]. Diamonds: data. Lines: fits (see Qubit-resonator coupling in Sec. 2.4.3). Inset: Region around the avoided crossing with more data points using single-tone spectroscopy.

Parameter	Value	Error
Josephson energy $E_J/h$	18.8 GHz	10.6 GHz
Charging energy $E_C/h$	557.6 MHz	1.5 MHz
Coupling to resonator $g/(2\pi)$	73.0 MHz	$\pm 0.7$ MHz
Asymmetry parameter $d$	0.2	n.a.

Table 4.1: Parameters of the transmon qubit, based on a reevaluation of the data obtained by Javier Puertas [49].

## 4.2 Transmon qubit in interferometer

In this section, we discuss the main objective of this thesis: the measurements on a transmon qubit in one arm of an interferometer. The individual components have been analyzed in the previous sections, but now we want to see the interplay of the transmon qubit with the broadband engineered environment of an interferometer. We clearly expect the qubit to only have an influence in a small frequency range near its working frequency, while the spectrum of the sample at other frequencies should be determined by the interferometer structure. Indeed, compared to the spectrum of a bare interferometer, we find a distortion in the frequency response which is shifting when we adjust the coil current.

Using the setup explained in Sec. 3.3, we measure the frequency dependence of different S-parameters  $S_{12}, S_{32}, S_{14}, S_{34}$  of our sample (see Fig. 4.10). Figure 4.11 shows exemplary transmission measurements.

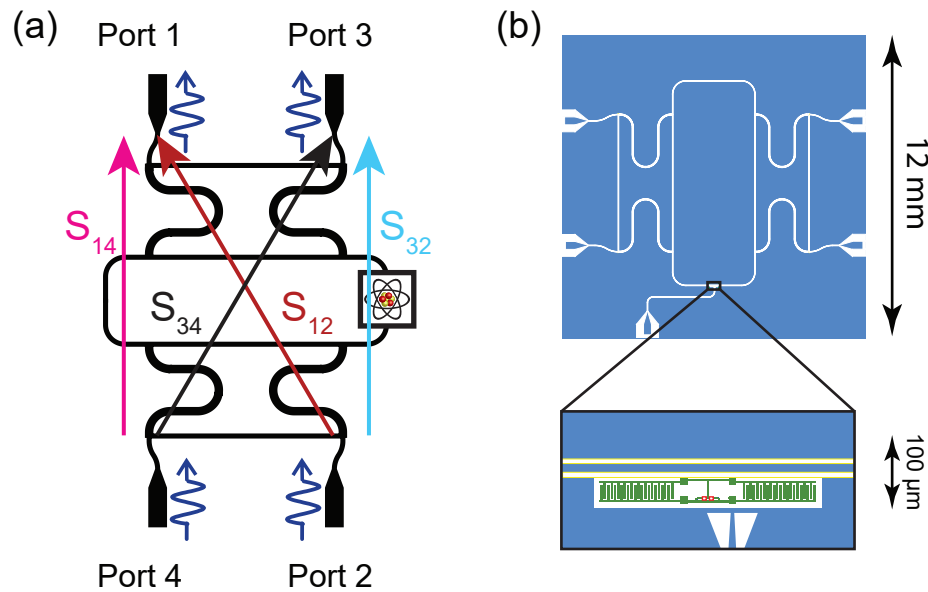


Figure 4.10: (a) Schematic for the interferometer with a transmon qubit in one arm, ports and measured S-parameters. (b) Sample mask with zoom on transmon qubit circuit (blue...Nb structures, green...Al structures, white...substrate). Red rectangles show the positions of the JJs.

### Interferometer and Transmon qubit parameters

The measurements of the individual components (see Sec. 4.1) give us the confidence to understand how these behave and which are the parameter ranges to expect.

Nevertheless, the interferometer center frequency  $\omega_{\text{IF}}$  and the main transmon qubit parameters such as maximum Josephson energy  $E_J$ , charging energy  $E_C$ , and asymmetry parameter  $d$  have to be evaluated for the combined sample. All parameters are evaluated by fitting transmission magnitude and phase obtained via the procedure explained in Sec. 3.4 for straight and cross transmission [see S-Parameters in Fig. 4.10(a)]. Figure 4.11(a) shows typical data measured in the vicinity of a specific qubit working frequency. Also, the theory line resulting from fitting the model to the data is depicted. In this way, 109 qubit working points are analyzed. To

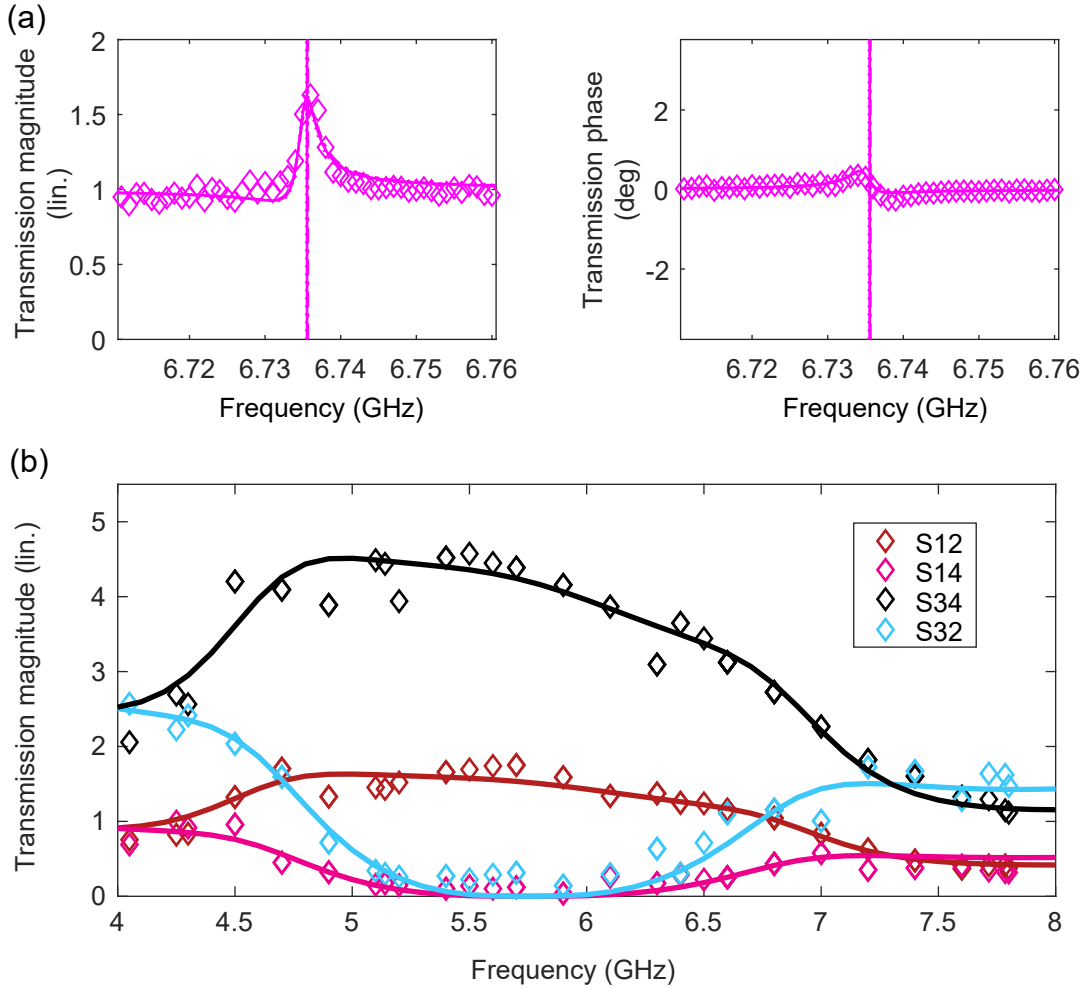


Figure 4.11: (a) Data and fit of magnitude (in linear units) and phase for a cross transmission measurement for  $\omega_{\text{qb}}/(2\pi) \approx 6.735$  GHz. (b) The spectrum of the bare interferometer can be obtained by combining the information of all calibration measurements (not all data points are shown in this plot).

gain information on the interferometer center frequency  $\omega_{\text{IF}}$ , we combine the calibration data from all frequency segments (see Fig. 3.11) to compile a transmission measurement for the bare interferometer. The result is shown in Fig. 4.11(b). We

find the interferometer center frequency to be  $\omega_{\text{IF}}/(2\pi) = 5.75$  GHz. Next, the

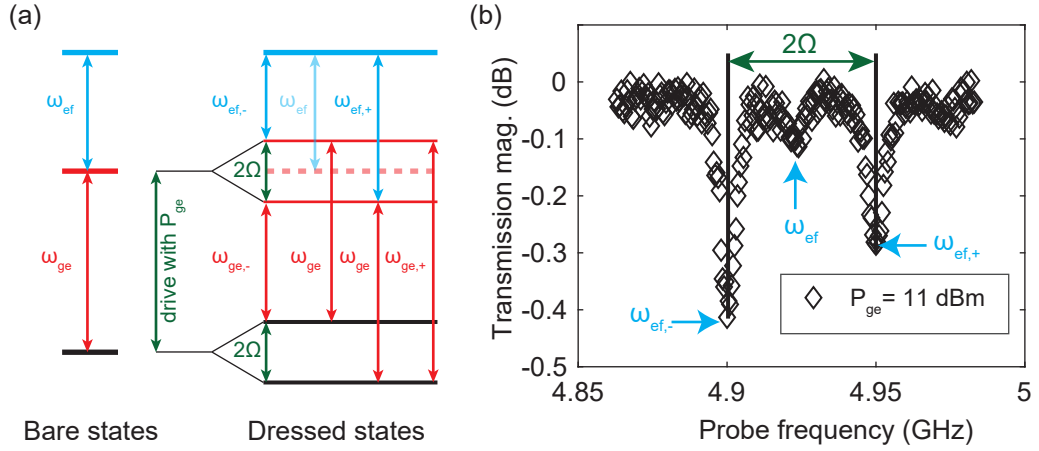


Figure 4.12: Autler Townes splitting. (a) Bare states vs. dressed states resulting from strong driving of the first qubit transition. (b) The frequency of the second qubit transition  $\omega_{\text{ef}}$  is obtained by measuring the Autler Townes splitting.

intrinsic parameters of the transmon qubit are determined. These are charging energy  $E_C$ , maximum Josephson energy  $E_J$ , and asymmetry parameter  $d$ . We start with the charging energy  $E_C$ , which is equal to the negative qubit anharmonicity  $\alpha$ , given by the difference of first ( $\omega_{\text{ge}}$ ) and second ( $\omega_{\text{ef}}$ ) qubit transition frequency  $\alpha = 2(\omega_{\text{ef}} - \omega_{\text{ge}}) = -E_C$  and  $P_{\text{ge}} = 11$  dBm. We determine it from a mollow triplet experiment similar to the one described in Ref. [69]. We apply a drive tone with a large strength  $P_{\text{ge}}$  at the frequency of the first qubit transition  $\omega_{\text{ge}}$ . The strong driving causes a splitting of the qubit levels by  $2\Omega \propto P_{\text{ge}}$  (data not shown) [70]. To find the frequency of the second qubit transition, we use an additional, weaker probe tone. The frequency of the second excited level is then given by  $\omega_{\text{ef}} = (\omega_{\text{ef,+}} + \omega_{\text{ef,-}})/2$ , where  $\omega_{\text{ef,+/-}}$  are the shifted second excited qubit levels [see Fig. 4.12(a)]. Knowing the first qubit transition frequency  $\omega_{\text{ge}}$  from resonance fluorescence spectroscopy, we can easily find the anharmonicity  $\alpha$  and thus the charging energy. Figure 4.12(b) shows this for a qubit working frequency  $\omega_{\text{qb}}/(2\pi) = \omega_{\text{ge}}/(2\pi) = 5.5$  GHz. The charging energy is the same for all qubit working frequencies, as it depends on the geometry of the qubit structure only, not on the flux in the SQUID loop. We find the charging energy to be  $E_C/\hbar = 573 \text{ MHz} \pm 4 \text{ MHz}(2\pi)/\hbar$ .

Finally, maximum Josephson energy  $E_{J0}/h = 17.9 \text{ GHz} \pm 190 \text{ MHz}$  and asymmetry parameter  $d = 14\% \pm 0.7\%$  are extracted from the dependency of the qubit working frequency on the coil current, thus on the flux threading the SQUID loop of the transmon qubit (see Fig. 4.13).

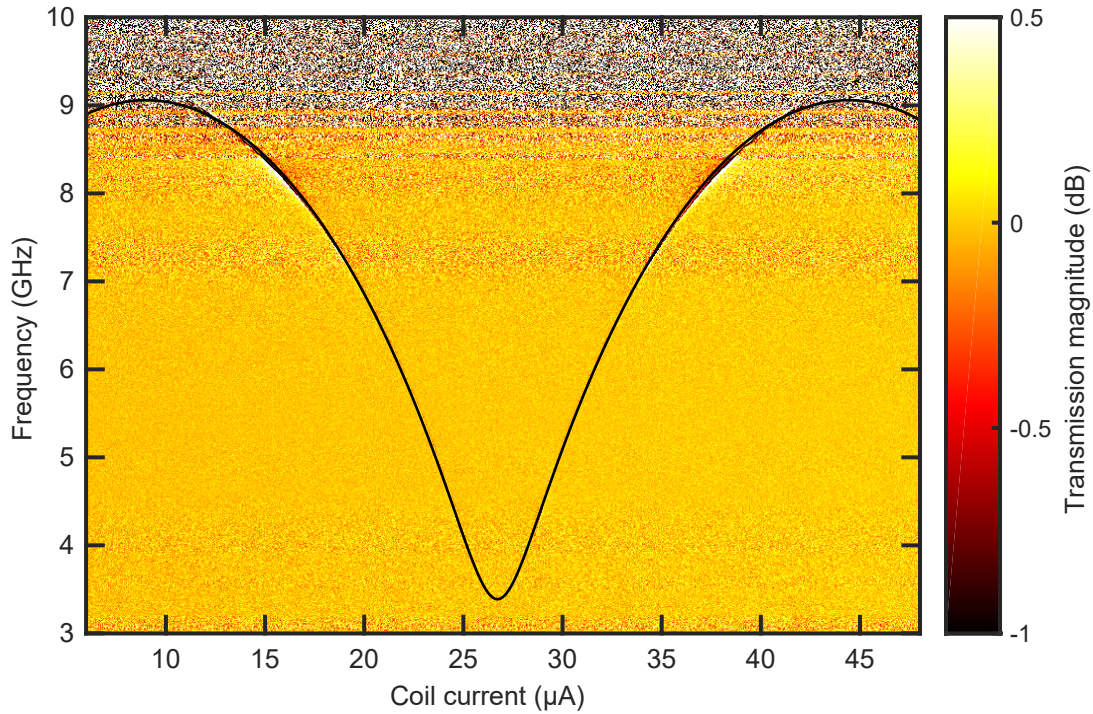


Figure 4.13: Resonance fluorescence spectroscopy: Cross transmission magnitude as a function of frequency and coil current. The black line is a fit to the deviations in the calibrated spectrum of the DUT caused by the transmon qubit using Eq. (2.86).

### Qualitative analysis - frequency regimes

Analyzing the transmission measurements, near the qubit frequency for various coil currents, we identify three different regimes showing different structures in the frequency domain (see Fig. 4.11 for a typical measurement). These deviations from the calibrated interferometer spectrum, which would show unity transmission for all frequencies, are known as fano-features [71] resulting from the constructive or destructive interference of the signals scattered off the qubit and recombined at the second beam-splitter of the interferometer circuit. In cross-transmission ( $S_{12}$  and  $S_{34}$ ) measurements, for working frequencies of the transmon qubit  $\omega_{qb}/(2\pi) < 5$  GHz, we find peak-dip in magnitude and dip-peak structures in phase, while for working frequencies  $\omega_{qb}/(2\pi) \approx \omega_{IF}/(2\pi) = 5.75$  GHz, thus near the center frequency of the interferometer, we just observe a dip in magnitude and dip-peak in phase, and for frequencies  $\omega_{qb}/(2\pi) > 6.5$  GHz we again observe peak-dip in magnitude and dip-peak structures in phase.

For the ideal interferometer, in straight-transmission ( $S_{14}$  and  $S_{32}$ ) measurements, the transmission is zero near the center frequency. This leads to inaccuracies with calibration, and thus, to poor data and fit quality in the region where the trans-

mitted signal is strongly suppressed. Nevertheless, some data and fits are shown in Fig. 4.14(c). The role of peak and dip is interchanged for magnitude and phase in the regime near the working frequency of the interferometer  $\omega_{\text{IF}}$ . For frequencies  $\omega_{\text{qb}}/(2\pi) < 5 \text{ GHz}$  and  $\omega_{\text{qb}}/(2\pi) > 6.5 \text{ GHz}$ , we once more observe peak-dip in magnitude and dip-peak structures in phase.

Near the design frequency of the interferometer, we expect the transmon qubit in the interferometer to behave similarly to a qubit in a simple transmission line [9, 16, 40]. The interferometer spectral response in this frequency range is similar to an open transmission line. Signals are not reflected at the beam splitters. This is exactly what is observed for  $5 \text{ GHz} < \omega_{\text{qb}}/(2\pi) < 6.5 \text{ GHz}$ . As we move the working frequency of the transmon qubit away from the design frequency of the interferometer, the beam splitters start to have finite reflections. The two beam splitters in this regime act as a Fabry–Pérot interferometer [72]. This leads to the Fano-features in Fig. 4.14.

## Quantitative analysis

The characteristic shape of the fano-resonances is determined by the relaxation rate  $\Gamma_1$  and dephasing rate  $\Gamma_\phi$  of the transmon qubit (see Sec. 2.4.3) in one of the interferometer arms. These parameters are obtained by fitting a theory model [see Eq. (2.107)] to the measured transmission spectra at each individual transmon qubit working frequency. This approach allows for a quantitative analysis of the dependency of  $\Gamma_1$  and  $\Gamma_\phi$  on the transmon qubit working frequency. We find that the qubit relaxation rate  $\Gamma_1$  is dominated by high frequency noise near the qubit transition rate, while the qubit dephasing rate  $\Gamma_\phi$  is governed by noise at low frequencies, below 10 kHz.

The qualitative discussion of the transmission spectra in Sec. 4.2 shows that the very same qubit produces different spectra for different working frequencies depending on the position in frequency space relative to the center frequency of the interferometer  $\omega_{\text{IF}}$ . Thus, a quantitative analysis must take into account all scattering and interference effects on the sample chip (see Sec. 3.2.3 for details on the design). To describe this situation, we choose the transfer matrix approach [73] (see Sec. 2.4.4), where the transmon qubit is treated as a scatterer of the incident signal [40]. The relaxation rates of the qubit are modeled within the framework of the SBM, while the dephasing rates are treated in an Ornstein-Uhlenbeck approach (see Sec. 2.5.2). We expect the qubit relaxation rate to have a linear dependence on the qubit working frequency,  $\Gamma_1 = \alpha\omega_{\text{qb}}$  [16]. The linear scaling (Ohmic bath,

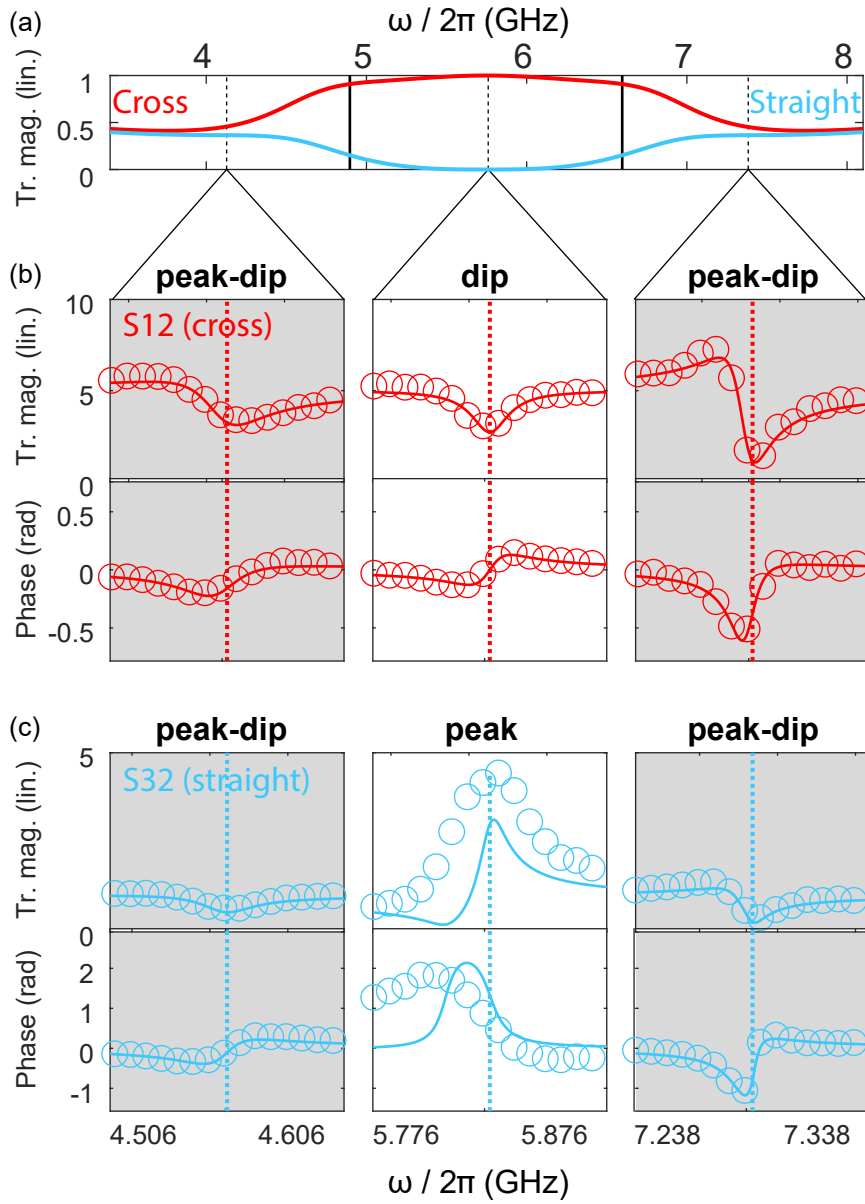


Figure 4.14: (a) Cross (red) and straight (light blue) transmission magnitude (Tr. mag.) in linear units as a function of the probe frequency for the bare interferometer in theory. (b) Measured cross transmission magnitude (Tr. mag.) in linear units and phase in rad as a function of the probe frequency at three different qubit transition frequencies  $\omega_{\text{qb}}/(2\pi) = 4.556$  GHz,  $5.826$  GHz, and  $7.288$  GHz. The solid lines show the results of a fits of our transfer matrix model (see Eq. 2.107) to the data. The fits are in good agreement with the experiment. (c) Measured straight transmission magnitude and phase at the same qubit transition frequencies. Evidently the dip and peak structure near  $\omega_{\text{IF}}/(2\pi) = 5.75$  GHz is inverted.

see Sec. 2.5.1) is due to the fact that, assuming a high-frequency cutoff  $\omega_c$ , Ohmic dissipation causes an effective bath spectral density linear in frequency,  $J(\omega) = \alpha\omega$ , where  $\alpha$  corresponds to a friction constant. Note that the dimensionless parameter  $\alpha$  reflects the strength of dissipation, which in a physical system depends on the amplitude of the noise and its coupling strength.

Analyzing the measured transmission spectra by the transfer matrix model, we can derive the important qubit parameters relaxation rate  $\Gamma_1$  and dephasing rate  $\Gamma_\phi$  in a quantitative way. From a numerical fit of our model to the measured cross-transmission data  $S_{34}$  and  $S_{12}$  [see Fig. 4.14(b)], we extract the qubit transition frequency as well as the relaxation and dephasing rates. As mentioned above, the straight transmission is expected to have poor data quality [see Fig. 4.14(c)]. Thus, we discard  $S_{14}$  and  $S_{32}$  and use  $S_{34}$  and  $S_{12}$  for our analysis.

Within a 95%–confidence interval, the statistical error of the extracted qubit transition frequency is below 2%. For  $\Gamma_1$  and  $\Gamma_\phi$ , we typically observe statistical errors below 33%. Thus, we obtain a reliable set of data for the decoherence properties of the transmon qubit over a wide range of qubit transition frequencies (4 – 8.5 GHz). The excellent fit quality of the individual spectra for most qubit transition frequencies and the reproduction of the regimes seen in Fig. 4.14, provide strong evidence for the validity of the applied model. Additionally, as expected by design, our measurements confirm that the interferometer predominantly dictates the transmission spectrum of the system, except for a small region of approximately 100 MHz near the qubit transition frequency.

## Decoherence analysis

In order to gain information about the local electromagnetic environment of the qubit, we use the transmon qubit as a sensitive broadband spectrometer in this section. The measurement is broadband, as we capture the transmission spectrum of the qubit at several working points in a frequency range of 4 – 9 GHz. It is sensitive as the transmon qubit is probed at and reacts to the energy of single microwave photon, where  $E = \hbar\omega$ . In the relevant frequency range this corresponds to an energy of  $E = \hbar\omega = 0.42 - 0.95$  yJ or  $2.63 - 5.92$   $\mu$ eV. In comparison, the energy of photons of visible light  $E = h(c/\lambda)$  are in the range  $E = 1.65 - 2.95$  eV, is higher by a factor of  $2 \times 10^6$ . From the individual qubit spectra, we extract the relaxation rate  $\Gamma_1$  and the pure dephasing rate  $\Gamma_\phi$  at each qubit frequency  $\omega_{\text{qb}}$ . Analyzing these by fitting model parameters of the SBM and the Ornstein-Uhlenbeck model

to the obtained data points, we are able to deduce the nature of the environment of the qubit. On top of that, deviations from the expected functional dependencies of  $\Gamma_1$  and  $\Gamma_\Phi$  on the qubit frequency indicate possible errors in microwave design or fabrication.

### Qubit relaxation $\Gamma_1$ - high frequency noise

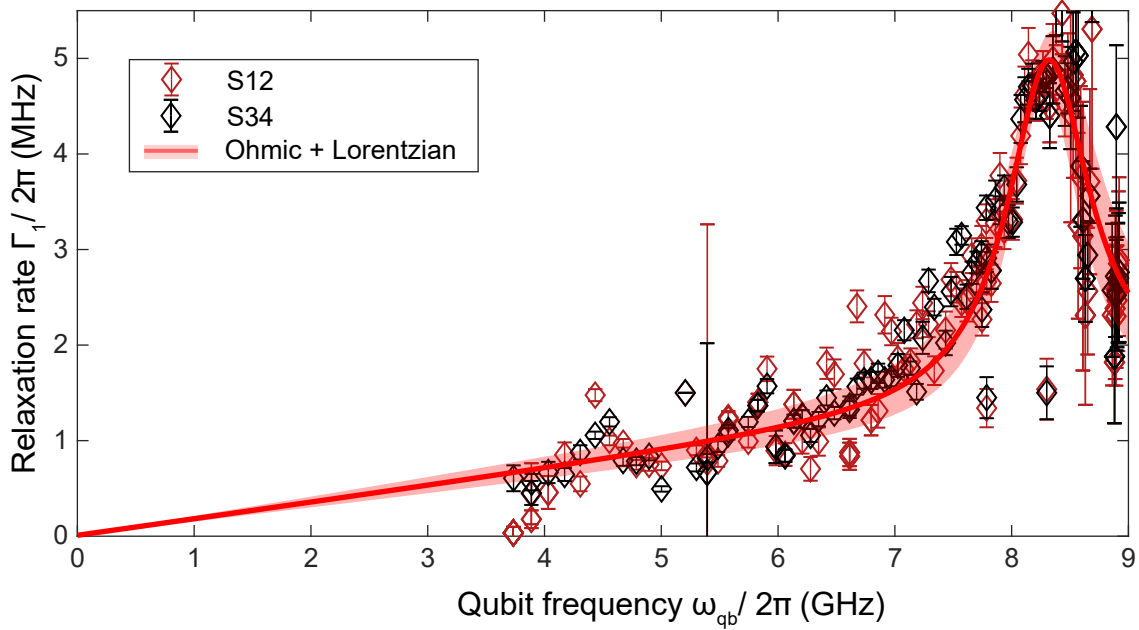


Figure 4.15: Fitted relaxation rate for different qubit working points. The red line shows a fit to an Ohmic line. A Lorentzian accounts for the observed rise in  $\Gamma_1$  above 8 GHz.

Following a Golden rule argument, the relaxation rate  $\Gamma_1$  is proportional to the noise power spectral density at the qubit transition frequency  $S(\omega_{qb})$ . Hence, the measurement of  $\Gamma_1$  as a function of qubit transition frequency allows us to obtain information on  $S(\omega)$ . Therefore, we use the  $\Gamma_1$  values extracted for working frequencies of the transmon qubit between 4 and 8.5 GHz to derive valuable information on the interaction of the qubit with its electromagnetic environment.

Figure 4.15 shows that our  $\Gamma_1$  data follows a linear trend for frequencies up to about 7 GHz, as expected for an ohmic environment (see Sec. 2.5.1). This clearly supports our initial assumption that the transmission line coupled to the qubit provides an Ohmic bath. Interestingly, deviations from the Ohmic environment are rather small in the range between 4 GHz and 7 GHz although the coupling strength is low in comparison to other experiments [17]. For frequencies above 8 GHz, we

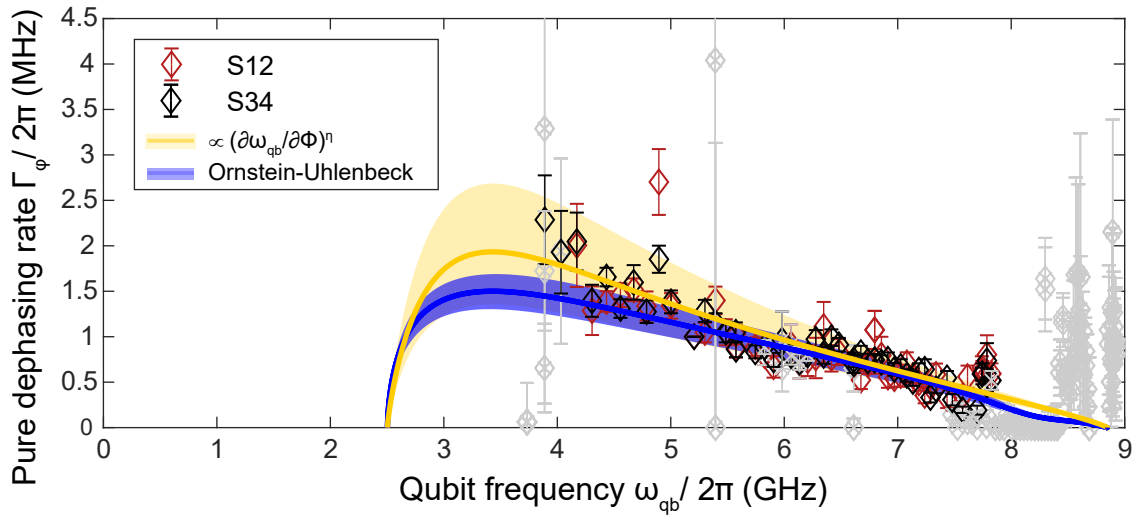


Figure 4.16: Single tone measurements for transmon qubit in resonator.

observe a pronounced rise in  $\Gamma_1$  which provides a hint to the presence of an additional on-chip mode coupling to the qubit. In a first-order approximation, we model this mode by an additional Lorentzian (center frequency  $\omega_{L0}/2\pi = 8.3$  GHz, full width half maximum  $\Gamma/2\pi = 1.5$  GHz) on top of the linear Ohmic background. By fitting the data, we find  $\alpha = (1.7 \pm 0.3) \cdot 10^{-4}$ , corresponding to  $\tilde{d} = (6.9 \pm 2.7) \cdot 10^{-21}$  A s. In order to find a more quantitative evidence for the transmission line to be the dominant bath for qubit relaxation, we also determine  $\alpha_{\text{res}} = \pi(g_{\text{res}}/\omega_{\text{res}})^2 = (3.6 \pm 0.04) \cdot 10^{-4}$  in the qubit-resonator system described in Sec. 3.2.3. The good agreement between  $\alpha$  and  $\alpha_{\text{res}}$  clearly confirms the validity of the SBM-based data analysis.

### Qubit dephasing $\Gamma_\phi$ - low frequency noise

Here, we characterize the noise causing pure dephasing of the transmon qubit inside the interferometer circuit. For the subsequent analysis, we only consider  $\Gamma_\phi$ -values with less than 33% statistical error in the fitting to the transmission spectrum data. It is well established that flux noise through the dc SQUID loop is a dominant source for the fluctuation of the transmon qubit transition frequency  $\omega_{\text{qb}}$ , leading to dephasing [42, 74–76]. As a consequence, we expect a strong dependence of  $\Gamma_\phi(\omega_{\text{qb}})$  on the first derivative of  $\omega_{\text{qb}}$  with respect to flux  $\Phi$  [74]. Indeed, our data is well fitted with the ansatz  $\Gamma_\phi \propto (\partial\omega_{\text{qb}}/\partial\Phi)^\eta$ , as shown in Fig. 4.16. Interestingly, the exponent  $\eta \simeq 1.64 \pm 0.21$  suggests that the observed flux noise may be appreciably correlated rather than simple white noise, for which an exponent of 2 is expected [74]. To further characterize the properties of the observed flux noise, we fit a theory model based on an Ornstein-Uhlenbeck process to the  $\Gamma_\phi(\omega_{\text{qb}})$ . The model assumes the

autocorrelation function for random flux fluctuations to be  $\langle \delta\Phi(0)\delta\Phi(\tau) \rangle = \sigma^2 e^{-\kappa|\tau|}$  [see Eq. (2.130)]. It smoothly interpolates between its limiting cases of white noise and low-frequency correlated, colored Gaussian noise (see Sec.2.5.3). The latter is similar to the ubiquitous  $1/f$ -noise. From the fit we extract  $\sigma = (79 \pm 9) \mu\Phi_0$  with  $\Phi_0$  being the flux quantum. We further find that  $\kappa/(2\pi)$  vanishes within a statistical uncertainty of 52 kHz. Hence, this noise speed is negligible with respect to the noise strength  $|\partial\omega_{\text{qb}}/\partial\Phi|(\sigma/2\pi)$ , which is on the order of a few megahertz. We conclude that the noise in our device is well described by colored Gaussian noise in the quasi-static limit. This is also consistent with our previous assessment based on  $\eta \neq 2$  and with a noise spectrum diverging at  $\omega \rightarrow 0$ . A possible source for such noise can, e.g., be TLS ensembles produced by surface defects in dielectric materials [77, 78]. We can directly relate the quantity  $\sigma$  to the strength of the  $1/f$ -noise typically produced by such ensembles [42, 74–76]. The standard treatment [42] provides us with an upper bound of approximately  $100 \mu\Phi_0$ , which is well compatible with the values on the order of a few  $\mu\Phi_0$  found in many other works [42, 74, 79, 80].

# Chapter 5

## Summary and outlook

In this thesis, we have characterized the properties of the broadband on-chip environment of a superconducting transmon qubit via spectrally resolved transmission measurements. The environment is formed by a Mach-Zehnder-type onchip interferometer. To this end, we have developed a theoretical description of the designed sample and have performed a comprehensive analysis of the decoherence properties of the qubit over a broad frequency range.

We have used a transfer matrix description of our circuitry. To construct the transfer matrix, we have built on lumped element circuit theory for superconducting microwave circuits. We have extended the theory to support quasi 1D circuits and adapted it to take into account the quantum nature of Josephson junctions of the transmon qubit.

All measurements have been conducted at cryogenic temperatures of 40 mK. During this thesis, the measurement apparatuses have been improved, completed and modified to carry out and optimize our measurements. To improve the quality of the measurements, we have changed the experimental setup with respect to the parts holding the sample and connecting it to the measurement apparatus:

- We have designed and fabricated a new sample holder for better shielding against parasitic microwave radiation.
- We have improved the chip packaging via PCBs to overcome geometrical limitations.
- We have eliminated unreliable connections between PCB and sample chip.

Furthermore, the fundamental microwave components defining the on-chip environment of the qubit, such as microwave beam splitters and Mach-Zehnder-type

microwave interferometers, have been designed, simulated and fabricated. Based on simulation and measurement of these components, we have developed an optimized chip layout of a microwave interferometer with the transmon qubit in one of its arms. Finally, transmission measurements have been performed. Here, the transmon qubit has been used as a probe by tuning its working frequency over a broad range. Fitting the transfer matrix model to the data obtained in transmission measurements, we extract the relaxation rates  $\Gamma_1$  and the pure dephasing rates  $\Gamma_\Phi$  of the qubit at the different working points.

The functional dependence of the relaxation rate on the frequency of the qubit allows for an assessment of the nature of the qubit environment at high frequencies, while the functional dependence of the pure dephasing rate allows to conclude on the properties of the noise at low frequencies. In the frequency range of 4 – 7 GHz, the relaxation rate increases linearly with the qubit frequency. This finding confirms our expectation that the transmission line acts as an Ohmic bath. We have further analyzed the qubit dephasing using a model based on the Ornstein-Uhlenbeck process. We find that our circuit QED open quantum system is dominated by slow, colored Gaussian noise. The sources for such noise cannot be explained by the circuit design. They are most likely caused by the used materials and fabrication processes.

There are several opportunities to follow up on what has been done in this thesis. Here, we want to focus on two application-oriented approaches:

## Transmon qubit as spectrometer

Using a qubit as a spectrometer could help to test microwave designs developed for general quantum technologies in a broad range of applications from sensing, over communications to quantum computing. E.g., in the sample investigated in this thesis, an unexpected resonance was obtained from the  $\Gamma_1$  behavior at frequencies near 8.5 GHz. It provides a hint to the presence of an unintended on-chip mode coupling to the qubit, which, in a first-order approximation, was modeled by an additional Lorentzian.

## Quantum computing platform

Our work can also serve as a novel platform for quantum computing. Using the techniques and designs of the microwave interferometer described in this thesis, one can implement the ideas stated in all optical quantum computing (AOQC, [81]) in the microwave regime with superconducting circuits. Such an approach could

overcome the biggest challenge in optical quantum computing, namely the lack of a strongly nonlinear element. The concept of dual-rail encoding can be realized with microwave photons instead of visible light. Then, the design realized within this thesis is perfectly suited to implement a c-phase gate (see Fig. 5.1). A crucial property here is that the phase induced by the qubits placed in the interferometer arms has to depend on the photon number in a nonlinear fashion.

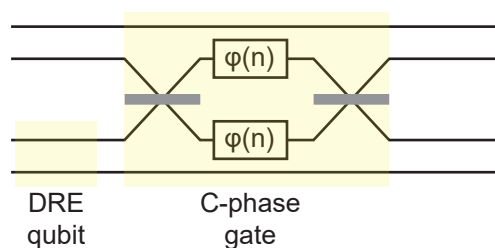


Figure 5.1: Sketch of a possible C-phase gate implementation for quantum computing with propagating microwaves in the spirit of all-optical quantum computing. Black lines indicate waveguides, gray boxes beam splitters and black boxes with  $\varphi(n)$  inside represent phase shifters. One dual-rail encoded (DRE) qubit and the gate are highlighted by yellow boxes.



# Bibliography

- [1] Jonathan P. Dowling and Gerard J. Milburn. “Quantum technology: the second quantum revolution”. In: *Philosophical Transactions of the Royal Society of London. Series A: Mathematical, Physical and Engineering Sciences* 361.1809 (2003). Ed. by A. G. J. MacFarlane, pp. 1655–1674. DOI: [10.1098/rsta.2003.1227](https://doi.org/10.1098/rsta.2003.1227).
- [2] E. P. Menzel et al. “Path Entanglement of Continuous-Variable Quantum Microwaves”. In: *Physical Review Letters* 109.25 (2012). DOI: [10.1103/physrevlett.109.250502](https://doi.org/10.1103/physrevlett.109.250502).
- [3] Kirill G. Fedorov et al. “Displacement of Propagating Squeezed Microwave States”. In: *Physical Review Letters* 117.2 (2016). DOI: [10.1103/physrevlett.117.020502](https://doi.org/10.1103/physrevlett.117.020502).
- [4] C. Eichler et al. “Observation of Two-Mode Squeezing in the Microwave Frequency Domain”. In: *Phys. Rev. Lett.* 107 (2011), p. 113601.
- [5] E. Flurin et al. “Generating Entangled Microwave Radiation Over Two Transmission Lines”. In: *Physical Review Letters* 109.18 (2012). DOI: [10.1103/physrevlett.109.183901](https://doi.org/10.1103/physrevlett.109.183901).
- [6] C. M. Wilson et al. “Observation of the dynamical Casimir effect in a superconducting circuit”. In: *Nature* 479.7373 (2011), pp. 376–379. DOI: [10.1038/nature10561](https://doi.org/10.1038/nature10561).
- [7] J. Goetz et al. “Photon Statistics of Propagating Thermal Microwaves”. In: *Physical Review Letters* 118.10 (2017). DOI: [10.1103/physrevlett.118.103602](https://doi.org/10.1103/physrevlett.118.103602).
- [8] D. Bozyigit et al. “Antibunching of microwave-frequency photons observed in correlation measurements using linear detectors”. In: *Nature Physics* 7.2 (2010), pp. 154–158. DOI: [10.1038/nphys1845](https://doi.org/10.1038/nphys1845).

- 
- [9] O. Astafiev et al. “Resonance Fluorescence of a Single Artificial Atom”. In: *Science* 327.5967 (2010), pp. 840–843. DOI: [10.1126/science.1181918](https://doi.org/10.1126/science.1181918).
- [10] C. Lang et al. “Correlations, indistinguishability and entanglement in Hong–Ou–Mandel experiments at microwave frequencies”. In: *Nature Physics* 9.6 (2013), pp. 345–348. DOI: [10.1038/nphys2612](https://doi.org/10.1038/nphys2612).
- [11] Io-Chun Hoi et al. “Demonstration of a Single-Photon Router in the Microwave Regime”. In: *Physical Review Letters* 107.7 (7 2011), p. 073601. DOI: [10.1103/physrevlett.107.073601](https://doi.org/10.1103/physrevlett.107.073601).
- [12] Io-Chun Hoi et al. “Giant Cross–Kerr Effect for Propagating Microwaves Induced by an Artificial Atom”. In: *Physical Review Letters* 111.5 (2013). DOI: [10.1103/physrevlett.111.053601](https://doi.org/10.1103/physrevlett.111.053601).
- [13] Lan Zhou et al. “Controllable Scattering of a Single Photon inside a One-Dimensional Resonator Waveguide”. In: *Physical Review Letters* 101.10 (2008). DOI: [10.1103/physrevlett.101.100501](https://doi.org/10.1103/physrevlett.101.100501).
- [14] Jing Lu et al. “Single-photon router: Coherent control of multichannel scattering for single photons with quantum interferences”. In: *Physical Review A* 89.1 (2014). DOI: [10.1103/physreva.89.013805](https://doi.org/10.1103/physreva.89.013805).
- [15] Bixuan Fan, Gerard J. Milburn, and Thomas M. Stace. “Microwave Quantum Photonics”. In: *Quantum Science and Technology*. Springer International Publishing, 2016, pp. 139–162. DOI: [10.1007/978-3-319-24091-6\\_6](https://doi.org/10.1007/978-3-319-24091-6_6).
- [16] A. J. Leggett et al. “Dynamics of the dissipative two-state system”. In: *Rev. Mod. Phys.* 59.1 (1 1987), pp. 1–85. DOI: [10.1103/RevModPhys.59.1](https://doi.org/10.1103/RevModPhys.59.1).
- [17] Max Haeberlein et al. “Spin-boson model with an engineered reservoir in circuit quantum electrodynamics”. In: <http://arxiv.org/abs/1506.09114> (2015). DOI: [http://arxiv.org/abs/1506.09114](https://doi.org/http://arxiv.org/abs/1506.09114). URL: <http://arxiv.org/abs/1506.09114>.
- [18] M.H. Devoret, Steven Girvin, and Robert Schoelkopf. “Circuit-QED: How strong can the coupling between a Josephson junction atom and a transmission line resonator be?” In: *Annalen der Physik* 16.10-11 (2007), pp. 767–779. DOI: [10.1002/andp.200710261](https://doi.org/10.1002/andp.200710261).
- [19] John Clarke and Frank K. Wilhelm. “Superconducting quantum bits”. In: *Nature* 453.7198 (2008), pp. 1031–1042. DOI: [10.1038/nature07128](https://doi.org/10.1038/nature07128).

- [20] Frank Arute et al. “Quantum supremacy using a programmable superconducting processor”. In: *Nature* 574.7779 (2019), pp. 505–510. DOI: [10.1038/s41586-019-1666-5](https://doi.org/10.1038/s41586-019-1666-5).
- [21] C.L. Degen, F. Reinhard, and P. Cappellaro. “Quantum sensing”. In: *Reviews of Modern Physics* 89.3 (2017). DOI: [10.1103/revmodphys.89.035002](https://doi.org/10.1103/revmodphys.89.035002).
- [22] Bahaa E. A. Saleh and Malvin Carl Teich. *Fundamentals of Photonics*. 2nd ed. John Wiley & Sons, Inc., 2007. DOI: [10.1002/0471213748](https://doi.org/10.1002/0471213748).
- [23] D. M. Pozar. *Microwave Engineering*. John Wiley & Sons Inc., New York, 2005.
- [24] E.W. Matthews. “The Use of Scattering Matrices in Microwave Circuits”. In: *IEEE Transactions on Microwave Theory and Techniques* 3.3 (1955), pp. 21–26. DOI: [10.1109/tmtt.1955.1124941](https://doi.org/10.1109/tmtt.1955.1124941).
- [25] Christian Schneider. “On-chip Superconducting Microwave Beam Splitter”. Master’s thesis. Walther-Meißner-Institut, Dec. 2014.
- [26] Uri Vool and Michel H. Devoret. “Introduction to Quantum Electromagnetic Circuits”. In: (Oct. 11, 2016). DOI: [10.1002/cta.2359](https://doi.org/10.1002/cta.2359). arXiv: <http://arxiv.org/abs/1610.03438v2> [quant-ph].
- [27] Mauro Parodi and Marco Storace. *Linear and Nonlinear Circuits: Basic & Advanced Concepts*. Springer International Publishing, 2018. DOI: [10.1007/978-3-319-61234-8](https://doi.org/10.1007/978-3-319-61234-8).
- [28] M. H. Devoret, A. Wallraff, and J. M. Martinis. “Superconducting Qubits: A Short Review”. In: (Nov. 7, 2004). arXiv: <http://arxiv.org/abs/cond-mat/0411174v1> [cond-mat.mes-hall].
- [29] Todd Satogata. *Todd Satogata. Lecture notes*. 2013. URL: <http://www.toddsatogata.net/2013-USPAS/ResonantDrivenOscillator.pdf>.
- [30] Philipp Kurpiers et al. “Characterizing the attenuation of coaxial and rectangular microwave-frequency waveguides at cryogenic temperatures”. In: *EPJ Quantum Technology* 4.1 (2017). DOI: [10.1140/epjqt/s40507-017-0059-7](https://doi.org/10.1140/epjqt/s40507-017-0059-7).
- [31] A. Wallraff et al. “Strong coupling of a single photon to a superconducting qubit using circuit quantum electrodynamics”. In: *Nature* 431 (2004), p. 162.
- [32] M. Göppl et al. “Coplanar waveguide resonators for circuit quantum electrodynamics”. In: *Journal of Applied Physics* 104.11 (Dec. 2008), p. 113904. DOI: [10.1063/1.3010859](https://doi.org/10.1063/1.3010859). arXiv: [0807.4094](https://arxiv.org/abs/0807.4094).

- [33] C. R. H. McRae et al. “Dielectric loss extraction for superconducting microwave resonators”. In: (Sept. 16, 2019). arXiv: <http://arxiv.org/abs/1909.07428v1> [quant-ph].
- [34] Wayne Woods et al. “Determining interface dielectric losses in superconducting coplanar waveguide resonators”. In: *Phys. Rev. Applied* 12, 014012 (2019) (Aug. 30, 2018). DOI: [10.1103/PhysRevApplied.12.014012](https://doi.org/10.1103/PhysRevApplied.12.014012). arXiv: <http://arxiv.org/abs/1808.10347v1> [quant-ph].
- [35] J. Reed and G.J. Wheeler. “A Method of Analysis of Symmetrical Four-Port Networks”. In: *IEEE Transactions on Microwave Theory and Techniques* 4.4 (1956), pp. 246–252. DOI: [10.1109/tmtt.1956.1125071](https://doi.org/10.1109/tmtt.1956.1125071).
- [36] Ludwig Zehnder. “Ein neuer Interferenzrefraktor”. In: *Zeitschrift für Instrumentenkunde* 11 (1891), pp. 275–285.
- [37] Michel H. Devoret. “Quantum Fluctuations in Electrical Circuits”. In: 1995, pp. 351–386.
- [38] J. J. García-Ripoll. “Lecture notes on superconducting quantum circuits”. Oct. 1, 2014.
- [39] David J. Griffiths. *Introduction to Quantum Mechanics (2nd Edition)*. Pearson Prentice Hall, 2004. ISBN: 0131118927.
- [40] Io-Chun Hoi. *Quantum Optics with Propagating Microwaves in Superconducting Circuits*. Department of Microtechnology and Nanoscience, Chalmers University of Technology, 2013. ISBN: 978-91-7385-878-6.
- [41] Will Oliver. *Quantum Information Processing: Lecture Notes of the 44th IFF Spring School 2013*. Ed. by David P. DiVincenzo. 2013. ISBN: 978-3893368334.
- [42] G. Ithier et al. “Decoherence in a superconducting quantum bit circuit”. In: *Physical Review B* 72.13 (13 2005), p. 134519. DOI: [10.1103/physrevb.72.134519](https://doi.org/10.1103/physrevb.72.134519).
- [43] “Festkörperphysik. Von Rudolf Gross und Achim Marx”. In: *Physik in unserer Zeit* 44.4 (2013), pp. 204–204. DOI: [10.1002/piuz.201390075](https://doi.org/10.1002/piuz.201390075).
- [44] B. D. Josephson. “Possible new effects in superconductive tunnelling”. In: *Physics Letters* 1 (1962), pp. 251–253. ISSN: 0031-9163. DOI: [DOI: 10.1016/0031-9163\(62\)91369-0](https://doi.org/10.1016/0031-9163(62)91369-0).
- [45] Jens Koch et al. “Charge-insensitive qubit design derived from the Cooper pair box”. In: *Physical Review A* 76.4 (4 2007), p. 042319. DOI: [10.1103/physreva.76.042319](https://doi.org/10.1103/physreva.76.042319).

- [46] J. A. Schreier et al. “Suppressing charge noise decoherence in superconducting charge qubits”. In: *Physical Review B* 77.18 (2008). DOI: [10.1103/physrevb.77.180502](https://doi.org/10.1103/physrevb.77.180502).
- [47] Hamel. “Georg Duffing, Ingenieur: Erzwungene Schwingungen bei veränderlicher Eigenfrequenz und ihre technische Bedeutung. Sammlung Vieweg. Heft 41/42, Braunschweig 1918. VI134 S”. In: *ZAMM - Journal of Applied Mathematics and Mechanics / Zeitschrift für Angewandte Mathematik und Mechanik* 1.1 (1921), pp. 72–73. DOI: [10.1002/zamm.19210010109](https://doi.org/10.1002/zamm.19210010109).
- [48] John M. Martinis, Michel H. Devoret, and John Clarke. “Energy-Level Quantization in the Zero-Voltage State of a Current-Biased Josephson Junction”. In: *Physical Review Letters* 55.15 (1985), pp. 1543–1546. DOI: [10.1103/physrevlett.55.1543](https://doi.org/10.1103/physrevlett.55.1543).
- [49] Javier Puertas Martínez. “Circuit quantum electrodynamics with transmon qubits”. Master’s thesis. Walther-Meißner-Institut, Feb. 2015.
- [50] Miriam Muetting. “Time domain characterization of a transmon Qubit”. Master’s Thesis. Walther-Meißner-Institut, Feb. 2015.
- [51] Jan Goetz. “The interplay of Superconducting Quantum Circuits and Propagating Microwave States”. Ph.D. thesis. Walther-Meißner-Institut, 2016.
- [52] D. F. Walls and G. J. Milburn. *Quantum Optics*. English. Springer, Berlin, 2008.
- [53] E.T. Jaynes and F.W. Cummings. “Comparison of quantum and semiclassical radiation theories with application to the beam maser”. In: *Proceedings of the IEEE* 51.1 (1963), pp. 89–109. DOI: [10.1109/proc.1963.1664](https://doi.org/10.1109/proc.1963.1664).
- [54] M. Brune et al. “From Lamb shift to light shifts: Vacuum and subphoton cavity fields measured by atomic phase sensitive detection”. In: *Physical Review Letters* 72.21 (1994), pp. 3339–3342. DOI: [10.1103/physrevlett.72.3339](https://doi.org/10.1103/physrevlett.72.3339).
- [55] B. Peropadre et al. “Scattering of coherent states on a single artificial atom”. In: *New Journal of Physics* 15.3 (2013), p. 035009. DOI: [10.1088/1367-2630/15/3/035009](https://doi.org/10.1088/1367-2630/15/3/035009).
- [56] P Eder et al. “Quantum probe of an on-chip broadband interferometer for quantum microwave photonics”. In: *Superconductor Science and Technology* 31.11 (2018), p. 115002. DOI: [10.1088/1361-6668/aad8f4](https://doi.org/10.1088/1361-6668/aad8f4).

- [57] David P. DiVincenzo. “The Physical Implementation of Quantum Computation”. In: *Fortschritte der Physik* 48.9-11 (2000), pp. 771–783. DOI: [10.1002/1521-3978\(200009\)48:9/11<771::aid-prop771>3.0.co;2-e](https://doi.org/10.1002/1521-3978(200009)48:9/11<771::aid-prop771>3.0.co;2-e).
- [58] Grégoire Ithier. “Manipulation, readout and analysis of the decoherence of a superconducting quantum bit”. Ph.D. thesis. Université Pierre et Marie Curie - Paris VI, Dec. 2005. URL: <https://tel.archives-ouvertes.fr/tel-00130589>.
- [59] N.G. Van Kampen. *Stochastic Processes in Physics and Chemistry*. Ed. by N.G. VAN KAMPEN. Third Edition. North-Holland Personal Library. Amsterdam: Elsevier, 2003, pp. x –.
- [60] C.W. Gardiner. *Handbook of Stochastic Methods*. 1997.
- [61] G. J. Dolan. “Offset masks for lift-off photoprocessing”. In: *Applied Physics Letters* 31.5 (1977), pp. 337–339. DOI: [10.1063/1.89690](https://doi.org/10.1063/1.89690).
- [62] Henri Jansen et al. “A survey on the reactive ion etching of silicon in microtechnology”. In: *Journal of Micromechanics and Microengineering* 6.1 (1996), pp. 14–28. DOI: [10.1088/0960-1317/6/1/002](https://doi.org/10.1088/0960-1317/6/1/002).
- [63] Thomas Niemczyk. “From strong to ultrastrong coupling in circuit QED architectures”. Ph.D. thesis. Walther-Meißner-Institut, June 30, 2011.
- [64] Friedrich Wulschner. “Controlled interactions in superconducting quantum circuits”. Ph.D. thesis. Walther Meißner Institut, 2016.
- [65] E. P. Menzel et al. “Dual-Path State Reconstruction Scheme for Propagating Quantum Microwaves and Detector Noise Tomography”. In: *Phys. Rev. Lett.* 105 (Jan. 2010), p. 100401.
- [66] Ferdinand Loacker. “Design and characterization of a superconducting beam-splitter for quantum information processing”. Master’s thesis. Walther-Meißner-Institut, Dec. 2013.
- [67] H.-S. Ku et al. “Design and Testing of Superconducting Microwave Passive Components for Quantum Information Processing”. In: *IEEE Transactions on Applied Superconductivity* 21 (2011), pp. 452 –455. ISSN: 1051-8223. DOI: [10.1109/TASC.2010.2089403](https://doi.org/10.1109/TASC.2010.2089403).
- [68] Michael Fischer. “On-chip Superconducting Microwave Interferometer”. Master’s thesis. Walther-Meißner-Institut, Dec. 2014.

- [69] M. Baur et al. “Measurement of Autler-Townes and Mollow transitions in a strongly driven superconducting qubit”. In: *Phys. Rev. Lett.* 102, 243602 (2009) 102.24 (Dec. 23, 2008). DOI: [10.1103/PhysRevLett.102.243602](https://doi.org/10.1103/PhysRevLett.102.243602).
- [70] S. H. Autler and C. H. Townes. “Stark Effect in Rapidly Varying Fields”. In: *Physical Review* 100.2 (1955), pp. 703–722. DOI: [10.1103/physrev.100.703](https://doi.org/10.1103/physrev.100.703).
- [71] U. Fano. “Effects of Configuration Interaction on Intensities and Phase Shifts”. In: *Phys. Rev.* 124 (6 1961), pp. 1866–1878. DOI: [10.1103/PhysRev.124.1866](https://doi.org/10.1103/PhysRev.124.1866).
- [72] A. Perot and Charles Fabry. “On the Application of Interference Phenomena to the Solution of Various Problems of Spectroscopy and Metrology”. In: *The Astrophysical Journal* 9 (1899), p. 87. DOI: [10.1086/140557](https://doi.org/10.1086/140557).
- [73] M. Born and W. Wolf. *Principles of Optics*. 4th. Pergamon Press, 1970. URL: <https://archive.org/details/PrinciplesOfOptics>.
- [74] F. Deppe et al. “Phase coherent dynamics of a superconducting flux qubit with capacitive bias readout”. In: *Physical Review B* 76.21 (21 2007), p. 214503. DOI: [10.1103/physrevb.76.214503](https://doi.org/10.1103/physrevb.76.214503).
- [75] F. Yoshihara et al. “Decoherence of Flux Qubits due to  $1/f$  Flux Noise”. In: *Physical Review Letters* 97.16 (16 2006), p. 167001. DOI: [10.1103/physrevlett.97.167001](https://doi.org/10.1103/physrevlett.97.167001).
- [76] K. Kakuyanagi et al. “Dephasing of a Superconducting Flux Qubit”. In: *Physical Review Letters* 98.4 (4 2007), p. 047004. DOI: [10.1103/physrevlett.98.047004](https://doi.org/10.1103/physrevlett.98.047004).
- [77] P. Dutta and P. M. Horn. “Low-frequency fluctuations in solids:  $1/f$  noise”. In: *Reviews of Modern Physics* 53.3 (3 1981), pp. 497–516. DOI: [10.1103/revmodphys.53.497](https://doi.org/10.1103/revmodphys.53.497).
- [78] P. J. J. O’Malley et al. “Qubit Metrology of Ultralow Phase Noise Using Randomized Benchmarking”. In: *Physical Review Applied* 3.4 (2015). DOI: [10.1103/physrevapplied.3.044009](https://doi.org/10.1103/physrevapplied.3.044009).
- [79] D. J. Van Harlingen et al. “Decoherence in Josephson-junction qubits due to critical-current fluctuations”. In: *Physical Review B* 70.6 (2004). DOI: [10.1103/physrevb.70.064517](https://doi.org/10.1103/physrevb.70.064517).
- [80] Frank Deppe. “Superconducting flux quantum circuits: Characterization, quantum coherence, and controlled symmetry breaking”. Ph.D. thesis. Technische Universität München, 2009.

- [81] Pieter Kok et al. “Linear optical quantum computing with photonic qubits”. In: *Reviews of Modern Physics* 79.1 (1 2007), pp. 135–174. DOI: [10.1103/revmodphys.79.135](https://doi.org/10.1103/revmodphys.79.135).
- [82] A. T. A. M. de Waele. “Basic Operation of Cryocoolers and Related Thermal Machines”. In: *Journal of Low Temperature Physics* 164.5-6 (2011), pp. 179–236. DOI: [10.1007/s10909-011-0373-x](https://doi.org/10.1007/s10909-011-0373-x).
- [83] K A Shafi et al. “Pulse Tube refrigerator-an alternative Cryocooler for low temperature applications down to 2.5K”. In: *Frontiers in Automobile and Mechanical Engineering -2010*. IEEE, 2010, pp. 184–188. DOI: [10.1109/fame.2010.5714829](https://doi.org/10.1109/fame.2010.5714829).
- [84] Kurt Uhlig. “Concepts for a low-vibration and cryogen-free tabletop dilution refrigerator”. In: *Cryogenics* 87 (2017), pp. 29–34. DOI: [10.1016/j.cryogenics.2017.08.003](https://doi.org/10.1016/j.cryogenics.2017.08.003).
- [85] Stephan Pogorzalek. “Displacement of Squeezed Propagating Microwave States”. Master’s thesis. Walther-Meißner-Institut, Oct. 1, 2015.
- [86] D. T. Pegg and S. M. Barnett. “Phase properties of the quantized single-mode electromagnetic field”. In: *Physical Review A* 39.4 (1989), pp. 1665–1675. DOI: [10.1103/physreva.39.1665](https://doi.org/10.1103/physreva.39.1665).
- [87] Leonard Susskind and Jonathan Glogower. “Quantum mechanical phase and time operator”. In: *Physics Physique* 1.1 (1964), pp. 49–61. DOI: [10.1103/physicsphysiquefizika.1.49](https://doi.org/10.1103/physicsphysiquefizika.1.49).
- [88] C. VEYRES and V. FOUAD HANNA. “Extension of the application of conformal mapping techniques to coplanar lines with finite dimensions”. In: *International Journal of Electronics* 48.1 (1980), pp. 47–56. DOI: [10.1080/00207218008901066](https://doi.org/10.1080/00207218008901066).
- [89] G. Ghione and C. Naldi. “Analytical formulas for coplanar lines in hybrid and monolithic MICs”. In: *Electronics Letters* 20.4 (1984), p. 179. DOI: [10.1049/el:19840120](https://doi.org/10.1049/el:19840120).

# List of publications

## Publications related to this thesis

1. Michael Fischer, Qi-Ming Chen, Christian Besson, **Peter Eder**, Jan Goetz, Stefan Pogorzalek, Michael Renger, Edwar Xie, Michael J. Hartmann, Kirill G. Fedorov, Achim Marx, Frank Deppe, Rudolf Gross, "In-situ tunable non-linearity and competing signal paths in coupled superconducting resonators", [arXiv:2009.13492](https://arxiv.org/abs/2009.13492), submitted for publication (2020)
2. **P. Eder**, T. Ramos, J. Goetz, M. Fischer, S. Pogorzalek, J. Puertas Martínez, E.P. Menzel, F. Loacker, E. Xie, J.J. Garcia-Ripoll, K.G. Fedorov, A. Marx, F. Deppe, R. Gross, "Quantum probe of an on-chip broadband interferometer for quantum microwave photonics", [Supercond. Sci. Technol. 31 , 115002](#) (2018)
3. Edwar Xie, Frank Deppe, Michael Renger, Daniel Repp, **Peter Eder**, Michael Fischer, Jan Goetz, Stefan Pogorzalek, Kirill G. Fedorov, Achim Marx, and Rudolf Gross, "Compact 3D quantum memory", [Appl. Phys. Lett. 112 , 202601](#) (2018)
4. Jan Goetz, Frank Deppe, Kirill G. Fedorov, **Peter Eder**, Michael Fischer, Stefan Pogorzalek, Edwar Xie, Achim Marx, Rudolf Gross, "Parity-engineered light-matter interaction", [Phys. Rev. Lett. 121 , 060503](#) (2018)
5. Kirill G. Fedorov, S. Pogorzalek, U. Las Heras, M. Sanz, P. Yard, **P. Eder**, M. Fischer, J. Goetz, E. Xie, K. Inomata, Y. Nakamura, R. Di Candia, E. Solano, A. Marx, F. Deppe, R. Gross, "Finite-time quantum entanglement in propagating squeezed microwaves", [Scientific Reports 8 , 6416](#) (2018)
6. Stefan Pogorzalek, Kirill G. Fedorov, Ling Zhong, Jan Goetz, Friedrich Wulschner, Michael Fischer, **Peter Eder**, Edwar Xie, Kunihiro Inomata, Tsuyoshi Yamamoto, Yasunobu Nakamura, Achim Marx, Frank Deppe, Rudolf Gross,

- "Hysteretic Flux Response and Nondegenerate Gain of Flux-Driven Josephson Parametric Amplifiers", [Phys. Rev. Applied 8 , 024012](#) (2017)
7. J. Goetz, S. Pogorzalek, F. Deppe, K. G. Fedorov, **P. Eder**, M. Fischer, F. Wulschner, E. Xie, A. Marx, R. Gross, "Photon Statistics of Propagating Thermal Microwaves", [Phys. Rev. Lett. 118 , 103602](#) (2017)
  8. J. Goetz, F. Deppe, **P. Eder**, M. Fischer, M. Müting, J. P. Martínez, S. Pogorzalek, F. Wulschner, E. Xie, K. G. Fedorov, A. Marx, R. Gross, "Second-order decoherence mechanisms of a transmon qubit probed with thermal microwave states ", [Quantum Sci. Technol. 2 , 025002](#) (2017)
  9. F. Wulschner, J. Goetz, F. R. Koessel, E. Hoffmann, A. Baust, **P. Eder**, M. Fischer, M. Haeberlein, M. J. Schwarz, M. Pernpeintner, E. Xie, L. Zhong, C. W. Zollitsch, B. Peropadre, J.-J. Garcia Ripoll, E. Solano, K. Fedorov, E. P. Menzel, F. Deppe, A. Marx, R. Gross, "Tunable coupling of transmission-line microwave resonators mediated by an rf SQUID", [EPJ Quantum Technology 3 , 10](#) (2016)
  10. Max Haeberlein, Frank Deppe, Andreas Kurcz, Jan Goetz, Alexander Baust, **Peter Eder**, Kirill Fedorov, Michael Fischer, Edwin P. Menzel, Manuel J. Schwarz, Friedrich Wulschner, Edwar Xie, Ling Zhong, Enrique Solano, Achim Marx, Juan-José García-Ripoll, Rudolf Gross, "Spin-boson model with an engineered reservoir in circuit quantum electrodynamics", [arXiv:1506.09114](#) , submitted for publication (2015)
  11. Kirill G. Fedorov, L. Zhong, S. Pogorzalek, **P. Eder**, M. Fischer, J. Goetz, E. Xie, F. Wulschner, K. Inomata, T. Yamamoto, Y. Nakamura, R. Di Candia, U. Las Heras, M. Sanz, E. Solano, E. P. Menzel, F. Deppe, A. Marx, R. Gross, "Displacement of propagating squeezed microwave states", [Phys. Rev. Lett. 117 , 020502](#) (2016)
  12. A. Baust, E. Hoffmann, M. Haeberlein, M. J. Schwarz, **P. Eder**, J. Goetz, F. Wulschner, E. Xie, L. Zhong, F. Quijandria, D. Zueco, J.-J. Garcia Ripoll, L. Garcia-Alvarez, G. Romero, E. Solano, K. G. Fedorov, E. P. Menzel, F. Deppe, A. Marx, R. Gross, "Ultrastrong coupling in two-resonator circuit QED", [Phys. Rev. B 93 , 214501](#) (2016)
  13. J. Goetz, F. Deppe, M. Haeberlein, F. Wulschner, C. W. Zollitsch, S. Meier, M. Fischer, **P. Eder**, E. Xie, K. G. Fedorov, E. P. Menzel, A. Marx, and R.

- Gross, "Loss mechanisms in superconducting thin film microwave resonators", [J. Appl. Phys. 119 , 015304](#) (2016)
14. A. Baust, E. Hoffmann, M. Haeberlein, M. J. Schwarz, **P. Eder**, E. P. Menzel, K. Fedorov, J. Goetz, F. Wulschner, E. Xie, L. Zhong, F. Quijandria, B. Peropadre, D. Zueco, J.-J. Garcia, "Tunable and Switchable Coupling Between Two Superconducting Resonators", [Phys. Rev. B 91 , 014515](#) (2015)
  15. L. Zhong, E. P. Menzel, R. Di Candia, **P. Eder**, M. Ihmig, A. Baust, M. Haeberlein, E. Hoffmann, K. Inomata, T. Yamamoto, Y. Nakamura, E. Solano, F. Deppe, A. Marx, R. Gross, "Squeezing with a flux-driven Josephson parametric amplifier", [New. J. Phys. 15 , 125013](#) (2013)

**Considerable contributions to the following student work has been given during doing this PhD-thesis**

1. **F. Loacker**, Diploma thesis, 2013
2. **Ch. Schneider**, Master thesis, 2014
3. **M. Fischer**, Master thesis, 2014



# Superconductor Science and Technology

**This is to certify that the article**

Quantum probe of an on-chip broadband interferometer  
for quantum microwave photonics

**P Eder, T Ramos, J Goetz, M Fischer, S Pogorzalek,  
J Puertas Martínez, E P Menzel, F Loacker, E Xie, J J Garcia-Ripoll,  
K G Fedorov, A Marx, F Deppe, and R Gross**

has been selected by the Editors of *Superconductor Science and Technology*  
for inclusion in the “Highlights of 2018” collection. Papers are chosen  
on the basis of referee endorsement, novelty and scientific impact.

**Dr Cathy Foley**  
Editor-in-Chief  
*Superconductor Science and Technology*  
[iopscience.org/sust](http://iopscience.org/sust)

**IOP Publishing**

# Acknowledgments

At this point, I want to express my gratitude to everyone who contributed to the success of this work. In particular, I thank

- Prof. Dr. Rudolf Gross for giving me the opportunity to work on a highly attractive topic.
- Dr. Achim Marx and Dr. Frank Deppe for advice and assistance in the lab and for proof-reading this thesis.
- Frank for discussions on interpreting the data which were often the key to a deeper understanding. Frank, your commitment and readiness to help are singular.
- Our collaborators and friends:
  - Roberto Di Candia, Dr. Daniel Ballester, and Prof. Enrique Solano from the University of the Basque Country UPV/EHU, Bilbao, Spain for their excellent theory support. Roberto, I will always remember our long and efficient working sessions on the analysis of the path entanglement.
  - Matthias Ihmig for developing the FPGA logic. Matthias, I enjoyed working with you, not only since you are a profound expert of electrical engineering.
- My former diploma students, Ferdinand Loacker, Christian Schneider, and Michael Fischer, for their excellent scientific work and the very good cooperation. Their commitment and specific skills were the key for the success of many experiments. Michael, I am very happy that you managed to do a Ph.D. at the WMI faster than myself. And it makes me happy that Christian decided to also do a Ph.D. in Innsbruck, Austria, my beloved home country. I wish you the very best for your future, you deserve it!
- Dr. Hans Huebl for fruitful discussions and lending me books.
- The working students, Benno Blaschke, Garlich Fischbeck, Chris Rau, Rolf Ripsam, and Franz Sterr for their help in developing power supplies, motorized phase shifters, measurement software, thermalizing DC lines and battery cabling.

- All members of the qubit group for interesting discussions and the friendly working atmosphere.
- The workshop team, Helmut Thies, Christian Reichlmeier, Julius Klaus, and Georg Nitschke for the high quality of their work and their suggestions to improve designs.
- A special tribute goes to Robert Müller, who left us during creation of my thesis.
- Astrid Habel and Karen Helm-Knapp for gold plating of sample holders and processing printed circuit boards.
- Thomas Brenninger for giving technical advice whenever needed.
- My current and former office colleagues, Fredrik Hocke, Bernhard Muschler, and Edwar Xie for the good working atmosphere and for discussions on physics and other topics.
- Dr. Dietrich Einzel for discussions.
- Dr. Matthias Opel and Dieter Guratzsch for IT support.
- The Helium liquefaction team for continuous supply of Helium and good company.
- Emel Dönertas and Ludwig Ossiander for administrative tasks.
- All members of the WMI for the very good working atmosphere.
- Especially, my mother and grandmother for always supporting me in every respect and for all the memories we share.

# Appendix A

## Details on cryogenic setups

Here, we present the different types of cryostats used within this thesis. Precharacterization experiments are done in helium bath cryostats at 4 K, while experiments involving Josephson junctions are done at millikelvin temperatures in dilution refrigerators.

### A.1 Helium bath cryostat

This type of cryostat provides a base temperature of  $T \simeq 4.2$  K. The DUT is mounted on a stick and directly subjected to a bath of liquid helium. This type of

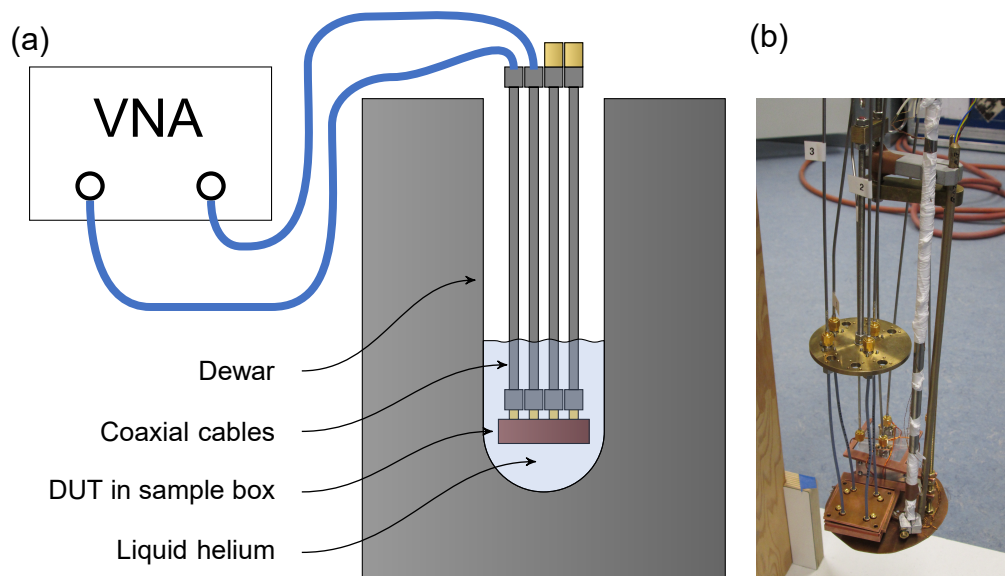


Figure A.1: (a) Setup for measurements in a Helium bath cryostat. (b) Photograph of sample stick with a sample box mounted at the bottom (Pictures with kind permission of Christian Schneider).

cryostat has been used in Refs. [25, 66, 68] to precharacterize the beam splitter and interferometer design.

## A.2 Wet dilution refrigerator

The working principle of a dilution refrigerator is to exploit the tendency of nature to restore the equilibrium of  $^3\text{He}$  concentration in a liquid  $^3\text{He}/^4\text{He}$ -mixture. Such a mixture separates into two phases with different  $^3\text{He}$ -concentrations at temperatures below 870 mK. Pumping on the side of the phase with higher  $^3\text{He}$ -concentration forces  $^3\text{He}$  to diffuse over the phase boundary. This process consumes heat from the environment, giving rise to cooling. Due to a closed-cycle operation, temperatures on the order of 20 mK can be obtained over timescales of weeks or months. Besides this central physical working principle a lot of technical effort has to be taken to implement such devices [51]. Figure A.2 shows a schematic of the dilution refrigerator used in the Circus-Lab at WMI. This specific cryostat relies on  $^4\text{He}$  for precooling. The liquid Helium has to be refilled roughly once a week. This cryostat has been

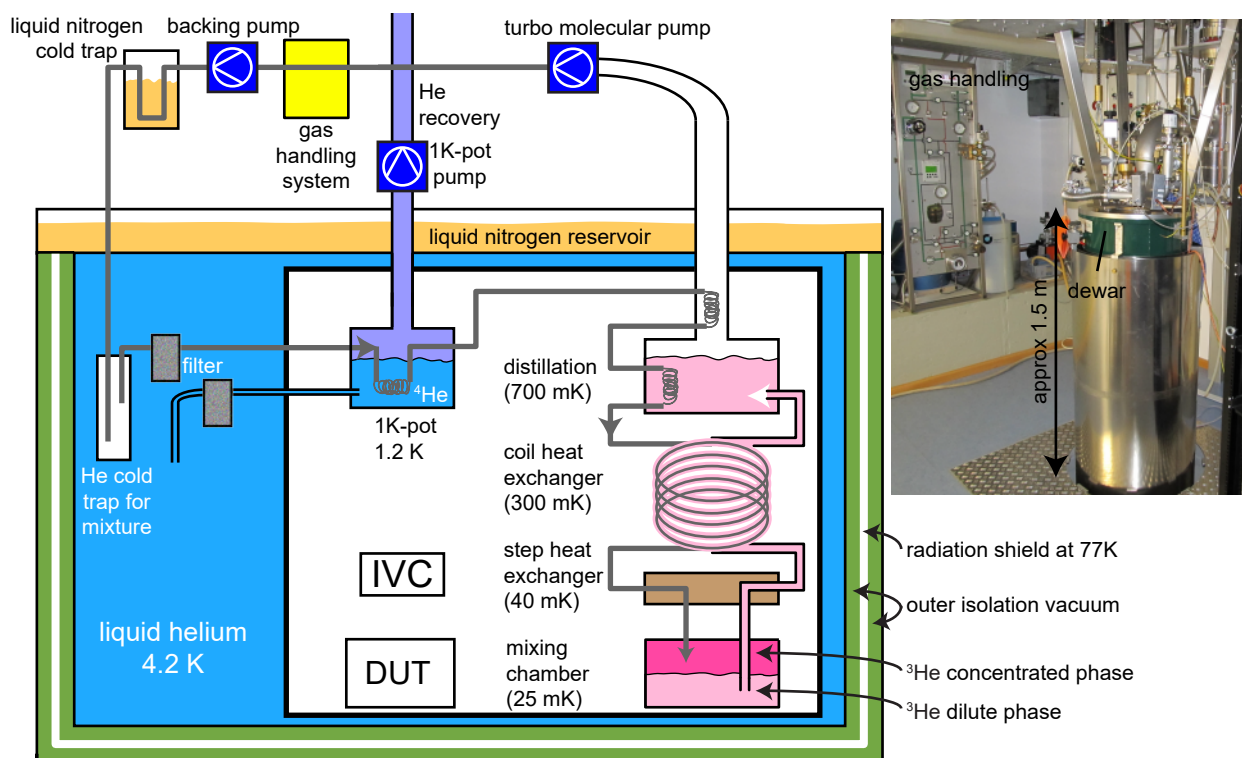


Figure A.2: Schematic overview of a wet dilution refrigerator at WMI (Pictures with kind permission of Jan Goetz).

---

used in Ref. [49] to precharacterize the transmon qubit design in a  $\lambda/4$ -resonator.

### A.3 Dry dilution refrigerator

A dry or cryogen-free  $^3\text{He}/^4\text{He}$  dilution refrigerator does not involve cryoliquids for precooling during operation. The relevant working principle for reaching the base temperature is the same as for all dilution refrigerators, but precooling is done by a pulse tube cryocooler (PTC) [82, 83]. The main advantages are easy handling and low helium consumption. An improved version of a dry dilution refrigerator with a lot of space for experiments has been built at WMI and is used for experiments since 2014 [84, 85]. A photograph of the closed fridge can be found in Fig. A.3. This

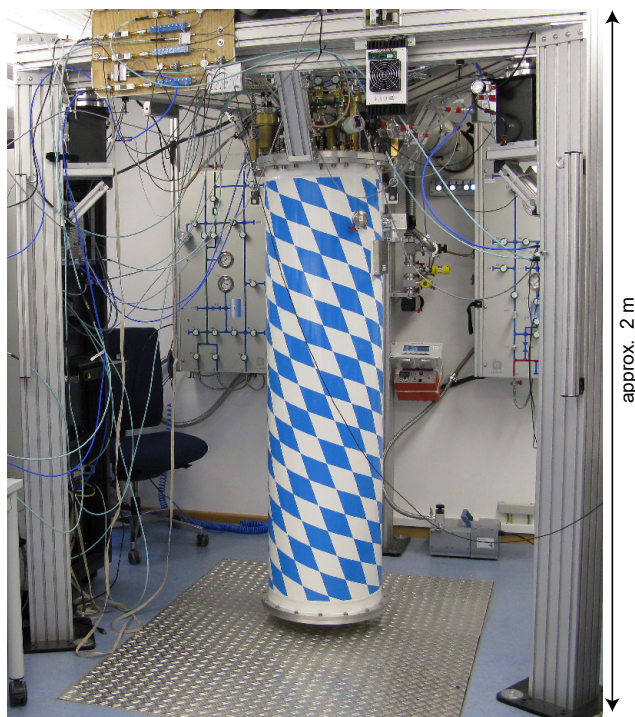


Figure A.3: Photograph of a dry dilution refrigerator at WMI (Used with kind permission by Achim Marx).

cryostat has been used to do the main measurements described in this thesis.

# Appendix B

## Derivation of Hamiltonians

Here, we want to show in detail how to derive the system Hamiltonian for a (quantum) circuit.

### B.1 LC resonator

We start by investigating one of the most basic circuits, a lumped element parallel LC resonator. We will proceed strictly by the recipe presented in Sec. 2.2.

LC resonator				
circuit diagram	descriptive variables	system of equations	Lagrangian Hamiltonian	Operators Commutation

An LC resonator consists of an inductor  $L_r$  and a capacitor  $C_r$  in parallel (see Fig. B.1). In order to allow for a drive, we couple it to a voltage source via a coupling capacitor  $C_g$ .

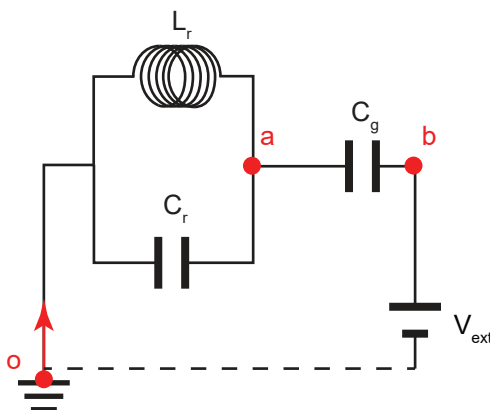


Figure B.1: Equivalent circuit for an LC-resonator.

pling capacitor  $C_g$ . First thing to do is to identify the circuit nodes in the equivalent

circuit and select a root node 0 (usually ground is used for this one).

LC resonator				
circuit diagram	descriptive variables	system of equations	Lagrangian Hamiltonian	Operators Commutation

Now, we define the descriptive node variables as  $\phi_i, Q_i$  for flux and charge at every node  $i$ , and we define descriptive variables for each component. This procedure corresponds to defining descriptive variables for each branch, as each branch contains exactly one component. We decide to use charge  $Q$  and flux  $\Phi$  for the nodes and current  $I$  and voltage  $V$  for components, because it is more intuitive. From a formal point of view, it might be more convenient to express all variables in  $Q$  and  $\Phi$ .

#	descriptive variables	#	start	end	variables
$o$	$\Phi_o = 0, Q_o = 0$	1	0	$a$	$V_1, I_1$
$a$	$\Phi_a, Q_a$	2	0	$a$	$V_2, I_2$
$b$	$\Phi_b, Q_b$	3	$a$	$b$	$V_3, I_3$
		4	$b$	0	$V_4, I_4$

Table B.1: Circuit nodes and branches of circuit shown in Fig. B.1. The symbol "#" stands for node label, which can be  $o, a$  or  $b$  or branch number, which can be 1, 2, 3, or 4.

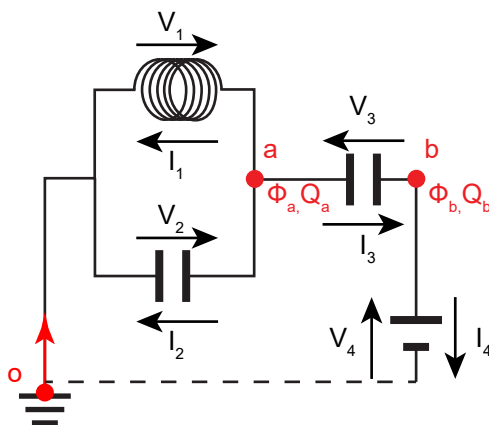


Figure B.2: All nodes in this equivalent circuit are marked in red. Ground is marked with  $o$ , without loss of generality we set  $\Phi_o = 0, Q_o = 0$ .

Figure B.2 shows the labeled circuit diagram. Table B.1 shows the nodes, branches and connected descriptive variables.

LC resonator				
circuit diagram	descriptive variables	system of equations	Lagrangian Hamiltonian	Operators Commutation

In this step, we extract a system of equations describing the circuit using the nodes variables defined above. This takes two sources for relations between the descriptive variables:

- Topology: Use node voltages (KVL) and KCL to make use of the circuit topology.
- Component properties: Use physical properties of components expressed in BCEs.

In Fig. B.2 we can see that the node voltage  $V_a = (\dot{\Phi}_a - \dot{\Phi}_o) = (\dot{\Phi}_a - 0) = \dot{\Phi}_a$  is equal to the voltage  $V_1, V_2$  dropping at branch 1, 2, respectively. The corresponding KVL implies that the voltages in a loop sum up to zero,  $V_1 - V_2 = 0$ . Here, we account for the opposite direction of  $V_1$  and  $V_2$  by multiplication the latter with  $(-1)$ .

To complete the information that can be gained from the circuit topology, we use KCL to investigate the currents in each node. We start with node  $a$  (see Fig. B.3). We see three currents flowing out of this nodes,  $I_1, I_2$ , and  $I_3$ . According to KCL,

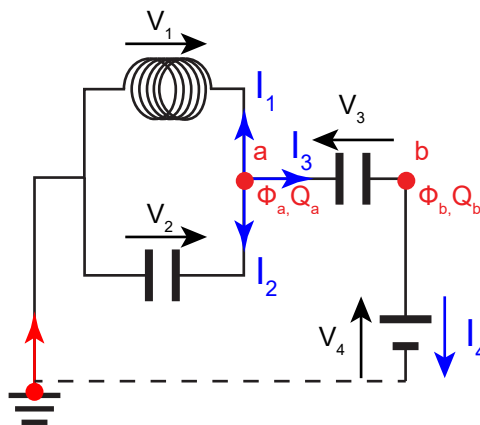


Figure B.3: KCL: The sum of the currents flowing out a node equals the sum of incoming currents ( $I_1 + I_2 + I_3 = 0$ ).

they have to add up to the sum of the incoming currents, which is zero in this case. Finally, we use the branch constitutive equations to exploit the physical properties of the circuit component to obtain the complete system of equations. Based on the

#	branch voltage	#	component	BCE
$a$	$V_a = (\dot{\Phi}_a - \dot{\Phi}_o) = (\dot{\Phi}_a - 0) = \dot{\Phi}_a$	1	Inductor	$I_1 = \frac{\Phi_a}{L_r}$
$a$	$V_a = \dot{\Phi}_a = V_1$	2	Capacitor	$I_2 = C_r \ddot{\Phi}_a$
$a$	$V_a = \dot{\Phi}_a = V_2$	3	Capacitor	$I_3 = C_g (\ddot{\Phi}_b - \ddot{\Phi}_a)$
$b$	$V_b = \dot{\Phi}_b = V_4 = V_{\text{ext}}$	4	V-source	$V_4 = \dot{\Phi}_b = V_{\text{ext}}$

#	KCL
$a$	$I_1 + I_2 + I_3 = 0$
$b$	$I_4 = I_3$

Table B.2: Relations between descriptive variables gained from circuit topology and branch BCEs. The symbol "#" stands for node label, which can be  $a$  or  $b$  or branch number, which can be 1, 2, 3, or 4.

KCL for node  $a$ , we can combine the equations in Tab. B.2 to a single equation:

$$\frac{\Phi_a}{L_r} + C_r \ddot{\Phi}_a = C_g (\dot{V}_{\text{ext}} - \ddot{\Phi}_a). \quad (\text{B.1})$$

By defining  $C_\Sigma = C_r + C_g$  as the total capacitance, we can rearrange Eq. (B.1) to:

$$C_\Sigma \left( \ddot{\Phi}_a - \frac{C_g}{C_\Sigma} \dot{V}_{\text{ext}} \right) = -\frac{\Phi_a}{L_r}. \quad (\text{B.2})$$

LC resonator				
circuit diagram	descriptive variables	system of equations	Lagrangian Hamiltonian	Operators Commutation

Next, we construct the Lagrangian  $\mathcal{L} = T - U$  of the system, contributing the capacitive terms ( $C\dot{\Phi}^2/2$ ) to kinetic energy, and inductive terms ( $\dot{\Phi}^2/(2L)$ ), as well as the voltage source ( $C_g V_{\text{ext}}^2/2$ ), for potential energy.

$$\mathcal{L}(\Phi_a, \dot{\Phi}_a) = \underbrace{\frac{C_r}{2}\dot{\Phi}_a^2 + \frac{C_g}{2}(V_{\text{ext}} - \dot{\Phi}_a)^2}_T - \underbrace{\left(\frac{\Phi_a^2}{2L_r} + \frac{C_g V_{\text{ext}}^2}{2}\right)}_U. \quad (\text{B.3})$$

We use the Euler-Lagrange equation  $\frac{d}{dt} \frac{\partial \mathcal{L}}{\partial \dot{\Phi}_i} = \frac{\partial \mathcal{L}}{\partial \Phi_i}$  to obtain the equations of motion, Eq. (B.2), from  $\mathcal{L}$ , and thus confirm that Eq. (B.3) is a system Lagrangian. Subsequently, we derive the conjugate momenta  $Q_i = (\partial \mathcal{L}) (\partial \dot{\Phi}_i)$ . For the simple resonator circuit, we we have only one momentum with index  $i = a$ :

$$Q_a = \frac{\partial \mathcal{L}}{\partial \dot{\Phi}_a} = (C_r + C_g)\dot{\Phi}_a - C_g V_{\text{ext}} = C_\Sigma \dot{\Phi}_a - C_g V_{\text{ext}} \quad (\text{B.4})$$

Applying the Legendre transformation  $H = Q\dot{\Phi} - \mathcal{L}$ , we get the system Hamiltonian:

$$H(\Phi_a, \dot{\Phi}_a) = Q\dot{\Phi}_a - \mathcal{L} \quad (\text{B.5})$$

$$= \left( (C_r + C_g)\dot{\Phi}_a - C_g V_{\text{ext}} \right) \dot{\Phi}_a - \quad (\text{B.6})$$

$$\left[ \frac{C_r \dot{\Phi}_a^2}{2} + \frac{C_g}{2} (\dot{\Phi}_a - V_{\text{ext}})^2 - \frac{\Phi_a^2}{2L_r} - \frac{C_g V_{\text{ext}}^2}{2} \right]$$

$$= \frac{C_\Sigma}{2} \dot{\Phi}_a^2 + \frac{\Phi_a^2}{2L_r}. \quad (\text{B.7})$$

Using  $C_\Sigma$ , Eq.(B.4), and defining  $Q_g = -C_g V$  as the externally induced charge, we arrive at the Hamiltonian of a capacitively coupled, driven LC-resonator:

$$H_{\text{LC}}(Q_a, \Phi_a) = \frac{1}{2C_\Sigma} (Q_a - Q_g)^2 + \frac{\Phi_a^2}{2L_r} \quad (\text{B.8})$$

LC resonator				
circuit diagram	descriptive variables	system of equations	Lagrangian Hamiltonian	Operators Commutation

This last step is necessary only for the description of circuits within the framework of quantum mechanics. In this case, we need to promote the conjugate variables to operators, thus:

$$Q_a \longrightarrow \hat{Q}_a, \quad \Phi_a \longrightarrow \hat{\Phi}_a$$

For the system Hamiltonian, we get

$$\hat{H}_{\text{LC}}(\hat{Q}_a, \hat{\Phi}_a) = \frac{1}{2C_\Sigma} \left( \hat{Q}_a - Q_g \right)^2 + \frac{\hat{\Phi}_a^2}{2L_r}, \quad (\text{B.9})$$

where we have to note, that  $Q_g$  still is a classical variable. For the conjugate momenta we introduce a commutation relations.

$$[\hat{\Phi}_a, \hat{Q}_a] = i\hbar, \quad (\text{B.10})$$

or, equivalently, a quantummechanical uncertainty relation

$$\Delta\Phi_a \Delta Q_a \geq \frac{1}{2}\hbar. \quad (\text{B.11})$$

## B.2 Cooper pair box

The very same procedure as above can be conducted to obtain the Hamiltonian of the basic charge qubit, a Cooper pair box (CPB). The circuit has a formal similarity with that of the LC resonator. This property is not very surprising, because, as we already mention in the main text, the potential of a transmon qubit (also a charge qubit) can be treated as a perturbation to the harmonic potential of a resonator.

Cooper pair box				
circuit diagram	descriptive variables	system of equations	Lagrangian Hamiltonian	Operators Commutation

The circuit diagram of a CPB is shown in Fig. B.4. The qualitative difference between the circuits is that the CPB involves a nonlinear inductance introduced by the Josephson junction. Quantitatively also the capacitance  $C_r$  is replaced by the capacitance of the Josephson junction  $C_J$ .

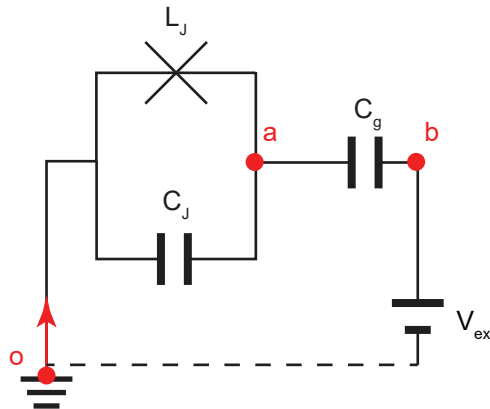


Figure B.4: Equivalent circuit for a Cooper pair box (CPB). Compared to the lumped element resonator circuit, in the CPB circuit, we replace the linear inductance ( $L_r$  in Fig. B.1) by the nonlinear Josephson inductance  $L_J$ .

Cooper pair box				
circuit diagram	descriptive variables	system of equations	Lagrangian Hamiltonian	Operators Commutation

This step is exactly the same as for the LC resonator, because the topology is identical.

Cooper pair box				
circuit diagram	descriptive variables	system of equations	Lagrangian Hamiltonian	Operators Commutation

In this step, the only difference to the linear resonator is that the BCE of the inductor is replaced by the BCE of a Josephson junction (JJ). As before, we start by applying KVL and KCL on the voltages and currents shown in Fig. B.5. Finally, we

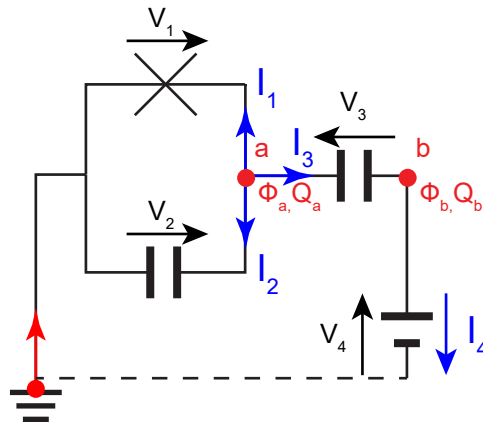


Figure B.5: KCL: The sum of the currents flowing out a node equals the sum of incoming currents ( $I_1 + I_2 + I_3 = 0$ ).

again use the branch constitutive equations to exploit the physical properties of the circuit component to obtain the complete system of equations.

#	branch voltage	#	component	BCE
$a$	$V_a = \dot{\Phi}_a - \dot{\Phi}_o = \dot{\Phi}_a - 0 = \dot{\Phi}_a$	1	JJ	$I_1 = I_c \sin(\varphi_{SC})$
$a$	$V_a = \dot{\Phi}_a = V_1$	2	Capacitor	$I_2 = C_r \ddot{\Phi}_a$
$a$	$V_a = \dot{\Phi}_a = V_2$	3	Capacitor	$I_3 = C_g (\ddot{\Phi}_b - \ddot{\Phi}_a)$
$b$	$V_b = \dot{\Phi}_b = V_4 = V_{\text{ext}}$	4	V-source	$V_4 = \dot{\Phi}_b = V_{\text{ext}}$

#	KCL
$a$	$I_1 + I_2 + I_3 = 0$
$b$	$I_4 = I_3$

Table B.3: Relations between descriptive variables gained from circuit topology and branch BCEs. The symbol "#" stands for node label, which can be  $a$  or  $b$  or branch number, which can be 1, 2, 3, or 4.

In the end, the system condenses to a single equation:

$$I_c \sin(\varphi_{\text{SC}}) + C_J \ddot{\Phi}_a = C_g (\dot{V} - \ddot{\Phi}_a). \quad (\text{B.12})$$

By defining  $C_\Sigma = C_J + C_g$  as the total capacitance, we can rearrange Eq. (B.12) to:

$$C_\Sigma \left( \ddot{\Phi}_a - \frac{C_g}{C_\Sigma} \dot{V} \right) = -I_c \sin(\varphi_{\text{SC}}). \quad (\text{B.13})$$

*Remark:* Equation (B.13) is valid for the CPB. To describe the transmon qubit circuit (see Fig. B.6), we assume the SQUID loop to act as a single tunable junction with  $L_J(f_{\text{ext}})$  and  $C_J$ . Additionally, we extend the definition of the total capacitance to  $C_{\text{TM}} = C_{\text{sh}} + C_J + C_g$ , to account for the shunt capacitor of the circuit. Thus, we get

$$C_{\text{TM}} \left( \ddot{\Phi}_a - \frac{C_g}{C_{\text{TM}}} \dot{V} \right) = -I_c(f_{\text{ext}}) \sin(\varphi_{\text{SC}}). \quad (\text{B.14})$$

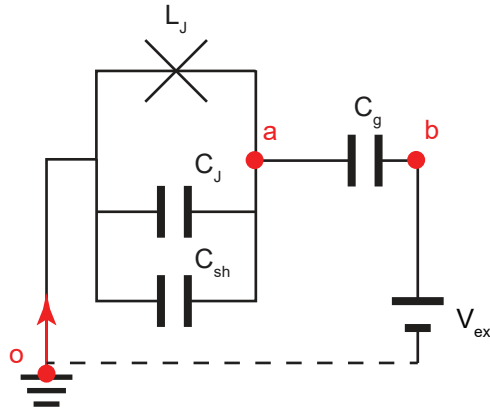


Figure B.6: Equivalent circuit for a transmon qubit. Compared to the Cooper pair box, in this circuit, we add a shunt capacitor  $C_{\text{sh}}$ .

Cooper pair box				
circuit diagram	descriptive variables	system of equations	Lagrangian Hamiltonian	Operators Commutation

Here, the Lagrangian of the system the equation of motion, Eq. (B.13), we find the Lagrangian of the system.

$$\mathcal{L}(\Phi_a, \dot{\Phi}_a) = \underbrace{\frac{C_r}{2} \dot{\Phi}_a^2 + \frac{C_g}{2} (V_{\text{ext}} - \dot{\Phi}_a)^2}_T - \underbrace{\left( E_J \cos(\varphi_{\text{SC}}) + \frac{C_g V_{\text{ext}}^2}{2} \right)}_U. \quad (\text{B.15})$$

Applying the Legendre transformation, also here, the equation of motion is found to have been derived before in Eq. (B.13).

We derive the conjugate momentum

$$Q_a = \frac{\partial \mathcal{L}}{\partial \dot{\Phi}_a} = C_\Sigma \dot{\Phi}_a - C_g V \quad (\text{B.16})$$

Applying the Legendre transformation  $H = Q\dot{\Phi} - \mathcal{L}$ , we get the system Hamiltonian:

$$H_{\text{CPB}}(Q_a, \Phi_a) = \frac{1}{2C_\Sigma} (Q_a - Q_g)^2 - E_J \cos(\varphi_{\text{SC}}), \quad (\text{B.17})$$

where  $Q_g = -C_g V$  is the externally induced charge.

For the transmon qubit, we find

$$H_{\text{TM}}(Q_a, \Phi_a) = \frac{1}{2C_{\text{TM}}} (Q_a - Q_g)^2 - E_J(f_{\text{ext}}) \cos(\varphi_{\text{SC}}) \quad (\text{B.18})$$

Cooper pair box				
circuit diagram	descriptive variables	system of equations	Lagrangian Hamiltonian	Operators Commutation

Also for the QPB, we need to promote the conjugate variables to operators, thus:

$$Q_a \longrightarrow \hat{Q}_a, \quad \Phi_a \longrightarrow \hat{\Phi}_a$$

Using  $\varphi_{\text{SC}} = \Phi(2\pi)/\Phi_0$  (see Appendix C.2), for the system Hamiltonian, we get:

$$\hat{H}_{\text{CPB}}(\hat{Q}_a, \hat{\Phi}_a) = \frac{1}{2C_{\Sigma}} \left( \hat{Q}_a - Q_g \right)^2 - E_J \cos(\hat{\varphi}_{\text{SC}}) \quad (\text{B.19})$$

and

$$\hat{H}_{\text{TM}}(\hat{Q}_a, \hat{\Phi}_a) = \frac{1}{2C_{\text{TM}}} \left( \hat{Q}_a - Q_g \right)^2 - E_J(f_{\text{ext}}) \cos(\hat{\varphi}_{\text{SC}}). \quad (\text{B.20})$$

Conjugate momenta and quantum mechanical uncertainty relation read

$$[\hat{\Phi}_a, \hat{Q}_a] = i\hbar \quad (\text{B.21})$$

$$\Delta\Phi\Delta Q \geq \frac{1}{2}\hbar \quad (\text{B.22})$$



# Appendix C

## Cooper pair box and transmon as qubit

To derive the Hamiltonian of a Cooper pair box (CPB) and a transmon qubit, we use a three-step procedure:

1. Derive a Hamiltonian for the LC resonator.
2. Replace the inductance of the resonator by the Josephson inductance.
3. Restrict to two energy levels and use Pauli operators.

### C.1 Harmonic oscillator

The Hamiltonian of the harmonic oscillator (see Tab. 2.1) is

$$H_{\text{HO}} = \frac{\hat{Q}^2}{2C} + \frac{\hat{\Phi}^2}{2L} \quad (\text{C.1})$$

or, equivalently,

$$H_{\text{HO}} = \frac{C\hat{\Phi}^2}{2} + \frac{\hat{\Phi}^2}{2L} \quad (\text{C.2})$$

A summary of the quantities and relation required to obtain Eq. (C.2) from Eq. (C.1) can be found in Tab. C.1.

### C.2 Introduce nonlinear inductance

To make the LC-resonator nonlinear, we replace the inductor by a Josephson junction [see Eq. 2.81 for the Josephson inductance] to create a Cooper pair box (CPB,

<b>Capacitor</b>		
1. Constitutive equation	$V(t) = \frac{1}{C}(\int I(t))$	$I(t) = C\dot{V}(t)$
2. Energy	$E = \int I(t')V(t')dt'$	$E = \int I(t')V(t')dt'$
3. Substitute	$E_{\text{cap}}(I) = \frac{1}{C} \int I(t') (\int I(t')) dt'$	$E_{\text{cap}}(V) = C \int V(t')\dot{V}(t')dt'$
4. Integration by parts and $Q = (\int I)$		
4. Result in $I$ and $V$	$E_{\text{cap}}(I) = \frac{1}{2C} (\int I)^2$	$E_{\text{cap}}(V) = \frac{C}{2} V^2$
4. Result in $Q$ and $\phi$	$E_{\text{cap}}(Q) = \frac{1}{2C} Q^2$	$E_{\text{cap}}(\phi) = \frac{C}{2} \dot{\phi}^2$
<b>Inductor</b>		
1. Constitutive equation	$V(t) = L\dot{I}(t)$	$I(t) = \frac{1}{L}(\int V(t))$
2. Energy	$E = \int I(t')V(t')dt'$	$E = \int I(t')V(t')dt'$
3. Substitute	$E_{\text{ind}}(I) = L \int I(t')\dot{I}(t')dt'$	$E_{\text{ind}}(V) = \frac{1}{L} \int (\int V(t'))V(t')dt'$
4. Integration by parts and $\phi = (\int V)$		
4. Result in $I$ and $V$	$E_{\text{ind}}(I) = \frac{L}{2} I^2$	$E_{\text{ind}}(V) = \frac{1}{2L} (\int V)^2$
4. Result in $Q$ and $\phi$	$E_{\text{ind}}(Q) = \frac{L}{2} \dot{Q}^2$	$E_{\text{ind}}(\phi) = \frac{1}{2L} \phi^2$

Table C.1: Energy of capacitor and inductor

see Fig. B.4) or by a capacitively shunted dc SQUID loop to design a transmon qubit (see Fig. B.6). In the latter case, the dc SQUID loop is treated as a single Josephson junction with tunable Josephson energy  $E_J$ .

Following Ref. [38], we introduce a relation between the descriptive variable  $\Phi$  and the gauge invariant phase difference  $\varphi_{\text{SC}}$ . Integrating Eq. (2.79) we find

$$\int \partial_t \varphi_{\text{SC}} dt = \frac{2\pi}{\Phi_0} \int V dt. \quad (\text{C.3})$$

Using the definition of flux  $\Phi = \int V dt$  in Eq. (2.24), we substitute its derivative  $V = \partial_t \Phi$  and find

$$\int \partial_t \varphi_{\text{SC}} dt = \frac{2\pi}{\Phi_0} \int \partial_t \Phi dt \quad (\text{C.4})$$

$$\implies \partial_t \varphi_{\text{SC}} = \frac{2\pi}{\Phi_0} \partial_t \Phi \quad (\text{C.5})$$

$$\implies \varphi_{\text{SC}} \propto \frac{2\pi}{\Phi_0} \Phi. \quad (\text{C.6})$$

Thus, from now on we will use  $\frac{2\pi}{\Phi_0} \Phi$  instead of the gauge invariant phase difference

$\varphi_{\text{SC}}$ . Following Ref. [38] and using Eq. (B.17) and Eq. (B.18), we find

$$\hat{H}_{\text{CPB}}(\hat{Q}_a, \hat{\Phi}_a) = \frac{1}{2C_\Sigma} \left( \hat{Q}_a - Q_g \right)^2 - E_J \cos\left(2\pi \frac{\hat{\Phi}_a}{\Phi_0}\right) \quad (\text{C.7})$$

$$\hat{H}_{\text{TM}}(\hat{Q}_a, \hat{\Phi}_a) = \frac{1}{2C_\Sigma} \left( \hat{Q}_a - Q_g \right)^2 - E_J(f_{\text{ext}}) \cos\left(2\pi \frac{\hat{\Phi}_a}{\Phi_0}\right) \quad (\text{C.8})$$

### C.3 Restriction to two energy levels

Here, we transform the Hamiltonians derived in Eq. (C.7) and Eq. (C.8) to use number state operators [38, 86, 87]. Charge and flux can be expressed in terms of number operators and number states by

$$\hat{Q} = -2e \sum_n \hat{n} |n\rangle, \quad n \in \mathbb{Z} \quad (\text{C.9})$$

$$e^{\pm i\hat{\varphi}} = \sum_n |n\rangle \langle n \pm 1|. \quad (\text{C.10})$$

Using the equations C.9, C.10, and the trigonometric identity  $\cos(\phi) = 1/2(\exp(i\phi) + \exp(-i\phi))$  we come to:

$$\hat{H}_{\text{QPB}} = \sum_n \left( E_Q (n - n_g)^2 |n\rangle \langle n| - \frac{E_J(2\pi \frac{\hat{\Phi}_a}{\Phi_0})}{2} (|n+1\rangle \langle n| + |n-1\rangle \langle n|) \right). \quad (\text{C.11})$$

Now, we limit the possible states of the hilbert space to  $|0\rangle$  and  $|1\rangle$ ,

$$\hat{H}_{\text{CPB}} = \left( E_Q (0 - n_g)^2 |0\rangle \langle 0| - \frac{E_J(2\pi \frac{\hat{\Phi}_a}{\Phi_0})}{2} (|1\rangle \langle 0|) \right) \quad (\text{C.12})$$

$$+ \left( E_Q (1 - n_g)^2 |1\rangle \langle 1| - \frac{E_J(2\pi \frac{\hat{\Phi}_a}{\Phi_0})}{2} (|0\rangle \langle 1|) \right). \quad (\text{C.13})$$

Subtracting an energy offset  $E_Q (n_g^2 - (1 - n_g)/2) \cdot \mathbb{I}$ , we obtain

$$\hat{H}_{\text{CPB}} = E_Q \frac{1 - 2n_g}{2} (|0\rangle \langle 0| - |1\rangle \langle 1|) \quad (\text{C.14})$$

$$+ \frac{E_J(\Phi)}{2} (|0\rangle \langle 1| + |1\rangle \langle 0|), \quad (\text{C.15})$$

with  $E_{\text{ch}}(n_g) = E_Q(1 - 2n_g)$ , the Pauli operators  $\sigma_z = |0\rangle\langle 0| - |1\rangle\langle 1|$  and  $\sigma_x = |0\rangle\langle 1| + |1\rangle\langle 0|$ , and the identity operator  $\mathbb{I}$ , we finally get

$$\hat{H}_{\text{CPB}} = -\frac{E_{\text{ch}}(n_g)}{2}\hat{\sigma}_z + \frac{E_J(2\pi\frac{\hat{\Phi}_a}{\Phi_0})}{2}\hat{\sigma}_x \quad (\text{C.16})$$

Remark: Comparing the Hamiltonian in Eq. (C.16) with Leggett *et al* [16] we identify  $\hbar\epsilon = E_{\text{ch}}$  and  $\hbar\Delta_0 = E_J$ .

# Appendix D

## Coplanar waveguide transmission line

As mentioned in Sec. 2.3.1 we focus on co-planar waveguides [see Fig. D.1(a)]. One

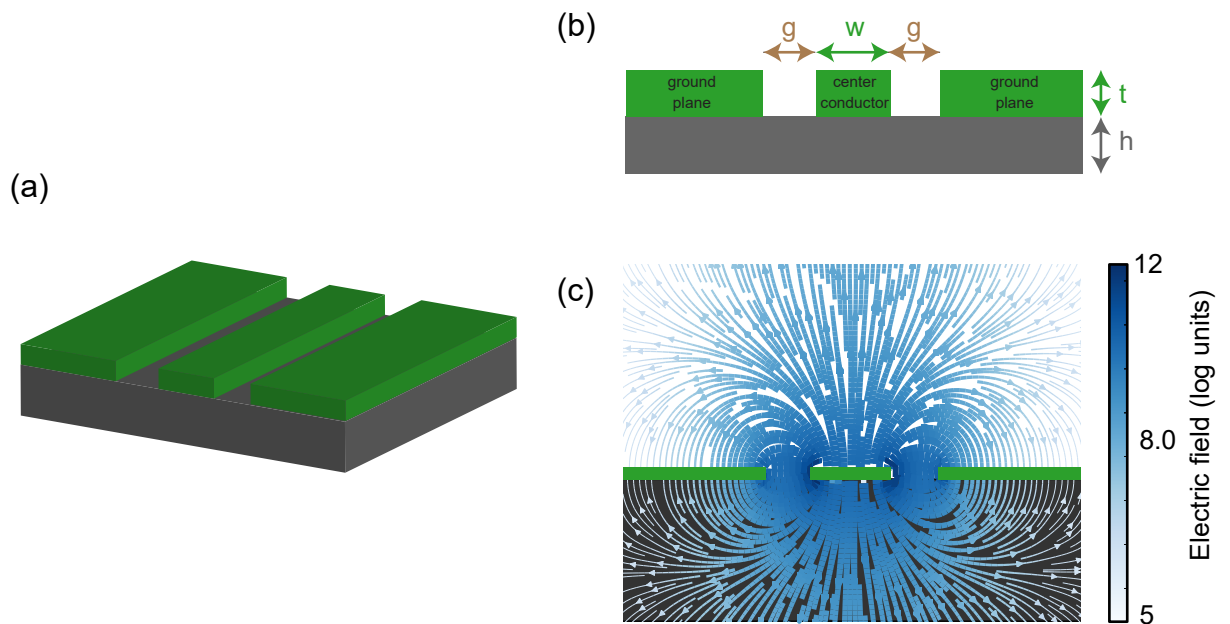


Figure D.1: (a) 3D model of a piece of a coplanar waveguide (CPW), (b) front view of CPW, green: superconducting material, grey Si-substrate,  $t$ ...thickness of superconducting film,  $h$ ...height of substrate,  $g$ ...gap width,  $w$ ...width of center conductor, (c) Electrical field lines (blue) in a coplanar waveguide (green).

key advantage of these structures is that they can be fabricated using well known lithographic techniques and that their characteristic impedance  $Z_0$  is defined mainly

by the effective dielectric constant  $\epsilon_{\text{eff}}$  of substrate and metalization and the geometric dimensions,  $g$  (gap width), and  $w$  (center conductor width) of the structure [see Fig. D.1(b)]. For our parameters,  $t \approx 100$  nm (thickness of superconducting metalization) and  $h \approx 550$   $\mu\text{m}$  (substrate height), the relation  $t \ll h$  applies. Then, an analytic expression for  $Z_0$  can be derived by conformal mapping techniques [88, 89]:

$$Z_0 = \frac{30\pi}{\sqrt{\epsilon_{\text{eff}}}} \frac{K(k')}{K(k)}, \quad \text{with: } k^{(\prime)} = k^{(\prime)}(w, g), \quad (\text{D.1})$$

where  $K(k')$  is the elliptical integral.

In CPWs, we find transverse electromagnetic (TEM) modes[23], whose electric field distribution is shown in Fig. D.1(c). The electric field in TEM modes is oriented perpendicular to the direction of propagation. Modeling a transmission line, we have

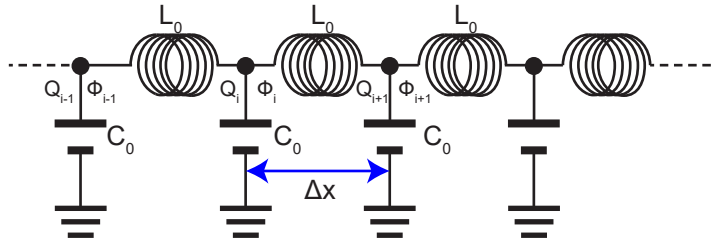


Figure D.2: To model a transmission line, it is cut into pieces and every piece is modeled as LC-resonator. Letting the length of the pieces go to zero  $\Delta x \rightarrow 0$  we end up with an infinite series of LC-resonators.

to account for its non-negligible size along the propagation direction, compared to the microwave wavelength. We do this by cutting it into infinitely many small pieces of length  $\Delta x$ . Each piece is modeled as a LC-resonator. The equivalent circuit for a transmission line then becomes an infinite series of LC-resonators (Fig. D.2).

## Hamiltonian

To derive the Hamiltonian of a transmission line, we follow the recipe given in Sec. 2.2 and start by finding a Lagrangian. As seen above, we model a transmission line of length  $L$  as an infinite chain of harmonic oscillators. From Eq. (2.33) we know the

Lagrangian for a single LC-resonator and thus get

$$\mathcal{L} = T - U = \sum_{i=1}^N \mathcal{L}_{\text{LC},i} \quad (\text{D.2})$$

$$= \sum_{i=1}^N \left( \frac{Q_i^2}{2C_0} \right) - \sum_{i=1}^{N-1} \left( \frac{(\Phi_{i+1} - \Phi_i)^2}{2L_0} \right) \quad (\text{D.3})$$

$$= \sum_{i=1}^N \frac{\Delta x}{2c_0} \left( \frac{Q_i}{\Delta x} \right)^2 - \sum_{i=1}^{N-1} \frac{\Delta x}{2l_0} \left( \frac{(\Phi_{i+1} - \Phi_i)}{\Delta x} \right)^2. \quad (\text{D.4})$$

In Eq. (D.4), for infinitesimally small pieces of the transmission line of length  $\Delta x = L/N$ , the capacitance and inductance of a single infinitesimal small piece are  $C_0 = c_0 \Delta x$  and  $L_0 = l_0 \Delta x$ , where  $c_0$  and  $l_0$  are introduced as the capacitance and inductance per unit length. We replace sums by integrals in Eq. (D.4), define the charge density  $\rho(x_i) = Q_i/\Delta x$  and flux derivative  $\partial_x \phi(x_i) = (\Phi_{i+1} - \Phi_i)/\Delta x$ , and formulate the Lagrangian as an integral:

$$\mathcal{L} = \int dx \left\{ \frac{\rho(x)^2}{2c_0} - \frac{(\partial_x \phi(x))^2}{2l_0} \right\} \quad (\text{D.5})$$

$$= \int dx \left\{ \frac{c_0 (\partial_t \Phi)^2}{2} - \frac{(\partial_x \phi(x))^2}{2l_0} \right\}, \quad (\text{D.6})$$

where we have used the conjugate momentum definition  $\rho = c_0 \dot{\Phi}$ . In the same way as for the Lagrangian in Eq. (D.6), we obtain:

$$H = \int dx \left\{ \frac{\rho(x)^2}{2c_0} + \frac{(\partial_x \phi(x))^2}{2l_0} \right\}, \quad (\text{D.7})$$

$$= \int dx \left\{ \frac{c_0 \dot{\Phi}^2}{2} + \frac{(\partial_x \phi(x))^2}{2l_0} \right\}, \quad (\text{D.8})$$

Using  $\partial_\mu \equiv (\partial/(c\partial t), \Delta)$  we find this to be of the same form as the massless Klein-Gordon equation and thus having equivalent solutions [55].